Dwarf Galaxies as Laboratories of Protogalaxy Physics:

Canonical Star Formation Laws at Low Metallicity

by

Jacqueline Ann Monkiewicz

A Dissertation Presented in Partial Fulfillment
of the Requirements for the Degree
Doctor of Philosophy

Approved May 2018 by the
Graduate Supervisory Committee:

Judd Bowman, Chair
Paul Scowen
Philip Mauskopf
Evan Scannapieco
Rolf Janssen

ARIZONA STATE UNIVERSITY

December 2018

ABSTRACT

In the upcoming decade, powerful new astronomical facilities such as the James Webb Space Telescope (JWST), the Square Kilometer Array (SKA), and ground-based 30-meter telescopes will open up the epoch of reionization to direct astronomical observation. One of the primary tools used to understand the bulk astrophysical properties of the high-redshift universe are empirically-derived star-forming laws, which relate observed luminosity to fundamental astrophysical quantities such as star formation rate. The radio/infrared relation is one of the more mysterious of these relations: despite its somewhat uncertain astrophysical origins, this relation is extremely tight and linear, with 0.3 dex of scatter over five orders of magnitude in galaxy luminosity. The effects of primordial metallicities on canonical star-forming laws is an open question: a growing body of evidence suggests that the current empirical star forming laws may not be valid in the unenriched, metal-poor environment of the very early universe.

In the modern universe, nearby dwarf galaxies with less than 1/10th the Solar metal abundance provide an opportunity to recalibrate our star formation laws and study the astrophysics of extremely metal-deficient (XMD) environments in detail. I assemble a sample of nearby dwarf galaxies, all within 100 megaparsecs, with nebular oxygen abundances between 1/5th and 1/50th Solar. I identify the subsample of these galaxies with space-based mid- and far-infrared data, and investigate the effects of extreme metallicities on the infrared-radio relationship. For ten of these galaxies, I have acquired 40 hours of observations with the Jansky Very Large Array (JVLA). C-band (4-8 GHz) radio continuum emission is detected from all 10 of these galaxies. These represent the first radio continuum detections from seven galaxies in this sample: Leo A, UGC 4704, HS 0822+3542, SBS 0940+544, and SBS 1129+476. The radio

continuum in these galaxies is strongly associated with the presence of optical H-alpha emission, with spectral slopes suggesting a mix of thermal and non-thermal sources. I use the ratio of the radio and far-infrared emission to investigate behavior of the C-band (4-8 GHz) radio/infrared relation at metallicities below 1/10th Solar. I compare the low metallicity sample with the 4.8 GHz radio/infrared relationship from the KINGFISHER nearby galaxy sample (Tabatabaei *et al.*, 2017) and to the 1.4 GHz radio/infrared relationship from the blue compact dwarf galaxy sample of Wu *et al.* (2008). The infrared/radio ratio q of the low metallicity galaxies is below the average q of star forming galaxies in the modern universe. I compare these galaxies' infrared and radio luminosities to their corresponding Hα luminosities, and find that both the infrared/Hα and the radio/Hα ratios are reduced by nearly 1 dex in the low metallicity sample vs. higher metallicity galaxies; however the deficit is not straightforwardly interpreted as a metallicity effect.

DEDICATION

This doctoral disserataion is dedicated to my parents, Audrey Constance Mierzwa Monkiewicz and Kim Victor Monkiewicz, without whose unconditional support and love it would certainly not exist.

TABLE OF CONTENTS

LIST OF TABLES

LIST OF FIGURES

Figure Page

Chapter 1

CANONICAL STAR FORMATION LAWS AT LOW METALLICITY

1.1 Project Significance: Protogalaxy Feedback and JWST

Central to the NASA Cosmic Origins Program[1], and a key science driver identified by the NASA Science Mission Directorate's Astrophysics Roadmap[2], are observations of the very first galaxies to form after the Big Bang. These primordial objects profoundly altered the chemical and thermal history of the intergalactic medium (IGM), flooding the universe with ultraviolet and X-ray radiation from the first stars and supernovae. This surge of radiation ended the Cosmic Dark Ages and triggered the epoch of reionization (EoR), converting the cooling web of neutral hydrogen back to the hot plasma state that dominates the modern universe [3].

We may now be able to observe the IGM during the earliest stages of this process: a possible detection of the redshifted 21-cm hydrogen spin-flip transition has been reported by the *Experiment to Detect the Global EoR Signature (EDGES)* experiment (Bowman *et al.*, 2018), via a broad absorption trough in the cosmic microwave background CMB at 78 MHz. Assuming the trough is due to coupling of the neutral hydrogen spin temperature T_s with the kinetic gas temperature T_g via resonant scattering of Lyman α photons from the first stars, this frequency corresponds to

[1]NASA Cosmic Origins Program: http://cor.gsfc.nasa.gov/

[2]2013 Astrophysics Roadmap, NASA Science Mission Directorate: http://science.nasa.gov/media/medialibrary/2013/12/20/secureAstrophysics_Roadmap_2013.pdf

[3]HERA: The Hydrogen Epoch of Reionization Array roadmap. http://reionization.org

redshifts between $20 > z > 15$, and thus may represent the early signature of Cosmic Dawn. The full reionization of the IGM happens a couple hundred million years later, between redshifts of $12 < z < 6$. Along with *EDGES*, numerous long-wavelength radio experiments are underway worldwide. The *Low Frequency Array (LOFAR; de Vos et al., 2009)*, the *Murchison Widefield Array (MWA; Lonsdale, 2009)*, and the *Square Kilometer Array (SKA)* all prominent players in the effort to directly observe reionization via the disappearance of the absorption signal of the evaporating neutral hydrogen.

While the race to directly observe reionization continues, on the other side of the equation are the early protogalaxies which triggered it. For the past two decades the *Hubble Space Telescope (HST)* has been the premier tool for probing the faintest, reddest, and most distant galaxies. Long-exposure pointings with increasingly sensitive cameras on *HST* have produced images of young galaxies up to 13 billion light-years away, providing information about a time when the universe itself was less than a billion years in age. Direct observation of the protogalaxies that spurred reionization is one of the primary mission goals of *HST*'s successor, the *James Webb Space Telescope (JWST)*. Set to launch in 2021, *JWST* is expected to push the limits of our knowledge all the way back to the very edge of the Cosmic Dark Ages.

However, even *JWST* has its limits. As with all observations of the early universe, the information obtained will be limited by the enormous distances and penalized by the dimming effects of relativity in an expanding universe. All of the available light from each primordial galaxy will be jammed into just a few precious pixels of data. Most inferences to be made about these objects and their impact on the early IGM will be derived from spectral energy distributions, census statistics, and challenging spectroscopic measurements with large (10-30 meter) ground-based telescopes.

To make use of these data, we will need to translate them into astrophysically-meaningful quantities, such as the number of stars formed in a protogalaxy per year. This is a galaxy's star-formation rate (SFR), e.g. the total number of stars formed per year, in units of Solar mass. If we can measure the individual SFRs for a complete sample of galaxies at a given redshift, we can obtain the global star-formation rate of the universe at large at a given cosmic age. Because early stars are assumed to be the primary emitters of ionizing photons, the global SFR tells us about the intergalactic radiation field available to trigger reionization at a given redshift. Additionally, the global SFR tells us about the potential for chemical enrichment of the early universe. Stars are the production sites for all the chemical elements more massive than boron; the integrated star formation rate up to a given epoch tells us about the availability of the elements necessary for making planets, and life.

Empirically-derived star formation correlations are the Rosetta stones which translate observable quantities such as broad-band luminosities into astrophysical quantities such as star-formation rate. These relationships are well-established at low redshifts ($z < 0.1$), and are commonly built into computational simulations of the universe at all epochs. However, their reliability at high redshifts is more questionable: extreme low metallicities means a paucity of a shielding/cooling elements, harder ionizing radiation fields, and possibly a top-heavy initial mass function.

These conditions should result in substantial alterations in the established star-forming correlations, but the difficulties of high-redshift observations have limited our ability to actually quantify these changes. Further complicating this picture is the fact that we expect the bulk of the sources responsible for reionization to be low-luminosity dwarf galaxies, which are well-below the current detection limits of both space- and ground-based astronomical facilities (Ouchi et al. 2009; Yajima, Choi & Nagamine

2011; Bouwens et al. 2015). Even with JSWT and 30+ meter ground-based telescopes, our ability to study a true dwarf galaxy sample at high redshift will be severely curtailed, with our only information coming from gravitational lensing studies. We need to establish whether or not the observational correlations we have established at low redshifts are even applicable at high redshifts. If not, we will need to develop new empirical standards for working in a low metallicity environments analogous to the early universe.

1.1.1 Extreme Dwarf Starbursts as Protogalaxy Analogs

Modern dwarf galaxies provide handy laboratories for studying the processes of star formation in environments which are physically and chemically similar to conditions of the early universe. A rare handful of these local galaxies are very like protogalaxies themselves: blue compact dwarf galaxies such as 1 Zw 18 or SBS 0335-052 are found to have nebular oxygen abundances which are 1/50th and 1/40th of the Solar values, respectively. Even their optical spectra look primordial: their bright emission line ratios remarkably similar to high-redshift Lyman-alpha galaxies, implying unusually hard ionizing radiation and very little shielding from dust (Nakajima *et al.*, 2012; Kniazev *et al.*, 2003; Skillman and Kennicutt, 1993). For several decades after the discovery of 1 Zw 18 and SBS 0335-052, astronomers speculated that these might truly be late-forming infant galaxies, only recently coalesced from the cosmic web.

The infant galaxy theory was eventually disproven by the discovery of > 1 Gyr stars in 1 Zw 18 (Aloisi *et al.*, 2007). Instead of being truly primordial objects, it appears that dwarf galaxies simply lack the gravitational wells to retain the products of stellar nucleosynthesis, which are ejected efficiently and completely by supernovae-driven

galactic winds (e.g. Henry *et al.* (2013a)). This makes dwarf galaxies intriguing for their ability to chemically enrich the IGM, while maintaining their own pristine and comparatively unenriched internal environments. Even if these are not inherently primordial objects, these low-metallicity galaxies nonetheless provide an opportunity to study up close the detailed chemical and physical conditions of an environment which is directly analogous to the earliest protogalaxies. Extremely metal-deficient dwarf (XMD) galaxies, with nebular oxygen abundances less than 1/10th Solar, are of particular interest.

1.2 High Redshift Comparisons

It is quite difficult to directly compare the properties of high- and low-redshift galaxies. Optical data of high-redshift sources traces the rest-frame ultraviolet, which is difficult or even impossible to observe in low-redshift galaxies; the optical emission lines typically used to benchmark the properties of low-redshift galaxies are shifted into the infrared, and become inaccessible to ground-based facilities at the redshifts of reionization. Even where data exist, it is difficult to produce truly analogous samples: at high-redshift, volume-complete samples only exist for the most luminous galaxies, which are not currently believed to be the primary drivers of reionization (Grazian *et al.*, 2017).

In recent decades, the observational situation has improved. Ultraviolet instrumentation on space-based telescopes such as *GALEX, FUSE*, and *HST* have enabled observation of the near-UV (though at $z \sim 0$, direct observation of ionizing Lyman alpha and Lyman continuum is blocked by the interstellar absorption of the Milky Way's own neutral hydrogen). Meanwhile, the increasing availability of near-infrared

spectrometers on 10-meter class ground-based telescopes has made rest-frame optical measurements of high-redshift galaxies more common. We can therefore draw some conclusions about the high-redshift universe, notably:

- The overall rate of star formation was much higher during earlier cosmic epochs. High-intensity, compact starbursts were much more common at high redshifts than in the modern epoch (Madau and Dickinson, 2014).
- Dusty starbursts appeared much sooner than expected (Blain *et al.*, 2002; Casey *et al.*, 2014; Hashimoto *et al.*, 2019; Shao *et al.*, 2019).
- The mass-metallicity relationship shifts downward at increasing redshift (Henry *et al.*, 2013a).
- Galactic outflows were ubiquitous in the early universe (Martin *et al.*, 2012; Erb *et al.*, 2012).
- The escape of ionizing UV photons into the IGM becomes more efficient (see next section).
- "Normal" spirals had much more neutral gas available (González-López *et al.*, 2017; Kaasinen *et al.*, 2019).

The mass-metallicity relation is of particular relevance to this work. At low redshift, it is well-established that higher luminosity galaxies generally have higher gas-phase metallicity (Tremonti *et al.*, 2004; Lee *et al.*, 2006). This is interpreted as evidence that higher mass galaxies are better at retaining the nucleosynthetic output of prior generations of stars. It is not really unexpected that entire relationship shifts downward at increasing redshift (Henry *et al.*, 2013a; Cullen *et al.*, 2019): at earlier epochs of cosmic history, galaxies have hosted proportionally fewer generations of stars, which have produced proportionally less nucleosynthetic output. "Extreme" metallicities of less than 1/10th Solar are presumably much more common at high

redshift, and low metallicities should be associated with somewhat more massive galaxies at high redshift. There may be a limit to *how* massive, however: dust is associated with massive galaxies at surprisingly high redshifts (Casey *et al.*, 2014), suggesting the enrichment of the ISM proceeds very rapidly in massive starbursts. This may in turn limit the escape of the ionizing photons necessary to power reionization. Even at high redshifts, extreme low metallicities may still be associated primary with low-mass galaxies, which may be the primary drivers of reionization.

1.2.1 Impact of Metallicity on the LyC Escape Fraction

Linking 21-cm observations of reionization with *JWST* observations of the early universe is the Lyman continuum (LyC) escape fraction f_{esc}, i.e. the percentage of ionizing photons which escape the galaxy's own enshrouding interstellar medium to reach the intergalactic medium. This radiation is required to trigger the reionization of the intergalactic web, and is presumably produced in abundance by the earliest protogalaxies. In modern galaxies, ionizing ultraviolet photons are produced exclusively in regions of high mass star formation by O and B stars–the very youngest, most massive stars in a galaxy. These stars are typically buried deep inside dusty nebulae, where their ionizing radiation is blocked by interstellar dust and neutral hydrogen. Consequently, very little of the ionizing UV is found to escape from modern starbursting galaxies. At low redshift LyC "leakers" are quite rare; dedicated searches have produced only a handful of nearby galaxies with $z < 1$ and $f_{esc} > 10\%$ (Leitet *et al.*, 2011; Leitherer *et al.*, 2016; Borthakur *et al.*, 2014; Izotov *et al.*, 2016a,b).

Searches for LyC "leakers" at $z > 0.5$ have been more fruitful (Naidu *et al.*, 2017; Izotov *et al.*, 2011), but at $z > 4$ it becomes increasingly difficult to directly observe

the ionizing flux, due to the incompleteness of reionization at higher redshifts. We do expect LyC escape to become more efficient at increasing redshifts–otherwise there would be insufficient ionizing flux for reionization between $6 < z < 10$. As f_{esc} increases, it will take proportionally less star formation to reionize the early IGM (e.g. Zackrisson *et al.*, 2017); it is therefore essential to accurately estimate the total UV flux exiting early protogalaxies.

Unfortunately, our ability to directly measure the ultraviolet photons responsible for reionization is hindered by the opacity of the very neutral hydrogen atoms being reionized. Even a very low neutral IGM fraction can partially or completely block the ionizing Lyman continuum emission (Gunn and Peterson, 1965; Bechtold *et al.*, 1987; Madau, 1995). For redshifts between $4 < z < 6$, the bulk of the expected attenuation will be concentrated in stochastically-distributed Lyman limit systems (Inoue and Iwata, 2008; Prochaska *et al.*, 2009; Inoue *et al.*, 2014), so it may be possible to interpolate around the intervening systems or find "clean" sightlines. But once we reach the epoch of reionization, when large parts of the cosmic web are still neutral, almost none of the ionizing flux is observable from Earth. For *JWST*, the 91.2 nm Lyman limit will only be observable at $z > 5.5$, at which point we can expect the opacity of the IGM to introduce considerable uncertainty. If we want to understand the impact of early galaxies on the IGM, we will need to be able to reliably predict their star formation rate and UV escape fraction from their broad-band luminosities at wavelengths which are actually observable. In order to do that, we must have a better understanding of the physics of star formation in primordial, low-metallicity environments.

Galactic scale winds may in turn create more favorable conditions for the escape of LyC radiation by blowing holes in the confining interstellar medium (Mac Low

and McCray, 1988; Clarke and Oey, 2002). Dust geometry, patchy ISM, and ionized superbubbles are all believed to play a role, especially in dwarf galaxies with their bursty star formation. Starbursting galaxies at all redshifts are found to be surprisingly efficient at launching enriched material into their halos (Heckman *et al.*, 1990; Martin *et al.*, 2012; Erb *et al.*, 2012). Dwarf galaxies, with their weaker gravitational potentials and lower escape velocities, may be especially efficient at transporting the entirety of their enriched gas into the IGM (Henry *et al.*, 2013b; Kirby, 2015, and references therein). Simulations and observations both indicate that momentum-driven winds are very efficient at removing the products of stellar nucleosynthesis, either directly (Martin *et al.*, 2002) or via entrainment (Scannapieco and Brüggen, 2010), and that the ejection of enriched gas is more efficient as galaxy mass decreases (Christensen *et al.*, 2016).

1.2.2 Dwarf Galaxies at High Redshift

For galaxies at $z \geq 3$, it is possible to observe Lyman continuum directly with ground-based telescopes: for example, Grazian *et al.* (2017, G17) use U-band imaging at the Large Binocular Telescope to observe 69 galaxies with spectroscopic redshifts at with $3.27 < z < 3.40$. This redshift range corresponds to the peak epoch of global star formation; extragalactic astronomers sometimes refer to this epoch as "Cosmic Noon". G17 report a stringent upper limit for luminous galaxies ($L < L_*$) of $f_{esc} < 1.7\%$. For lower luminosity galaxies, with $L < 0.2L_*$, this increases to $f_{esc} < 10\%$. But even with the boost from these less luminous galaxies, G17 calculate that the total combined contribution to the ionizing UV background from all galaxies observed at these redshifts *is insufficient to maintain an ionized IGM at these redshifts.* In

order to sustain reionization to the present day, the UV continuum requires a sizable contribution from galaxies well below the currently-observable flux limits at $z \sim 3$. If dwarf galaxies are able to maintain escape fractions $f_{esc} > 10\%$, they would contribute the missing Lyman continuum photons.

Unfortunately, $z > 6$ dwarf galaxies are well out of reach of the current sensitivity limits of *HST* and ground-based 10-meter telescopes. Even *JWST* will be unable to directly observe dwarf galaxies at these redshifts.

Gravitational lensing is currently the only viable way to observe low-mass, low-luminosity galaxies at high redshift. Strong gravitational lensing can magnify an underluminous galaxy into the sensitivity range of *HST* or ground-based telescopes. Lensed galaxies at $z \sim 2$ have even been successfully observed at infrared and radio wavelengths with the *Jansky Very Large Array(JVLA)* (Hsu *et al.*, 2017), the *Atacama Large Millimeter Array (ALMA)* (González-López *et al.*, 2017) and *Herschel* (Rawle *et al.*, 2016). From these studies we have learned that dwarf galaxies at high redshift do have optical properties very similar to blue compact dwarfs at low redshift.

While most lensing studies have focused on $1.5 < z < 3$ targets, Hubble Frontier Fields observations by Atek *et al.* (2015) have made some headway into constraining the lower luminosity end of the galaxy mass function during the epoch of reionization at $6 < z < 8$. These observations indicate that high redshift dwarf galaxies are spatially quite compact (Bouwens et al. 2017), but should be capable of reionizing the IGM with LyC escape fractions f_{esc} >10-15%. However, there remains considerable uncertainty about the faint end slope of the UV luminosity function at these redshifts (Atek et al. 2018).

1.2.3 Variations in the IMF at High Redshift

A modified stellar initial mass function (IMF) is another common expectation of the high redshift universe, but it is one that has remained stubbornly resistant to observation verification (Myers *et al.*, 2011, and references therein). Simulations of the formation of the very first stars from the near-pure hydrogen and helium gas left over after the Big Bang produce a vastly different mass function. In the absence of major cooling species such as carbon and oxygen, molecular hydrogen cooling produces a minimum stellar fragmentation mass of hundreds of solar masses (Abel *et al.*, 2002; Nakamura and Umemura, 2002; Bromm and Loeb, 2003; McKee and Tan, 2008). Observations of the high redshift universe may support the notion of a top-heavy IMF at earlier times (see e.g. van Dokkum, 2008; Cowley *et al.*, 2019), while Narayanan and Davé (2012) point out a wide variety of theoretical/observational discrepancies which would be resolved by a top-heavy IMF. The only thing that is missing from this picture is evidence of metallicity-related IMF variations from resolved stellar population studies. And it is indeed missing: while numerous authors have surveyed low metallicity environments such as the outer Milky Way or the Magellanic Clouds, no claims of IMF variations have stood the test of time (reviews: Bastian *et al.*, 2010; Oswalt and Gilmore, 2013). Geha *et al.* (2013) are among the few authors claiming to have found evidenced of an altered IMF, in this case via a flattening of the low-mass IMF in Leo IV and Hercules, two extremely metal-poor dwarf spheroidal galaxies (though see El-Badry *et al.*, 2017). In short: while theory and observations of high-redshift galaxies have seemingly given us every reason to expect the IMF to change in the high redshift universe, to date we have not yet produced unambiguous evidence confirming this expectation from resolved stellar populations.

This dissertation does not make any attempt to measure the IMF in low metallicity galaxies, and a standard Salpeter (1955) IMF is built into all of the star-forming correlations used in later chapter to relate hydrogen recombination lines to the mass of stars formed per year.

1.3 Canonical Star Formation Relations at Low Metallicity

One of the primary tools that will be used to interpret JWST protogalaxy data will be the various canonical star-forming relations (see e.g. Senarath *et al.*, 2018). These empirically-derived relationships use luminosity measures at various wavelengths– ultraviolet emission, hydrogen Balmer lines, bolometric dust luminosity, molecular gas, radio continuum–as proxies to estimate the overall star formation rate. Generally, galaxy luminosity in one wavelength regime is found to increase monotonically with luminosity in another; generally, these relations are approximately linear, but not always straightforwardly proportional. These relations, in combination with JWST imaging and ground-based spectroscopy, are what will allow us to transform galaxy counts and spectral energy distribution into overall star formation rates and ultraviolet luminosities during the epoch of reionization.

Considerable effort has been expended to extend the use of these relationships to the higher redshift universe. But there remains considerable uncertainty about the behavior of the low-luminosity, low-metallicity end of most star-forming relations. Comparisons of Hα and far-UV star formation estimates are highly discrepant for dwarf galaxies, even after dust attenuation has been accounted for (Lee *et al.*, 2009a, 2011; McQuinn *et al.*, 2015). Lee et al. assert that the discrepancy is not attributed to gas-phase metallicity, and examine other possibilities, including IMF variations,

faint missing emission, and the effects of "bursty" star formation episodes in dwarf galaxies.

Other star formation measures show clearer signs of metallicity dependence, including mid- and far-infrared luminosity (Engelbracht *et al.*, 2005, 2008; Houck *et al.*, 2004; Wu *et al.*, 2006), molecular gas fraction (Barone *et al.*, 2000), thermal X-ray (see, e.g. Ott *et al.* (2005)), and non-thermal radio emission (Wu *et al.*, 2008; Chyży *et al.*, 2011).

In this section I review and summarize the existing literature on the effects of low metallicity on canonical star forming laws, in order of decreasing electromagnetic frequency. Because these are fundamentally empirical correlations, derived as a way to estimate star formation using a particular telescope or wavelength range, I begin by classifying them according to the wavelength ranges. I discuss the astrophysical processes assumed to be driving the observed relationships, and how low metallicity environments are expected to impact the observed relationships.

1.3.1 Canonical Star Formation Relations at Ultraviolet through Near-Infrared Wavelenghts

Among all the various empirically-derived star formation relations, one of the most cited is the Kennicutt *et al.* (1994, K94) Hα relation, which straightforwardly relates the extinction-corrected Hα luminosity of a galaxy to its global SFR. The Balmer lines of hydrogen are a popular star formation rate indicator, due to both their brightness and easy observability in the optical part of the electromagnetic spectrum. However, the Balmer lines may be subject to considerable extinction in dusty, high-metallicity star forming environments. Observations of near-infrared recombination lines such as

Brackett γ ($\lambda = 2.166\mu$m) and Paschen α ($\lambda = 1.876\mu$m) have greatly reduced dust extinction uncertainties, and are therefore used to anchor the empirical calibrations for $L_{H\alpha}$. Using narrow-band Paschen-α imaging from the *Hubble Space Telescope*, MIPS 24μm imaging from the *Spitzer Space Telescope*, and updated assumptions about the stellar initial mass functions, Calzetti *et al.* (2007, C07) updated the relation of K94:

$$SFR[M_{\odot}yr^{-1}] = 5.3 \times 10^{-42} L(H\alpha)_{corr}[ergs\ s^{-1}] \tag{1.1}$$

where

$$L(H\alpha)_{corr} = L(H\alpha)_{obs} + 0.031 \pm 0.006 L(24\mu m) \tag{1.2}$$

Following the suggestion of Gordon *et al.* (2000) and Kennicutt *et al.* (2007), C07 include an additive correction for the mid-infrared 24 μm flux, which captures the portion of the ionizing UV which is absorbed and reradiated by dust. At normal metallicities, $12 + (O/H) > 8.3$, this correction reduces the scatter in the Hα/Pa-α correlation.

C07 divide their calibration sample into three metallicity groups: high metallicity, $12 + (O/H) > 8.3$; intermediate, $8.3 > 12 + (O/H) > 0.8$; and low, $12 + (O/H) < 8.0$. While there are a handful of XMD galaxies in the starburst sample they import from Engelbracht *et al.* (2005)–notably HS 0822+3542, UGC 292A, and SBS 0335-05200– the main sample only includes galaxies with nebular oxygen abundances down to $12 + (O/H) > 7.6$, which is the upper limit of the XMD category. With the addition of the 24 μm correction, C07 are able to fit produce a good correlation between Hα_{corr} and Pa-α luminosities, for all but the most metal deficient galaxies (C07, Figure

7). The Engelbracht starbursts are not included in this correlation, however, so the behavior at extreme metallicities is not really examined.

Are hydrogen recombination lines like Hα and Pa-α the best star formation measures? In any star-forming galaxy, a certain fraction of Hα flux is diffusely distributed, and not clearly associated with ongoing star-formation regions. In principle, what we would truly like to measure is the total ultraviolet flux output by a star-forming galaxy. Ultraviolet traces the young stars, and thus gives us a direct, instantaneous measure of the current high-mass star formation rate. Unfortunately, ultraviolet is heavily attenuated by dust, making it impractical for estimating star formation in most normal spiral galaxies.

Low metallicity dwarf galaxies, on the other hand, have comparatively little dust. Using *GALEX* near- and far-UV imaging, Lee *et al.* (2011) examined the star formation correlations for a volume-complete sample of 390 dwarf galaxies within 11 Mpc. They use the NUV-FUV color to estimate the internal reddening and hence extinction of the individual galaxies, and L_{FUV} to estimate the star formation rate. Lee *et al.* (2009a) had previously found that the FUV/Hα star formation estimates were highly discrepant for dwarf galaxies vs. the regular spiral sample. They attribute this behavior to dwarf galaxy "burstiness" (short star formation duty cycles) rather than metallicity. But once again: their metallicity sample is incomplete below 1/10th solar abundance.

1.3.2 Canonical Star Formation Relations at Mid-Infrared through Radio Wavelengths

Most infrared-luminous galaxies are considered to be star-forming. With the exception of the very near infrared 1-4 μm emission–which is associated with older stellar populations and often used as a proxy for stellar mass-the bulk of the infrared spectrum is dominated by dust emission. From 5-15 μm, the near-infrared spectrum is dominated by the emission features of polycyclic aromatic hydrocarbons (PAHs). In the mid- and far-infrared, between 20-1000μm, the bulk of the luminosity is thermal emission from warm and cold dust particles. While a certain amount of cool dust will be usually be present in quiescent galaxies, due to dust production by asymptotic giant branch stars, the vast majority of infrared dust emission is associated with active star formation processes and younger stellar populations.

Given the presumed dependence of dust formation on both stellar and gas phase metallicity, we would expect these star formation relations to show significant deviations at low metallicity. Indeed, a wide variety of mid- and far-infrared star-formation measures do demonstrate a clear dependence as function of nebular oxygen abundance, 12+(O/H). In the clearest examples (e.g. Engelbracht *et al.*, 2005, 2008), there is a pronounced metallicity threshold around 12+(O/H)$<$ 8.0, or 1/5th the Solar abundance, below which the metallicity effects become much more pronounced (See Figure 1). The effects are generally understood to be the combined result of altered gas chemistry and impeded molecular cloud formation due to dust depletion, low mid-plane gas pressure in the galaxy disks, and lack of shielding from hard UV radiation. But a detailed picture of star formation in these environments is still an open area of study.

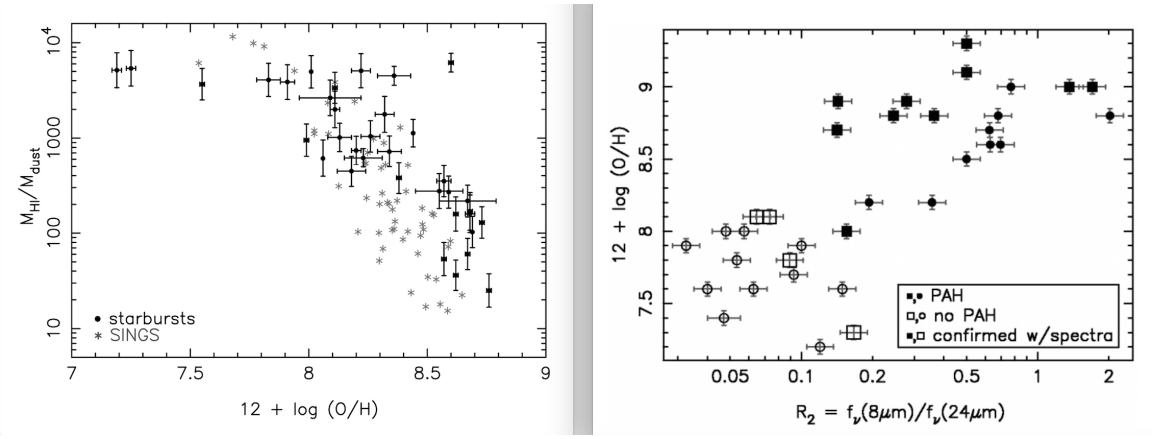

Figure 1: Right: Total gas-to-dust mass ratios for a sample of local bright galaxies and starbursts as function of nebular oxygen abundance, from Engelbracht *et al.* (2008). Left: Mid-infrared flux ratios for the identical sample, as a function nebular oxygen abudance. Reprinted with permission from G. Rieke.

One of the most durable star-forming relationships is the radio/infrared correlation, which relates the continuum radio emission of a starburst to the mid- or far-infrared broad-band emission. Radio continuum has proven to be one of the most reliable tracers of star formation in both the nearby and distant universe, with the radio/IR relationship maintaining 0.3 dex rms over several orders of magnitude (Yun *et al.*, 2001; Schleicher and Beck, 2013). The correlation is found to persist out to redshift of $z \sim 4$ (Bourne *et al.*, 2011; Mao *et al.*, 2011; Pannella *et al.*, 2015), despite predictions that the underlying conditions of the interstellar medium should trigger the modification and eventual breakdown of the relationship at high redshift (Schleicher and Beck, 2013).

When we consider that the physics tying radio continuum emission to star formation rate is not fully understood, the durability of the radio/IR relationship is surprising. Presumably the relationship originates with cosmic rays accelerated by supernova shocks during deaths of short-lived, massive stars in young star forming regions (Condon, 1992; Yun *et al.*, 2001), but the effects of an extremely low metal-

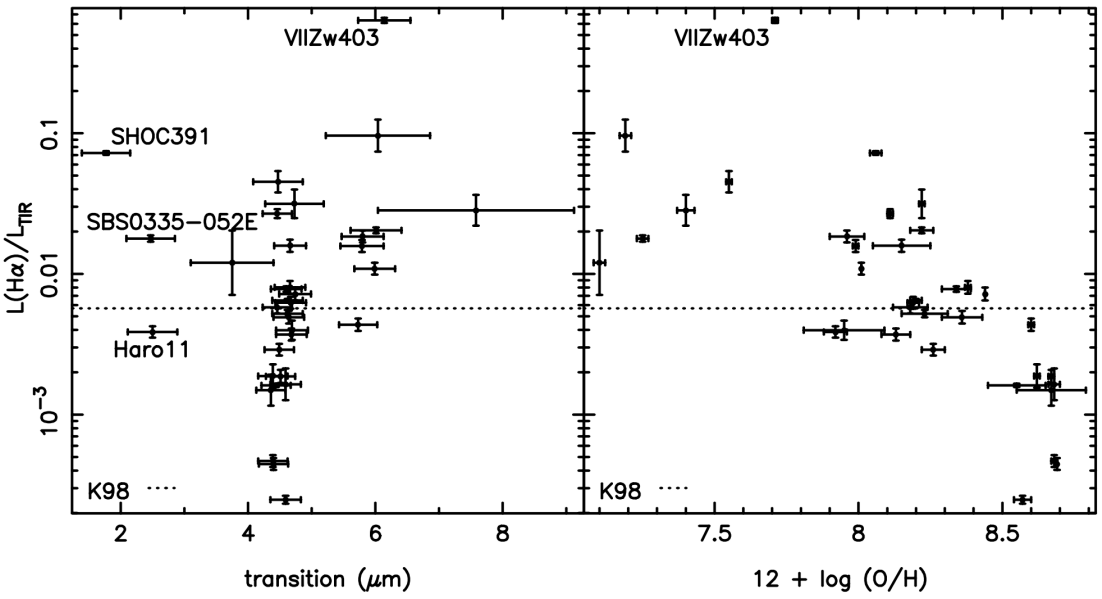

Figure 2: Ratio of Hα luminosity vs. the bolometric total IR (TIR(5-1000μm), as a function of nebular oxygen metallicity $12 + (O/H)$. From Engelbracht *et al.* (2008), reprinted with permission from G. Rieke.

licity environment on this relation are difficult to predict. In the local universe, low-metallicity objects tend to be low-luminosity, and the faint end of the radio continuum/star forming relationship is often constrained by upper limits rather than detections (Chyży *et al.*, 2011; Wu *et al.*, 2008). There are hints of a changes in the relation for galaxies with nebular oxygen abundances of 12+ (O/H)$<$ 8.0, (Wu *et al.*, 2008, Figure 2), though our understanding of this relationship is complicated by the current lack of radio continuum detections for most low-metallicity dwarf galaxies.

1.4 Nebular Oxygen vs. Overall Gas-Phase Metallicity

In the previous sections I discussed the impact of low metallicity on empirical-derived star forming relations as calibrated at various various wavelengths; in the next

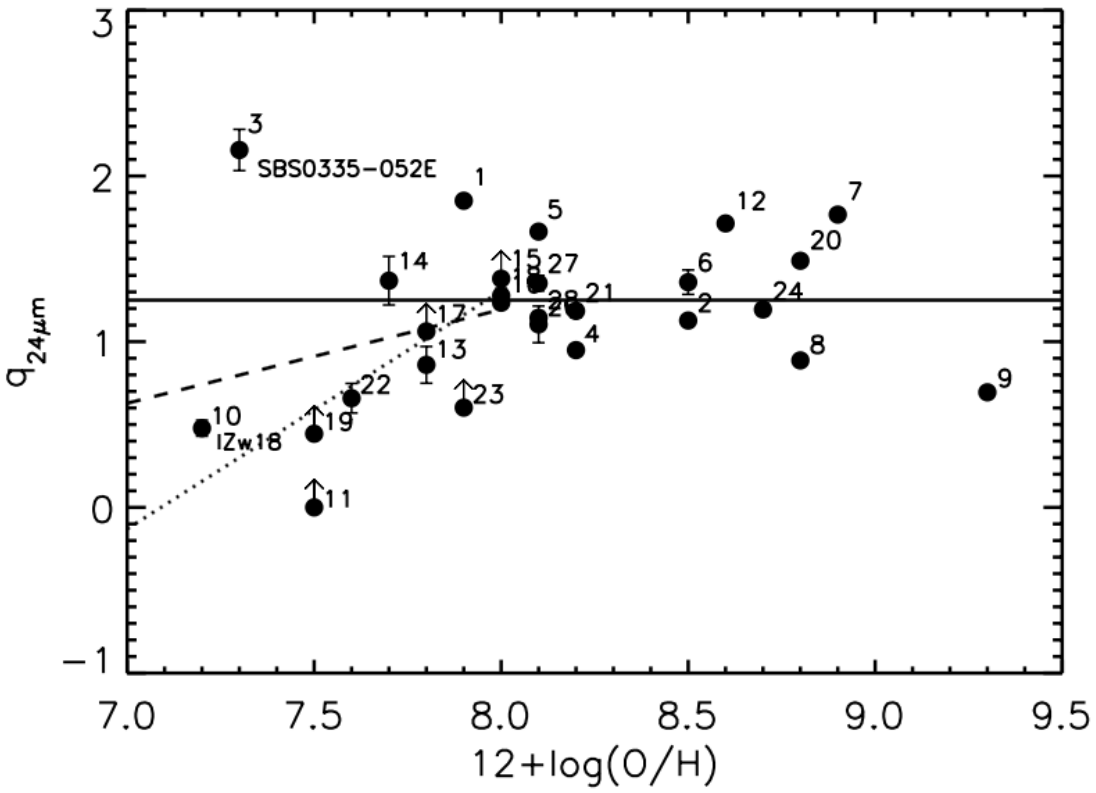

Figure 3: Ratio of 24 μm infrared to 1.4 GHz radio emission q_{24} vs. nebular oxygen metallicity $12 + (O/H)$, for a sample of blue compact dwarf galaxies from (Wu *et al.*, 2008) Figure 3. Wu et al. report that no strong correlation is evident, but a pronounced decrease in q_{24} is evident at metallicities less than $12 + (O/H) < 8.0$, if the exceptional behavior of 1 Zw 18 and SBS 0335-052E is excluded.

chapter, I will use nebular oxygen abundance as the primary criteria for assembling a sample of XMD dwarf galaxies. While it may seem strange to use oxygen abundance as a proxy for overall gas-phase metallicity–or strange to even call it a "metal" to begin with–it is common practice to use nebular oxygen emission lines to estimate the overall abundance of star-forming galaxies. First of all, because oxygen is available and abundant–it is the most common element in the universe after hydrogen and helium. Second, because the forbidden oxygen lines are bright: the [OII]$\lambda\lambda$3727,3729 and [OIII]$\lambda\lambda$ 4959,5007 doublets are easily accessible in visible part of the electromagnetic

spectra, and often have equivalent widths comparable to the Balmer Hα and Hβ lines of hydrogen. This means that oxygen is usually the first element detected after hydrogen in faint or distant extragalactic sources.

A third reason for using oxygen is because it is primarily generated in high-mass stars. Oxygen abundance is therefore tied to core-collapse supernovae, which are the final outcomes of these stars, and mark the release of their nucleosynthetic products into the interstellar medium (see Hinkel, 2012, and references therein). "Metallicity" is after all a misnomer–the term is used to encompass all the chemical elements which could not be created in the Big Bang, and which are therefore the products of stellar nucleosynthesis. These elements serve as a generational marker: as each new generation of stars is formed, it includes the enriched nucleosynthetic output of all the previous generation of stars. Because oxygen production is tied to short-lived, high mass stars, its abundance in the interstellar medium at any given epoch *should be* essentially proportional to the total number of high mass stars that have been formed to date. As previously discussed, many lines of evidence suggest that enriched material is efficiently removed from dwarf galaxies into the IGM, so the oxygen abundance will not truly be proportional to the number of stars formed over the complete history of the galaxy–but this caveat applies to any and all products of stellar nucleosynthesis.

Arguments against using oxygen as a benchmark for overall gas-phase metallicity are associated with uncertainties in measuring its relative abundance. These include both uncertainties in measuring the ionized gas-phase abundance of the interstellar medium, and uncertainties in measuring the Solar photosphere abundance (which serves as a benchmark for the former). These uncertainties are summarized in Chapter 2 and discussed in detail in Appendix 1.

1.5 Gas-Phase Metallicity vs. Stellar Metallicity

Is the gas-phase metallicity a good tracer of the metallicity of the underlying stars? Nebular diagnostics tell us about the global metallicity of the interstellar medium *now*. Because the timescales for high-mass star formation and the onset of core-collapse supernovae are so short ($\sim$ 3 million years), the assumption is generally that the gas-phase metallicity is identical to the current generation of stars. It is difficult to test this assumption observationally. With current 10-meter class telescopes, it is sometimes possible to measure abundances of individual stars in galaxies outside of the Milky Way, provided the stars are very luminous and the galaxies are within the Local Group. Kaufer *et al.* (2004) and Lee *et al.* (2005) obtained high-resolution of a handful of A-type supergiants in two metal-poor Local Group dwarf galaxies, Sextans A and WLM. They find that the measured stellar oxygen abundance of Sextans A is consistent with the nebular abundance of that galaxy, but that the stellar oxygen abundance of WLM is discrepant by ~ 0.6 dex, or a factor of four. (The photospheric abundance of the next-most abundant α-element, magnesium, is in better accord with the nebular oxygen abundance of WLM.) It should be noted, however, that the A-type supergiants used in these studies were chosen for their relative isolation, in order to minimize contamination from other stars. This isolation makes the spectroscopic measurements easier, but means that abundances measured from these stars may not be representative of the star formation in the Sextans A and WLM dwarf galaxies generally.

For galaxies outside of the Local Group, the only data available are integrated spectra, which include contributions from *all* of the stars, including the lower-mass stars left over from previous star-forming epochs. Spectra of of high-mass stars

(spectral types: O,B) are dominated by hydrogen and helium absorption, which are not particularly useful for measuring metallicity; the strong calcium and iron absorption lines in an integrated spectra are largely from low-mass stars (spectral types: G, K, M). Whereas gas-phase metallicities are typically estimated via emission line measures of lighter elements, mostly commonly oxygen, stellar abundances are measured from absorption line spectroscopy of heavier elements, most commonly iron. Like oxygen, iron was originally chosen because it was abundant and fairly easy to measure in stellar photospheres, and subsequently came to be used as a proxy for all the other nucleosynthetic elements–hence the word "metallicity". One of the main problems with using iron is its primary production site in Type Ia supernovae, which have typical timescales tens or even hundreds of millions of years later than core-collapse supernovae.

An advantage of iron is that it is not produced by low-mass stars. This simplifies the interpretation of its photospheric abundance a great deal. It is always necessary to differentiate between the present-day abundances and the zero-age abundances: stars are nucleosynthetic engines, after all, and after a few billion years some enriched material will inevitably wind up in the stellar photosphere. This is a particularly problematic for very low mass K/M- dwarfs and for red giants, which have convective envelopes that penetrate quite deep into the star. Deriving zero-age metallicities from present-day abundances typically requires computational modeling of stellar envelopes. This is simplified greatly if the star's internal nucleosynthetic processes are making only a minimal contribution to the measured abundances–as is the case for iron in low-mass stars.

We have seen the justifications for using oxygen to measure gas phase metallicities and iron to measure stellar abundances, but there remain problems with comparing

iron and oxygen to each other. While oxygen is formed almost exclusively in core-collapse supernovae, iron is primarily produced in Type Ia supernovae. Core-collapse supernovae track the formation of massive stars, with typical timescales of a few million years; Type Ia supernovae require the formation of degenerate binary companions, and have typical timescales of 100s of millions or even billions of years. Oxygen and iron trace very different populations of stars, and so it unsurprising that the ratio [Fe/O] is not constant in different environments (Hinkel, 2012). While the most metal-deficient galaxies known have nebular oxygen abundances of 1/50th solar, the most metal-poor stars in the Milky Way galaxy have [Fe/H] metallicities of 1/10,000th Solar. These so-called Population II stars are largely found in the halo of the Milky Way, and are true artifacts from the epoch of reionization or earlier. The differing timescales of Type Ia vs. core-collapse supernova is clearly seen as an offset in α/[Fe/H] ratios in the oldest stars in the Milky Way disk and halo. We should note that a similar α/[Fe/H] offset is not seen in low metallicity local dwarf galaxies–adding to the evidence that these galaxies are not fundamentally primordial themselves.

Our interpretation of the current gas-phase metallicity and the stellar metallicity is subject to additional uncertainties associated with the exact fraction of enriched material which find its way back into the next generation of stars. There is a well-documented deficit of low-mass, low-metallicity stars in the Milky Way and other nearby galaxies. This shortage, sometimes referred to as the "G-dwarf problem", is typically solved with the inclusion of inflows and outflows to cosmic star-formation models (Tinsley, 1975; Binney and Tremaine, 1987)– as we have established earlier in this chapter, galactic outflows are ubiquitous at all redshifts. Still, it is quite intriguing that to date there have been *no* stars found with the truly primordial metallicities of

Population III, which could be take as indirect evidence for a top-heavy IMF at early times.

1.6 Project Statement

My thesis focuses on understanding the low-mass, low-metallicity behavior of one particular canonical star-forming relationship: the radio/IR correlation. With the recent upgrade of the *JVLA* and initial plans underway for the *Next Generation Very Large Array (ngVLA)*, deep radio interferometry will continue to push into the high redshift ranges that are currently restricted to optical telescopes. At lower redshifts, the upgraded *JVLA* enables the observation of the low luminosity dwarf galaxies which have previously been too faint for detection in the radio continuum (see e.g. Chyży *et al.*, 2011; Wu *et al.*, 2008). Because these non-detections include most of the XMD galaxies in the local universe, a detailed examination of the low metallicity behavior of the radio/IR correlation has been previously out of reach. The primary goal of the project described here is to use the *JVLA* to convert upper limits into true detections, enabling an investigation of the systematic deviations of the radio/IR relation at the low metallicities consistent with the conditions of the first protogalaxies. The subsequent chapters are broken down here:

In Chapter 2, I assemble a complete sample of all currently known low-metallicity galaxies within $d < 50$ Mpc, with nebular oxygen abundances ranging from $7.1 < 12 + (O/H) < 8.1$, or 1/5th and 1/50th of the Solar abundance. This corresponds to the metallicity range between the most metal-deficient objects in the local universe (1 Zw 18 and SBS 0335-552E) at the lower end, and the approximate metallicity of the Small Magellanic Cloud at the upper end. The Small Magellanic Cloud is typically

used as the canonical "low-metallicity galaxy" in many large nearby galaxy surveys, but it would be at the high-metallicity limit of this "extreme" sample. I discuss the overall characteristics of the sample, including volume completeness, phase-space sampling of the mass-metallicity relation, and spatial distribution. Using a smaller sub-sample of galaxies with existing 24 μm mid-infrared detections I construct a smaller representative sample of galaxies to target for radio continuum observations with the *JVLA*.

In Chapter 3, I focus on one of these dwarf galaxies in particular: Sextans A, an extreme dwarf galaxy located within the Local Group. Using the upgraded *JVLA*, I obtain multi-wavelength radio continuum observations of Sextans A. I use the spectral slope of the radio continuum to estimate the relative contributions of the thermal and non-thermal emissions components, and use the latter to calculate the ambient magnetic field strength of the dwarf galaxy. I measure the overall star formation rate of Sextans A, and compare this with the star-formation estimate from narrow-band Hα imaging.

In Chapter 4, I expand my *JVLA* observations to my full infrared-selected sample of 10 dwarf galaxies. These data represent the first radio continuum detections for several of these objects. For each individual galaxy, I explore the spatial relationship between the Hα and radio continuum emission. I examine the radio/IR correlation as a function of nebular oxygen abundance, with the aim of determining if there are systematic deviations in the correlation at extreme low metallicities. Using the Hα emission as a proxy for the "true" star formation rate, I compare the apparent deficiencies in both infrared and radio flux, and discuss the underlying astrophysical processes driving the metallicity behavior of the radio/IR relationship.

In Chapter 5 I summarize my results and conclusions, and discuss future work I

am undertaking to expand this study to include optical and ultraviolet star formation indicators for a larger sample of galaxies.

Chapter 2

ASSEMBLING A TRUE LOW METALLICITY SAMPLE

2.1 Introduction

In this chapter I assemble a sample of extremely metal-deficient (XMD) galaxies. I use the hyperbolic "extremely" to differentiate this sample from traditional local galaxy samples, which typically use "low metallicity" to mean "comparable to the Small Magellanic Cloud," or 1/5 Solar oxygen abundance, 12+(O/H)$\sim$ 8.1. In the previous chapter I argued that this definition of "low metallicity" is insufficient: the most profound changes in the conditions of star formation are observed at nebular oxygen abundances below 12+(O/H)$<$ 8.1. If I am to study the impact of primordial metallicity on the processes of star formation, I must assemble a sample of galaxies with nebular oxygen abudances ranging from the threshold metallicity at 12+ (O/H) $\sim$ 8.1 down to the most metal-deficient environement in the observable Universe (12+ (O/H)$\sim$ 7.0). In the modern universe, all such galaxies will be dwarf galaxies (Tremonti *et al.*, 2004).

In the last two decades, considerable effort has been expended to locate true XMD galaxies. The Sloan Survey Digital Sky Survey (SDSS; York *et al.* (2000); Eisenstein *et al.* (2011); Blanton *et al.* (2017)) has proven a particularly fruitful starting point for candidate XMD searches (Kniazev *et al.*, 2003; Izotov *et al.*, 2006a; Papaderos *et al.*, 2008; Izotov *et al.*, 2012; Guseva *et al.*, 2015; James *et al.*, 2015; Izotov *et al.*, 2018; Senchyna and Stark, 2018). Blind HI surveys such as the Areciebo Legacy Fast ALFA survey (ALFALFA; Haynes *et al.* (2018)) have yielded some of the most extreme

candidates to date (Giovanelli *et al.*, 2013; Hirschauer *et al.*, 2016). The growing list of confirmed and candidate XMDs means that it is rapidly becoming possible to assemble a statistically meaningful sample of XMD galaxies in the local universe. In this chapter, I attempt to do just that.

2.2 Initial Candidate Selection

My initial candidate list is presented in Table 1. These objects were pulled from local surveys of dwarf galaxies (e.g. Kennicutt *et al.*, 2008; Hunter and Elmegreen, 2004; Hunter *et al.*, 2012), dedicated low-metallicity galaxy searches (e.g. Senchyna and Stark, 2018; James *et al.*, 2015; Guseva *et al.*, 2015; Izotov *et al.*, 2006a), and surveys of blue compact galaxies (e.g. Gil de Paz *et al.*, 2003a; Hunter and Elmegreen, 2004; Houck *et al.*, 2004; Wu *et al.*, 2006)). Because archival mid- and far-infrared data is critical (see below), many of the sources came from deep IR surveys of dwarf galaxies (Dale *et al.*, 2009; Engelbracht *et al.*, 2008; Wu *et al.*, 2008; Cigan *et al.*, 2016).

I include the Small Magellanic Cloud as my 12+(O/H)$\sim$ 8.0 reference point, marking the metallicity at which the change in canonical relationships seems to occur; the SMC is too far south to be observed from the Northern hemisphere, but has already been observed extensively by other authors at almost every conceivable wavelength. A handful of other well-studied Local Group dwarfs and blue compact galaxies with multi-wavelength data and 12+(O/H)$<$ 8.0 have been included as higher metallicity "anchors", bridging the gap between the XMD sample and the more traditional "sub-Solar" metallicity dwarfs, with 8.0 $>$ 12+(O/H)$>$ 8.6 The highest metallicity galaxy is IC 10, with 12+(O/H)= 8.35.

Table 1: Summary table of candidate low-metallicity galaxies within 100 Mpc.

Galaxy	RA [h:m:s]	Dec [d:m:s]	cz[a] [km/s]	D [Mpc]	Metallicity $[12+(O/H)]$	m_B[a] [mag]	$E(B-V)$[b] [mag]	Type	Ref
WLM	00:01:58.1	-15:27:39.3	-122	0.92	7.83	11.03	0.033	dIRR	1, 14
IC 10	00:20:17.3	+59:18:13.6	-348	0.7	8.35	11.8	1.386	dIRR	2, 15
Haro 11	00:36:52.5	-33:33:16.8	6175	84	7.9	13.8	0.010	BCD	13, 16
SMC	00:52:44.8	-72:49:43.0	158	0.06	7.98	2.7	0.037	dIRR	1, 17
J0100+0028	01:00:56.9	-00:28:43.9	5752	76.5	7.10	20.9g	0.031	BCD	13, 18
IC 1613	01:04:47.8	+02:07:04.0	-234	0.73	7.86	9.88	0.22	dIRR	3, 17
UGC 772	01:13:40.4	+00:52:39.1	1128	15.5	7.26	20.1g	0.024	BCD	13, 19
SBS 0335-052E	03:37:44.1	-05:02:40.2	4053	53.8	7.30	17.7b	0.041	BCD	13, 20
SBS 0335-052W	03:37:38.4	-05:02:37.5	4038	53.6	7.13	19.5b	0.041	BCD	13, 20
NGC 1569	04:30:49.0	+64:50:52.6	-104	3.06	8.2	11.86	0.613	BCD	4, 21
II Zw 40	05:55:42.6	+03.23.32.0	789	11.1	8.06	15.48	0.728	BCD	13, 22
KUG 0743+513	07:47:33.2	+51:11:24.8	454	8.9	7.74	14.8	0.063	BCD	13, 23

Continued on next page

Table 1 – continued from previous page

Galaxy	RA [h:m:s]	Dec [d:m:s]	cz[a] [km/s]	D [Mpc]	Metallicity $[12+(O/H)]$	m_B[a] [mag]	$E(B-V)$[b] [mag]	Type	Ref
J0811+4730	08:11:52.1	+47:30:26.24	13324	184	6.98	21.4g	0.058	BCD	13, 24
HS 0822+3542	08:25:55.5	+35:32:31.9	727	12.6	7.4	18.05	0.041	BCD	13, 25
UGC 4483	08:37:03.0	+69:46:31.0	156	3.2	7.53	15.1	0.030	BCD	5, 26
UGC 4704	08:59:00.3	+39:12:35.7	596	10.4		15.33	0.026	dIRR	13, 27
I Zw 18	09:34:02.0	+55:14:28.1	751	18.2	7.17	16.05	0.030	BCD	6, 28
SBS 0940+544	09:44:16.6	+54:11:34.2	1638	27.8	7.48	17.18	0.012	BCD	13, 29
Leoncino	09:43:32.4	+33:26:57.6	514	7.7	7.02	19.8g	0.012	dIrr	7, 7
DDO 68	09:56:45.7	+28:49:35.0	503	12.1	7.20	14.7	0.018	dIrr	8, 8
Leo A	09:59:26.5	+30:44:47.0	20	0.83	7.38	12.92	0.018	dIrr	9, 30
Sextans B	10:10:10.1	+04:19:56.0	301	1.32	7.53	11.85	0.032	dIrr	10, 31
Sextans A	10:11:00.8	-04:41:34.0	324	1.32	7.54	11.86	0.039	dIrr	1, 31
KUG 1013+381	10:16:24.5	+37:54:46.0	1173	21.6	7.58	15.9g	0.013	BCD	13, 32

Continued on next page

Table 1 – continued from previous page

Galaxy	RA [h:m:s]	Dec [d:m:s]	cz[a] [km/s]	D [Mpc]	Metallicity $[12+(O/H)]$	m_B[a] [mag]	$E(B-V)$[b] [mag]	Type	Ref
Leo P	10:21:45.1	+18:05:17.0	264[33]	1.72	7.17	17.25[34]	0.026	dIrr	11,35
SBS 1102+606	11:05:53.7	+60:22:28.7	1340	24.5	7.64	16.4g	0.005	BCD	13, 36
Mrk 170	11:26:00.8	+64:08:16.6	982	19.4	8.09	15.0	0.009	BCD	13, 19
VII Zw 403	11:27:59.9	+78:59:39.0	-103	4.34	7.7	14.5	0.033	BCD	1, 37
SBS 1129+576	11:32:02.5	+57:22:45.6	1566	27.9	7.42	16.50	0.012	BCD	13, 38
UM 461	11:51:33.3	-02:22:21.9	1039	12.7	7.8	16.87	0.015	BCD	13, 39
UM 462	11:52:37.2s	-02:28:09.9	1057	13.5	7.91	14.50	0.017	BCD	13, 39
SBS 1159+545	12:02:02.4	+54:15:49.6	3592	55.4	7.49	18.0	0.015	BCD	13, 37
UGCA 292	12:38:40.0	+32:46:00.5	309	3.1	7.27	16.00	0.013	dIrr	12,40
GR 8	12:58:40.4	+14:13:03.0	214	2.13	7.65	14.68	0.023	dIrr	1,31
DDO 178	14:15:56.5	+23:03:19.0	153	2.24	7.79	14.38	0.021	BCD	1,41
SBS 1415+437	14:17:01.4	+43:30:05.5	609	12.8	7.59	15.6	0.009	BCD	13, 37

Continued on next page

Table 1 – continued from previous page

Galaxy	RA	Dec	cz[a]	D	Metallicity	m_B[a]	$E(B-V)$[b]	Type	Ref
	[h:m:s]	[d:m:s]	[km/s]	[Mpc]	$[12+(O/H)]$	[mag]	[mag]		
SHOC 567	17:19:42.1	+61:18:51.7	3501	56	7.31	15.7	0.022	BCD	13, 42
J2104-0035	21 04 55.3	-00 35 22.0	1313	21.4	7.17	18.0	0.057	BCD	13, 18
Pegasus	23:28:36.2	+14:44:34.5	-183	0.94	7.92	12.50	0.060	dIrr	3, 43

[a] Recession velocities cz and apparent Johnson B magnitudes m_B are taken from the NASA Extragalactic Database (NED), excepted where noted in the table. Where Johnson B was not available, Sloan b or g was listed instead.

[b] NED derives Galactic reddening values $E(B-V)$ from Schlafly and Finkbeiner (2011). See section 2.2.1 for more details.

References: *Distance measurements from:* (1) Kennicutt *et al.* (2008, (references from Table 1)); (2) Ferrarese *et al.* (2000); (3) Tammann *et al.* (2011); (4) Grocholski *et al.* (2012); (5) Karachentsev (2005); (6) Aloisi *et al.* (2007); (7) Hirschauer *et al.* (2016); (8) Berg *et al.* (2012); Pustilnik *et al.* (2005); (9) Tammann *et al.* (2011); Bernard *et al.* (2013); (10) Tammann *et al.* (2011); Sakai *et al.* (1997); (11) McQuinn *et al.* (2013); (12) Karachentsev *et al.* (2004); (13) Virgocentric flow model of Mould *et al.* (2000), see section 2.2.1.

(O/H) *measurements from:* (14) Lee *et al.* (2005); (15) Magrini and Gonçalves (2009); Tehrani *et al.* (2017); (16) Bergvall and Östlin (2002); (17) Sakai *et al.* (2004); (18) Guseva *et al.* (2015); (19) Izotov *et al.* (2006a); (20) Izotov *et al.* (2009); (21) Kobulnicky and Skillman (1997); (22) Guseva *et al.* (2000); (23) Izotov and Thuan (2007); (24) Izotov *et al.* (2018); (25) Izotov *et al.* (2006b); (26) van Zee and Haynes (2006); (27) this work; (28) Skillman and Kennicutt (1993); (29) Thuan and Izotov (2005); (30) van Zee *et al.* (2006); (31) Kniazev *et al.* (2005); (32) Kniazev *et al.* (1998); (33) Giovanelli *et al.* (2013); (34) Rhode *et al.* (2013); (35) Skillman *et al.* (2013); (36) Kniazev *et al.* (2003); (37) Izotov and Thuan (1999); (38) Guseva *et al.* (2003); (39) Izotov *et al.* (2006b); Kniazev *et al.* (2004); (40) van Zee (2000); van Zee and Haynes (2006); (41) Lee *et al.* (2003); van Zee *et al.* (1997); (42) Kniazev *et al.* (2004); (43) Skillman *et al.* (1997).

2.2.1 Fundamental Parameters

Recession velocities, apparent B magnitudes, Galactic extinction were obtained from the NASA Extragalactic Database (NED), unless otherwise noted in 1. Galactic reddening values $E(B-V)$ are derived from the Schlafly and Finkbeiner (2011) recalibration of the Schlegel *et al.* (1998) *COBE/DIRBE* dust map, using a different source spectrum and $R_V = 3.1$ reddening law taken from Fitzpatrick (1999).

Because most of the galaxies in my initial sample are within 30 Mpc, local gravitational perturbations and peculiar velocities dominate over the cosmological Hubble flow of the expanding universes. Particularly for galaxies within the local volume ($d < 11$ Mpc) distances cannot be reliably determined from recessions velocities alone, and "direct" distance estimates from standard candle methods are preferred. Kennicutt *et al.* (2008) (hereafter K08) have compiled a near-comprehensive list of direct distance measures for objects within 11 Mpc. A handful of nearby dwarf galaxies (e.g. Sextans B, Leo A) are not included in the K08 sample, but have do have direct distance measurements in the literature. Wherever possible, direct distances from resolved stellar population methods (e.g. Cepheid or RR Lyrae variables; tip of the red giant branch; brightest blue stars; planetary nebulae luminosity function, etc.) are used. A few other galaxies (UGC 4483, DDO 68) have distances estimated via the Tully-Fisher method, which uses integrated luminosity of the galaxy to infer the luminosity distance, The Tully-Fisher technique is not an ideal technique for estimating individual galaxy distances due to its large intrinsic uncertainties– still, any standard candle distance is better than better than relying on recession velocity alone. This is especially true for objects around the Galactic North Pole, where the

gravitational effects of the Virgo Cluster and Great Attractor typically overwhelm the cosmological expansion.

For galaxies without direct distance estimates, I use the cosmological velocity flow model of Mould *et al.* (2000, Appendix A), assuming a Hubble constant of 73 km/s/Mpc, (lambda CDM), and including the optional terms to account for the Virgocentric inflow, the Great Attractor, and the Shapley supercluster (Virgo + GA + Shapley) . For galaxies which lie in the general direction of Virgo ($\alpha \sim 13°$, $\delta \sim 20°$), these perturbations have a 20% - 30% impact on luminosity distance estimates.

2.2.2 Nebular Oxygen Abundance Criteria

Low metallicity is clearly the key criteria for my study. In keeping with the rest of extragalactic astronomy, I use nebular oxygen as a proxy for all nucleosynthetic Oxygen is popular in this context in part due to its comparative abundance in the Universe, and for its extremely bright emission lines in the visible spectrum. There are two primary sources of uncertainty in assigning a single metallicity determination for an individual galaxy: 1.) systematic uncertainties associated with different abundance estimators, and 2.) the intrinsic metallicity spread between multiple star forming regions within a single galaxy.

Nebular oxygen metallicities listed in the table have been determined by several different methods, depending on the available data; not all of these methods will yield identical metallicities for identical line ratios. The "direct" method is generally considered the more reliable metallicity determination, but requires the measurement of the measurement of the [OIII]λ4363Å line, which has typically 2-10% of the flux of

the bright lines (see e.g. Figure 5.1 from Osterbrock, or Izotov *et al.*, 1994), and may be blended with the bright Hγ in low-resolution spectra.

For fainter galaxies it will often be possible to measure [OIII]λ5007Å and[OIII]λ4959Å with high signal-to-noise, while [OIII]λ4363Å remains in the noise. This situation has caused authors to develop several "empirical" methods of estimating the flux from the bright lines alone. Historically, R_{23} is the most popular method, because it uses the very brightest lines in an HII or PNe spectrum, which are easily observed via low-resolution spectroscopy on small aperture telescopes (1-2 meters). Using SDSS spectra for 53,000 galaxies, Tremonti *et al.* (2004, (T04)) demonstrate the uncertainties associated with the R_{23} method for oxygen abundances between $9.5 < 12 + (O/H) < 8.0$ (see Figure 30). T04 determines

However, in recent years, with the increasing availability of large ($<$ 6-10 meter) aperture telescopes, which allow reliable measurements of the [OIII]λ4363Å line, the "direct" method is becoming more popular. The Izotov et al. collaboration prefer to use "direct" method (two zone model) They have developed their own "semi-empirical" method Stasińska and Izotov (2003) which uses the traditional bright lines, but For the galaxies with both measurement, there does appear to be systematic offsets between the metallicities measured via the two methods (see Izotov and Thuan (2007) Table 5)

An additional source of metallicity uncertainty is the intrinsic metallicity variation within the galaxies themselves. For compact galaxies at low resolution, when an entire angular extent of the galaxies fits within a single SDSS fiber, it makes sense to talk of the integrated spectral properties of an entire galaxies, and assign a single integrated metallicity. At higher resolution, however, this treatment always breaks down. For galaxies in the local volume ($<$ 11 Mpc), and particular within the Local Group, it is easily possible to distinguish multiple discrete HII regions and even PNe, and obtain

separate metallicity estimates for each (Magrini *et al.*, 2003; Kniazev *et al.*, 2005). Metallicity gradients with galactocentric distance Even SBS 0335-052E/W is still close enough to separate into multiple HII regions from the ground with a powerful telescope at an excellent site: (Izotov *et al.*, 2009). Where available, resolved region-to-region metallicities within a single galaxy typically exhibit a range of $\sim 0.2 - 0.3$ in (O/H) abundance. I therefore assume a metallicity uncertainty of ± 0.2 in all cited values of $12 + (O/H)$ values.

Metallicities are traditionally benchmarked against the Solar abundance, but it is potentially tricky to compare nebular oxygen abundance (which is measured in emission) against abundance measurements from the Solar photosphere (which are measured in absorption). The Solar oxygen abundance has proven particularly difficult to nail down: In the past decade, advance in 3D atmospheres and non-LTE modeling brought the accepted value down quite sharply from $\sim$ 8.9 in 1989 (Anders and Grevesse, 1989) to $\sim$ 8.6 - 8.7 (Asplund *et al.*, 2005). The primary diagnostic is a forbidden transition, the [OI] 630nm line, which is blended with a Ni I line. Other transitions are available, but these either have their own issues with blending or have significant on non-LTE effects. Currently the most self-consistent determinations come from models in which the Ni abundance is determined independently before oxygen is addressed (Scott *et al.*, 2009). (For a full discussion, see review by Asplund *et al.*, 2009, and references therein.) Asplund's review recommends a Solar oxygen value of $12 + (O/H) = 8.69 \pm 0.05$. The updated value is now a decade old, but until fairly recently it was common to find the higher Anders & Grevasse 1989 value quoted in extragalactic papers.

Assuming a Solar metallicity of 8.69, then, the Small Magellanic Cloud has an abundance of $\sim 1/5$th Solar.

2.3 Narrowing the Sample

In order to achieve the basic science goals outlined in Chapter 1, i.e. confirming or refuting the impact of extreme low-metallicity environments on the radio/IR relation, I require a galaxy sample that meets certain base criteria.

- Low nebular oxygen abundance, $12 + (O/H) < 8.2$.
- Existing mid- and far-infrared detections.
- Visible in the Northern hemisphere
- Range of galaxy luminosities and star-forming intensities

In order to examine the IR/radio correlation, I will require both infrared and radio detections for a $N > 10$ low-metallicity objects. Broad-band continuum radio data can be obtained from the ground, but mid- and far-infrared detections will require archival space-based observations. This requirement automatically excludes several significant XMDs, in particular Leoncino, Leo P, and J0811+4730 (Hirschauer *et al.*, 2016; Giovanelli *et al.*, 2013; Izotov *et al.*, 2018). Despite their significance as some of the the lowest metallicity objects in the known universe, the recentness of their discovery means that they do not yet have mid- or far-infrared imagery. There are currently no ongoing space-based missions capable of obtaining these data, or plans to launch one in the near future; the only viable mid- and far-infrared telescope currently in operation is the air-borne *SOFIA* mission. The 5-40 μm FORCAST (The Faint Object infraRed CAmera for the *SOFIA* Telescope) lacks the sensitivity to detect all but the brightest of my sources at 24 μm, and sensitivity only worsens at longer wavelenghts[4].

[4] *SOFIA* Instrument Time Estimator: https://dcs.sofia.usra.edu/proposalDevelopment/SITE/

Because my ground-based observations use telescopes located in Arizona and New Mexico, I will only able to observe galaxies which are visible from the Northern Hemisphere. This requirement immediately eliminates the Small Magellanic Cloud and Haro 11 (though some archival data are available for both of these objects). Another luminous BCD, SHOC 567, was eliminated due to a combination of its large distance and awkward right ascension (α = 17h). Fortunately, most of the known XMDs are visible from the Northern hemisphere, due in large part to the productivity of the Second of the Byurakan Survey(SBS; Markaryan *et al.* (1983); Stepanian (2005)) in Armenia, SDSS in New Mexico, and ALFALFA in Puerto Rico.

2.3.1 Optional Criteria

There are numerous additional criteria which would be desirable for an "ideal" sample, but which were deemed impractical for the purposes of this study. Thers "optional" criteria included:

- Pre-existing $H\alpha$ imaging
- Not obscured by the Milky Way
- Within 11 Mpc.

Hα provides another estimate of the star formation rate, which is (mostly– Calzetti *et al.*, 2007) independent of the IR and radio continuum. Emission line imaging is generally superior to slit spectroscopy for nearby galaxies with large angular sizes, as it captures the contribution from diffuse flux that would fall outside the slit. Archival Hα imaging and published fluxes are available for 60% of the galaxies in this sample.

11 Mpc is the edge of the "local volume", as defined by Dale *et al.* (2009). While there are many low luminosity dwarf irregulars (dIRRs) within this volume which meet

the criteria for XMDs, introducing e.g. a 11-Mpc distance cut would automatically exclude the five lowest metallicity galaxies in the known Universe, I Zw 18, Leoncino, J0100+0028, and SBS 0335-052E/W. In fact, none of the blue compact dwarfs (BCDs) which match the metallicity criteria are found within $d < 11$ Mpc, so restricting the sample to the local volume would remove all higher luminosity XMDs–which are commonly expected to be the better protogalaxy analogs! Moreover, in order to disentangle the effects of low luminosity vs. low metallicity on the radio/IR relationship, I will need to adequately sample a wide parameter space for both. The 11 Mpc distance limit is therefore not appropriate for this study.

In general extragalactic surveys try to avoid the plane of the Milky Way galaxy itself, due to large galactic foregrounds, dust extinction, and reddening. Unfortuantely, of the few low-metallicity BCDs within the local volume, three of the most luminous– IC10, NGC1569, and II Zw 40– are located close the Galactic planet, at galactic latitude of $b < 15°$. Hα and optical fluxes from these galaxies are subject to extreme dust extinction and uncertainty. However, their radio and mid-infrared fluxes should be easily disentagled from Galactic foregrounds, so I include them in my final sample.

2.3.2 Final Low-Metallicity Dwarf Sample

I list my final sample of low-metallicity dwarf galaxies in Table 2. All of these objects meet the requirement for archival mid- or far-infrared data, are at declinations north of $\delta > -10°$. All but one of these galaxies (II Zw 40) are true XMDs, with 12+ (O/H) < 7.6. The distance requirement of $d < 11$ Mpc was not met, due to the paucity of luminous XMD sources within the local volume.

Archival Hα and near-infrared 4.5 μm luminosities are used to estimate the total

star formation rate and total stellar mass. The Hα luminosities come from emission-line imaging, rather than spectroscopy (Gil de Paz *et al.*, 2003b; Kennicutt *et al.*, 2008), and have been corrected for intervening dust extinction, but not for internet extinction or the contribution of [NII] emission. The luminosities list here do not necessarily match the literature values, due to different Hubble constants and distance moduli in the various references. If not accounted for, these mismatches could lead to systematic offsets in estimated star formation rate. For the purposes of this study, I have scaled all luminosities to match the distances given in Table 1, and re-calculated the estimated star formation rates accordingly.

Table 2: Sub-sample of low-metallicity galaxies with archival mid- or far-infrared Spitzer data

Galaxy	$f_{H\alpha}$[a]	$L_{H\alpha}$[a]	$f_{4.5\mu m}$	$L_{4.5\mu m}$	IR data	Ref
	$[log(\mathrm{ergs/s/cm^2})]$	$[log(\mathrm{ergs/s})]$	[Jy]	$[log(\mathrm{ergs/s})]$	[μm]	
SBS 0335-052E	-12.49 ± 0.01	41.05	1.63E-03 ± 4.9E-05	40.95	MIPS 24-160	1, 4
SBS 0335-052W	-13.84 ± 0.02	39.70	3.47E-05 ± 2.6E-06	39.28	(b)	1, 4
II Zw 40	-11.64 ± 0.02	40.53	1.83E-02 ± 5.5E-04	40.63	MIPS 24-160	3, 5
HS 0822+3542	-13.13 ± 0.05	39.15	8.89E-05 ± 3.5E-06	38.43	MIPS 24,70	2, 4
UGC 4704	-12.86 ± 0.06	39.26	5.63E-03 ± 7.7E-04	40.07	MIPS 24-160	3, 5
I Zw 18	-12.45 ± 0.03	40.15	3.51E-04 ± 1.2E-05	39.35	MIPS 24,70	2, 4
SBS 0940+544	-13.29 ± 0.04	39.68	5.11E-05 ± 1.0E-06	38.88	MIPS 24	2, 6
Leo A	-12.84 ± 0.22	37.08	1.36E-02 ± 1.9E-03	38.25	MIPS 70,160	3, 7
Sextans B	-12.2 ± 0.10	38.12	3.61E-02 ± 5.0E-03	39.08	MIPS 24-160	3, 7
Sextans A	-11.6 ± 0.07	38.65	2.49E-02 ± 3.4E-03	38.92	MIPS 24-160	3, 7
SBS 1129+576	(c)	(c)	(d)	(d)	IRS 16, 22	8
SBS 1415+437	-12.30 ± 0.05	39.73	2.96E-04 ± 9.3E-07	38.71	MIPS 24	2, 6

[a] While Kennicutt *et al.* (2008)(K08) spectroscopically measures the Hα/ [NII] ratio and subtracts the fraction of the total flux attributed to [NII], Gil de Paz *et al.* (2003b) (gdP03b) makes no attempt to do so. In order to insure consistency between samples, I add the contribution of [NII] back into the K08 fluxes. While the Hα/ [NII] ratio can range up to ~ 0.5 in normal spirals, in these low metallicity dwarfs the typical range is 0.04-0.08, with [NII] contributions never exceeding 10%.

[b] The small separation on the sky between the East and West components of SBS 0335-052 make the pair impossible to separate with the large MIPS beam. >90% or more of the flux is assumed to come from the Eastern dwarf.

[c] No Hα data for SBS 1129+576 is available in the literature. I have obtained Hα+ [NII] emission-line imaging of this object at the Kuiper 61-inch telescope during an observing campaign in February and March of 2016, which will be presented in a later work. SBS 1129+576 is omitted from the Hα star formation comparisons in both Chapters 2 and 4.

[d] IRAC 3.6 and 4.5 μm imaging for SBS 1129+576 was obtained by Houck et al, but is unpublished. In the absence of near-infrared photometry, it is still possible to estimate the the stellar mass with SED-modeling from the published SDSS + MIPS photometry.

Hα references: (1) Pustilnik *et al.* (2004); (2) gdP03b; (3) K08;

4.5μm and mid-infrared references: (4) Engelbracht *et al.* (2008); (5) Dale *et al.* (2009); (6) Capak *et al.* (2013); (7) P. Cigan, priv. communication; (8) Wu *et al.* (2006).

2.4 Sample Characteristics

A multitude of surveys contributed to the full list of XMD galaxies included in Table 1 and 2, resulting in a very inhomogenous mixture of sampling biases. Before attempting to draw conclusions about the bulk star formation properties of XMDs, it is necessary examine the bulk properties of the proposed sample in terms of volume completeness, luminosity coverage, and spatial distribution.

2.4.1 Assessing Volume Completeness

Volume-limited samples are considered the gold standard of low-redshift observational astronomy, and for good reason. Large-volume surveys are magnitude-limited by default, which translates to higher limiting luminosities at larger distances, introducing a bias towards brighter sources at earlier cosmological eras. This makes it difficult to e.g. measure the evolution of the luminosity functions compare similar galaxies populations at different cosmic ages (Bothun (1998), chapter 6; Hikage *et al.* (2003) section 4). When studying dwarf galaxies, this problem can become acute–beyond 20-30 Mpc, the vast majority of the dwarf galaxy population falls below the magnitude limits of the SDSS.

A casual examination of the local low-metallicity sample in Table 1 shows some evidence for luminosity bias: most of the galaxies can be divided into roughly into two general classes: local dwarf irregulars (dIrrs) and blue compact dwarfs (BCDs). BCDs are named for their optically blue colors and compact angular sizes on the sky, and are often the sites of intense starburst activity. Extremely metal-deficient BCDs are rarities in the modern universe; there are none in the Local Group. Lower-luminosity

dwarf irregulars with are much more common, but also much more difficult to detect at large distances. Consequently almost all of the BCDs in the sample are at $d > 15$ Mpc, while most of the dIRRs are at $d < 15$ Mpc.

In order to evaluate the volume completeness of my sample, I plot the B-band luminosities vs. galaxy distance (Figure 4). As expected, the more luminous BCD galaxies are at larger distances, while the less luminous dIrrs are within the Local Group or its immediate neighborhood. The sample is consistent with an apparent magnitude limit of $m_B \sim 20.5$. The density of sources at $d < 15$ Mpc vs. the comparative sparseness at $d > 15$ Mpc suggests that most XMD galaxies within the Virgo supercluster have yet to be discovered: recall that the volume enclosed increases as $\sim d^{\,2}$, so a volume complete sample would exhibit a geometric increase in source density with distance.

For comparison, I overplot the my sample in Figure 5 with the volume-complete Local Volume Legacy survey (LVL; Dale *et al.*, 2009)). The LVL is the current state-of-the-art in surveys of the local galaxy population, combining multi-wavelength data from 11 Hα and UV Galaxy Survey (11HUGS; Lee *et al.*, 2004, 2009b) survey with the ACS Nearby Galaxy Survey Treasury (ANGST; Dalcanton *et al.*, 2009). The differing luminosity limits of these two surveys can be clearly seen in Figure 5: ANGST is both volume complete and luminosity limited within 3.5 Mpc, while 11HUGS is magnitude-limited out to 11 Mpc. Both surveys are designed to be volume complete within their given luminosity limits. At any given luminosity, the number density of sources in the combined LVL sample generally increases with distance (though the number density peaks at 8 Mpc, rather than 11 Mpc, due to the local overdensity structure of galaxy groups between the Local Group and the Virgo Cluster–see Section 2.4.3.)

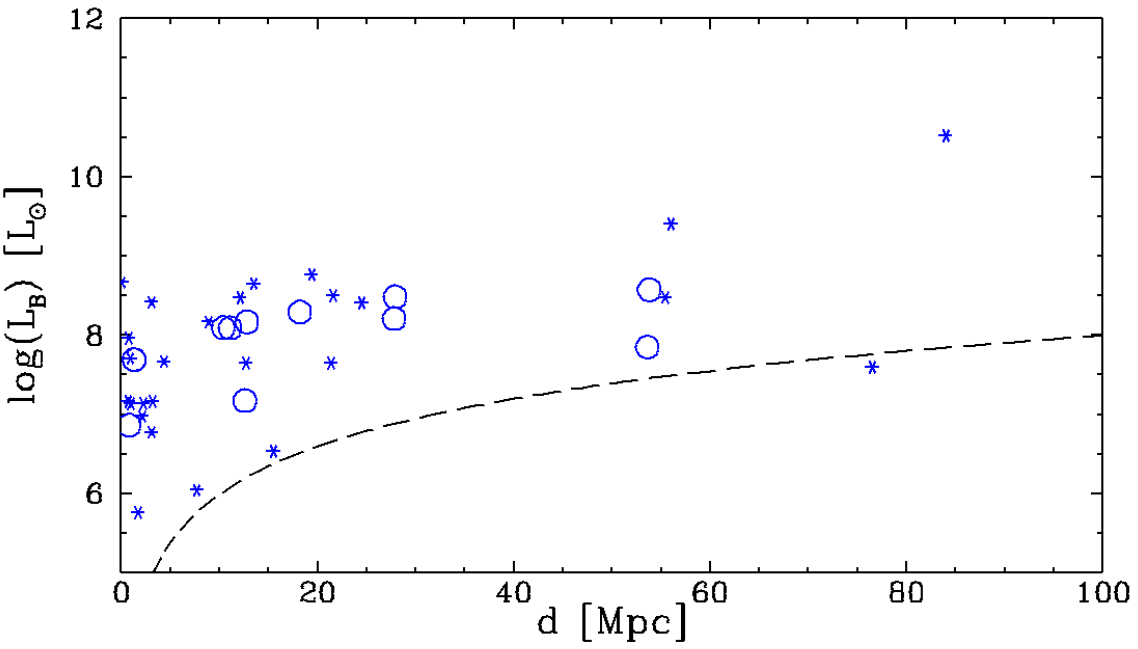

Figure 4: Luminosity-distance distribution of the low-metallicity sample. Large blue open circles are the galaxies with archival mid-infrared *Spitzer* photometry, which will be be used for later chapters (see Table 2). Blue asterisks are the remainder of the low-metallicity sample from Table 1. The dashed line the $m_B = 20.5$ apparent magnitude limit. The low-metallicity sample is weakly magnitude-limited, and does not show an obvious luminosity bias. The increasing sparseness with distance suggests that the sample likely not volume complete beyond $d < 2 - 3$ Mpc.

In contrast, the number density of the XMD sample decreases with distance, consistent with incomplete sampling, though the XMD sample includes proportionally more low luminosity dwarf galaxies. Incomplete sampling means that I will not be able to estimate the XMD galaxy luminosity function, and I make no attempt to do so in this work. The luminosity function will be a critical piece of information for future studies, as low luminosity Lyman continuum leakers could be a hidden contributor to the ionizing background at high redshifts.

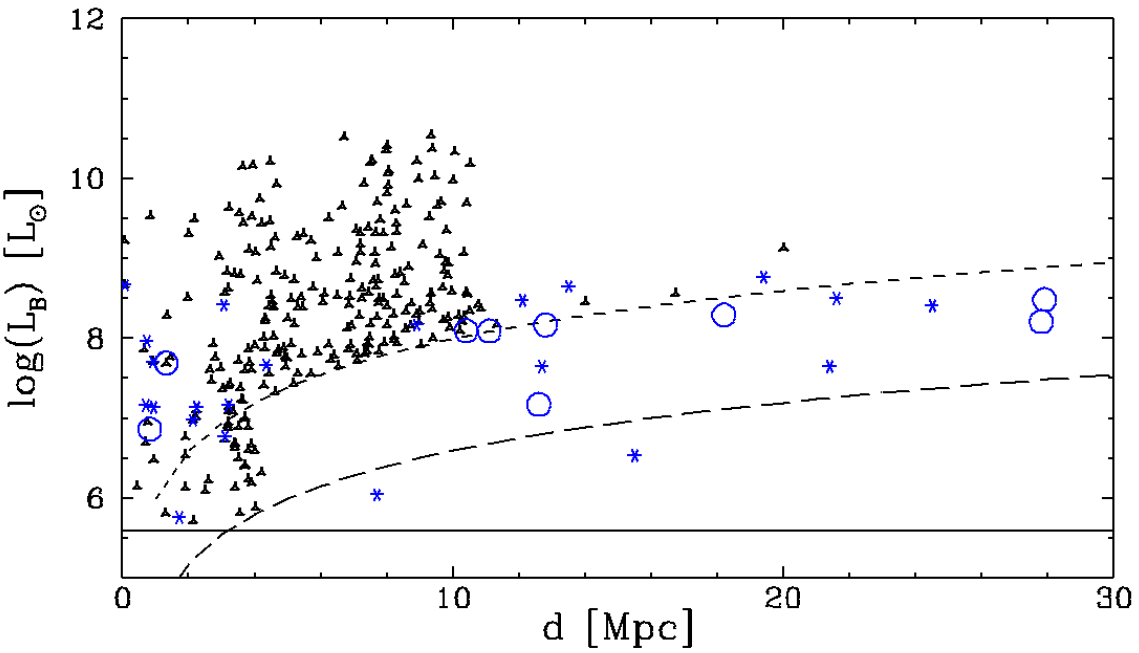

Figure 5: Luminosity-distance of the low-metallicity sample vs. the Local Volume Legacy survey (LVL; black triangles). LVL B magnitudes are from Dale *et al.* (2009). Markers are identical to Figure 4. The two surveys which contribute to the LVL–the volume-limited 3.5 Mpc ANGST survey, and the 11Mpc magnitude-limited 11HUGS survey– are easily distinguished. The short-dashed line is the $m_B = 15$ magnitude limit of the 11HUGS survey. The long-dashed line is the $m_B = 19.0$ magnitude limit. The solid line is the luminosity limit $log(L_B) = 5.6L\odot$, which corresponds to an apparent magnitude of $m_B = 20.0$ at 5 Mpc. In comparison with the LVL, my low-metallicity sample is more strongly weighted toward low-luminosity dwarf galaxies.

2.4.2 Luminosity-Metallicity Relation

Following the $z = 0$ luminosity-metallicity (L-Z) relation (Tremonti *et al.*, 2004), I expect that most XMD galaxies in the modern universe will be dwarfs, with shallow gravitational potentials that permit the enriching products of stellar nucleosynthesis to escape into the IGM before they can be incorporated into the next generation of stellar formation. But the L-Z relation itself exhibits > 2 magnitudes of dispersion

at any given metallicity, reflecting the great variety of individual galaxy assembly histories.

In Figure **??**, I overplot the full XMD sample on the B-band L-Z relationship for the LVL sample. The XMD sample spans the expected available luminosity range for 12+ (O/H)$<$ 8.1, and then some: while the Local Group dIrrs (such as Sextans A/B and Leo A) populate the natural low-metallicity extension of the L-Z relation, the BCD population is shifted well to the right, consistent with their higher star formation rates. This confirms that I am indeed oversampling the rarer, more luminous objects by including the BCDs. The full XMD sample ranges over *5 orders of magnitude* in luminosity, compared to the $\sim$ 1.0 dex spread of the main L-Z relation. My final archival IR sample (Table 2) excludes both the faintest and most luminous extremes, but still spans a factor of 100 in luminosity.

There is automatically some tension between sampling the full spread of the XMD luminosity-metallicity relation vs. creating a volumetrically complete sample. Referring to the previous section, it may be possible construct a volume complete sample within the nearest $\sim$ 2 Mpc, but this would exclude the rarer blue compact dwarfs. For this study, I sacrifice representative completeness for greater luminosity parameter space, and include the more-distance BCDs in my final sample (Table 2).

2.4.3 The Spatial Distribution of Low-Metallicity Galaxies in the Local Universe

Another outstanding feature of the galaxies in Table 1 is the concentration of sources at right ascensions 8.5h $< \alpha <$ 10.5h, and the relative absence in other parts of the sky. This feature is likely real: while the XMD sample is presumed to be

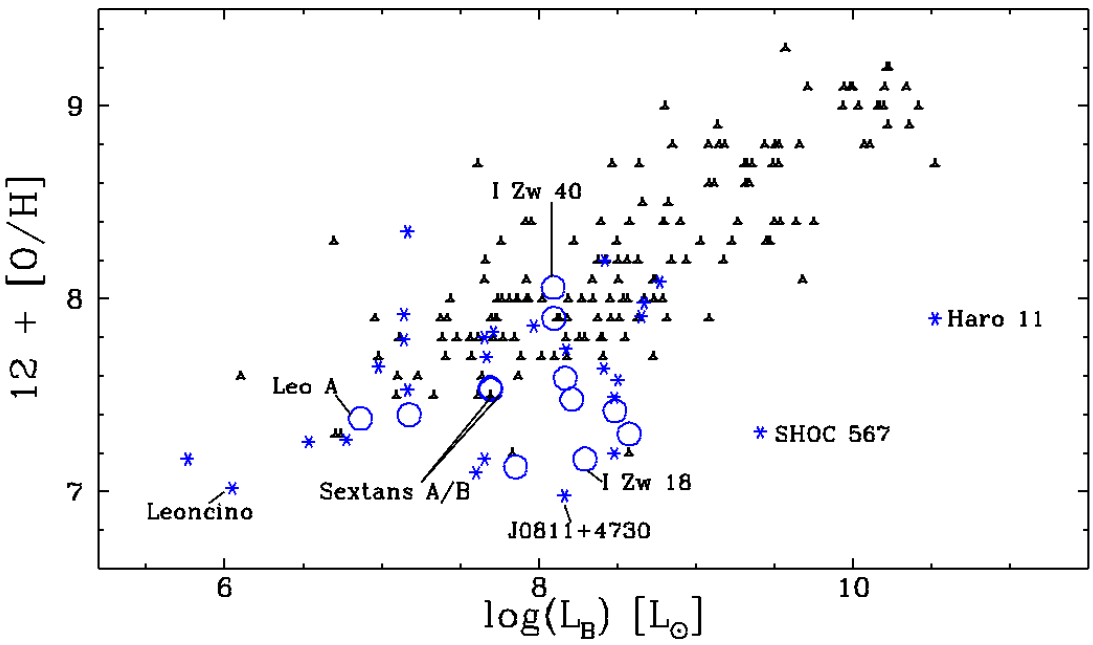

Figure 6: Johnson B L-Z relation for the low-metallicity sample vs. the Local Volume Legacy survey (LVL). Markers are identical to Figures 4 and 5. LVL B magnitudes are from Dale *et al.* (2009); nebular oxygen abundances are from Cook *et al.* (2014b). The large open circles mark the low-metallicity galaxies with archival mid-infrared data, which will constitute my primary sample in later chapters. Low-metallicity galaxies which extreme characteristics have been labeled. While most of the low-metallicity dwarfs populate the phase space expected for low-luminosity galaxies in the local universe, blue compact dwarfs generally lie well to the right of the main L-Z relation for $z = 0$.

incomplete at large distances ($d > 15$Mpc), the sample is complete at $d < 5Mpc$, and the area around the North Galactic Cap has been well surveyed by SDSS.

In Figure 7, I plot the spatial distribution of the full low-metallicity sample vs. the 2MASS Redshift Survey (2MRS; Huchra *et al.*, 2012), which extends to higher distances than the LVL, and includes the Virgo cluster and associated groups. The overdensity of bright galaxies associated with the Virgo supercluster is clearly visible at right ascension $\alpha = 13$h. The bulk of the true XMD dwarfs (12+ (O/H) < 7.6) are located to the west of the main Virgo filament, with the nearest XMDs arranged in a

strikingly linear formation that extends from Sextans northward through Leo, Leo Minor, and Lynx. This feature can be seen more clearly in Figure 8, where I have removed the individual galaxies, but left the major clusters and groups.

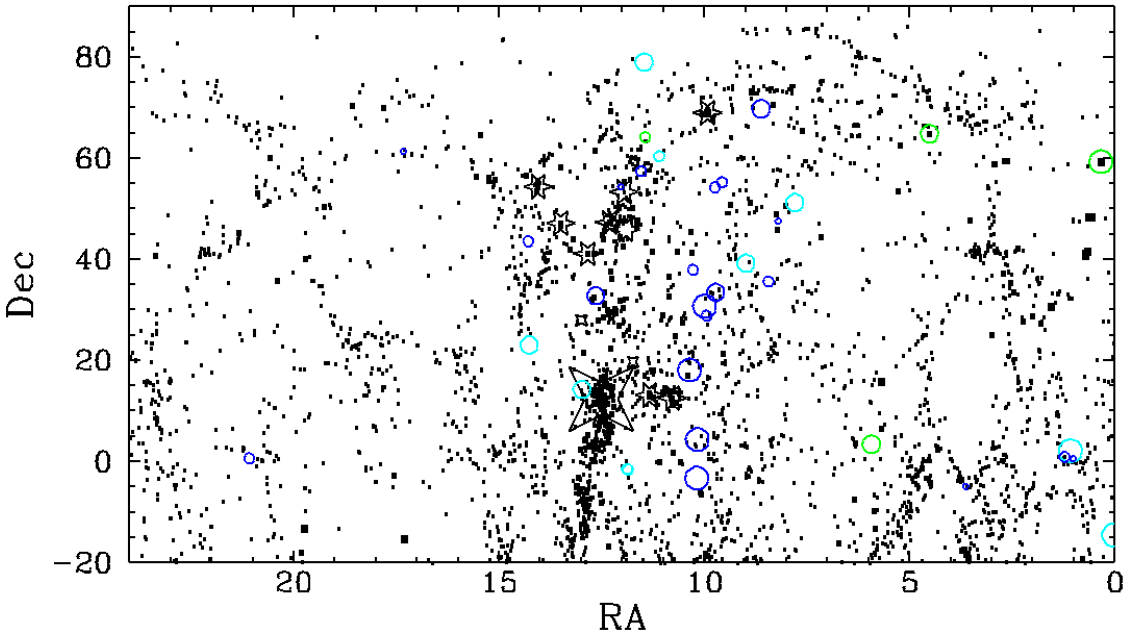

Figure 7: The spatial distribution of low-metallicity galaxies in the local universe ($d < 100$ Mpc), relative to bright galaxies observed by the 2mass survey (black squares). Circles indicate the positions of the low-metallicity galaxies in Table 1, and are color-coded according to metallicity. Green: 12+ (O/H)> 8.1. Cyan: $7.6 <$ 12+ (O/H)< 8.1. Dark blue: 12+(O/H)< 7.6. Smaller marker size indicates large distance, with marker size decreasing at 2, 12, and 30 Mpc.

In general, the low-metallicity dwarfs avoid the main filaments of the Virgo supercluster and its associated groups, which is not unexpected: bright galaxies efficiently suppress dwarf star formation in their halos, and the surrounding IGM will be heavily enriched with their nucleosynthetic products. But the XMDs are also not located in the voids, either. Instead, they appear to favor the outer edges of the large-scale structures. This location, plus the intriguing hint of filamentary structure,

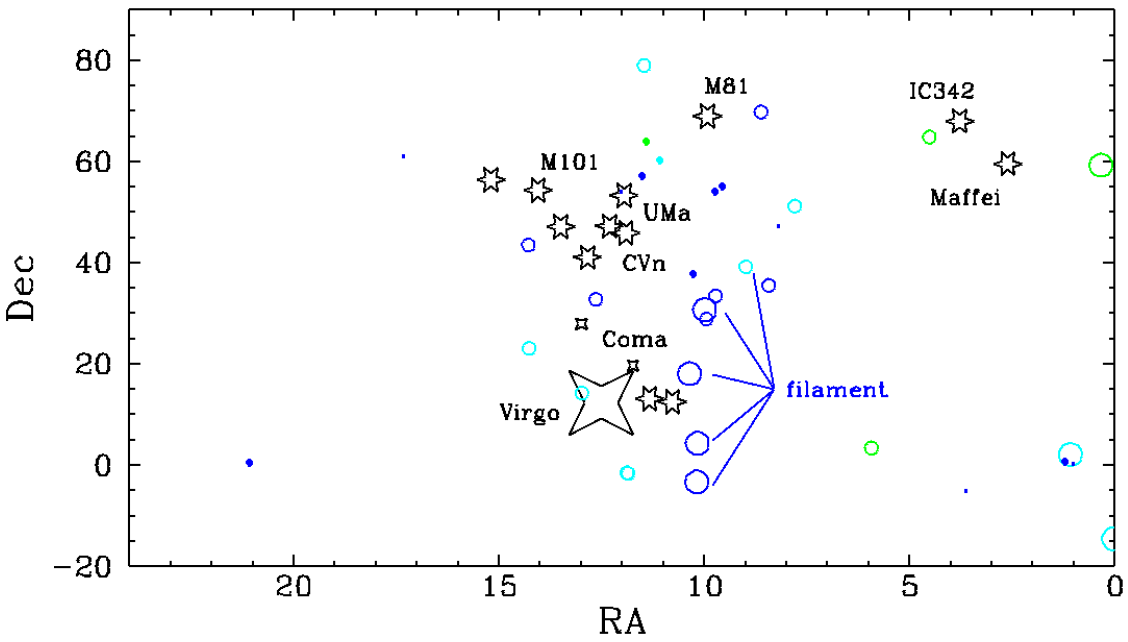

Figure 8: The distribution of nearby ($d < 100$ Mpc) low-metallicity galaxies on the celestial sphere, compared with the major groups (six-pointed stars) and clusters (four-pointed stars) marked for reference. The low metallicity galaxy markers are identical to Figure 7. The larger marker indicates the position of the Virgo cluster, which dominates the structure of the local Universe at $d = 20$ Mpc. The positions of the Coma cluster cores are indicated with the two smaller markers, but Coma's distance is outside the 100 Mpc limit of the sample. Most of the known low-metallicity galaxies are situated in front of and slightly to the west of Virgo and its associated galaxy groups, suggesting the these galaxies trace a filament of relatively-unenriched gas.

gives us a clue to the origin of modern XMD dwarfs. It appears that XMDs are able to maintain their pristine interstellar conditions not just by efficiently expelling metals, but also by drawing their fuel from a shared reservoir of unenriched gas. This would be an exciting result if it held up to additional scrutiny, but for now I will shift my attention to the radio continuum properties of low-metallicity dwarfs, and the measurement of the radio/IR star-formation law in XMD environments.

Chapter 3

JVLA CONTINUUM OBSERVATIONS OF THE SEXTANS A DWARF GALAXY

3.1 Introduction

The cycling of baryonic matter into and out of galaxies is currently a key area of study in extragalactic astronomy. Dwarf galaxies are particularly interesting in this context because their smaller dynamical masses allow outflowing winds and entrained material to escape into and enrich the surrounding intergalactic environment. Additionally, the tendency of the most intense star formation to shift to lower mass galaxies with decreasing redshift (the so-called cosmic "down-sizing"; Cowie *et al.* (1997)) means that dwarf galaxies have become the primary sites of starburst activity in the modern universe. As a result, starbursting dwarf galaxies are the best nearby laboratories for a detailed examination of the self-regulation of star formation via outflows and feedback.

The association of radio continuum emission with vigorous episodes of star formation (and in particular with infrared-luminous star formation, i.e the radio/far-IR relation) is one of the tightest and most reliable correlations in extragalactic astronomy (van der Kruit, 1971; Helou and Bicay, 1993; Yun *et al.*, 2001; Mao *et al.*, 2011). Cosmic rays launched by expanding shocks from supernovae are the presumed sources of the observed synchrotron emission, but a detailed understanding of the underlying physical mechanism linking the two emission measures is still lacking. Furthermore, the very faint end of this relation is not well-constrained: observations of dwarf galaxies are generally observed to have very weak continuum emission, with correspondingly

weak magnetic fields of $< 5\mu G$ (Chyży *et al.*, 2011). A few extreme starbursting dwarfs (NGC1569, NGC4499 and IC 10) are observed to have magnetic fields of order $\sim 10\mu G$. But these objects are on the more massive end of the dwarf galaxy spectrum, and none them have nebular oxygen abundances less than one-tenth Solar. They are therefore not ideal analogs for the extremely low-metallicity, dust-free conditions that are expected in the unenriched primordial environments of the earliest galaxies.

3.1.1 The Sextans A Dwarf

Sextans A (alternatively UGCA205/DDO075) is a nearby low-metallicity, star-bursting dwarf galaxy. It has a recession velocity of 324 ± 2 km/s (Dolphin *et al.*, 2003b) and a Cepheid distance measurement of 1.4 ± 0.4 Mpc (Dolphin *et al.*, 2003a). This places Sextans A at the outer edge of the Local Group, at approximately twice the distance to the Andromeda Galaxy. Sextans A has both very low measured stellar iron abundance ($[Fe/H] = -1.9 \pm 0.2$; Dohm-Palmer *et al.* (1997)) and a low nebular oxygen abundance ($12 + log(O/H) = 7.54 \pm 0.06$; Lee *et al.* (2006), and references therein).

While Sextans A is not especially bright in the far-infrared (S_{60} = 500 mJy, S_{100} = 850 mJy; Mateo (1998)), several bright knots of star formation are observed in optical images. Deep Hα imaging has revealed a number of bright HII regions, large shells of ionized gas, and several Hα streamers over a kiloparsec in length (Hunter and Plummer, 1996; Hunter and Gallagher, 1997; Dale *et al.*, 2009). These data suggest that despite its small size and low overall luminosity Sextans A is currently undergoing an episode of intense star formation, which is in turn powering a large-scale outflow of material. The comparative lack of far-infrared emission may be due in part to the

low metallicity inhibiting the formation of the dust grains that produce the far-IR spectral energy hump of most bright star-forming galaxies.

Atomic hydrogen 21-cm emission has been observed from Sextans A (Skillman *et al.*, 1988; Namumba *et al.*, 2018); however no 20-cm radio continuum was detected by the NRAO VLA Sky Survey (NVSS) (Condon *et al.*, 1998). The Sextans A dwarf has also been observed at 2.64 GHz and 4.75 GHz with the 100-m Effelsburg telescope (Chyży *et al.*, 2011; Klein, 1986), but these observations only provided upper limits. The first reported radio continuum detection is from Hindson *et al.* (2018), who observed the galaxy with the JVLA in *C*-configuration, as part of the LITTLE THINGS survey; they report an upper limit when integrated over the disk of the galaxy, but after BANE masking produce a detection.

3.2 Observations

L-band ($f = 1 - 2$ GHz; $\lambda \sim 20$cm) continuum observations of the Sextans A dwarf galaxy were obtained with the upgraded Jansky Very Large Array (JVLA) radio interferometer located near Magdalena, New Mexico on April 7 and 8, 2013. The program ID for this set observations is 13A-467. The JVLA antennas were positioned in the **D** configuration. This is the most compact configuration of the EVLA, with a maximum baseline of 1 km and a maximum synthesized resolution on the sky of $\theta_{HPBW} = 44$ arcseconds at 1.4 GHz. The size of the primary beam is set by the diffraction limit of the individual JVLA antennas, and is approximately $\theta_{PB} = 30$ arcminutes at these frequencies.

The total on-source integration time for these observations was 7 hours, split between the two observing periods on April 7 and April 8. This includes 5.1 hours

on the Sextans A science field, plus 13.3 minutes each on the flux and polarization calibrators, plus 3C286 (J1330+3030), Mrk 068 (J1407+2827), plus 45 minutes total on the phase calibrator J0943-0819. [Split into days rather than total?] The phase calibrator was observed for 50 seconds, at 4 minute intervals during observations of the primary science field. The upgraded JVLA includes the Wideband Interferometric Digital Architecture (WIDAR) correlator, which allows continuous observation from 1-2 GHz in L-band, broken into eight 128 MHz spectral windows (see Table 1).

3.3 Data Acquisition and Reduction

All data processing steps—including flagging, calibration, and imaging—were performed using *CASA v4.7.0*.

3.3.1 Initial Flagging

Before beginning the calibration, some initial large-scale flagging was done on the entire set (science scans and calibrator scans). The EVLA Continuum Tutorial[6] recommends excising the first 10 seconds of each scan. However, given the shorter one minute scans for this dataset, this would result in fully 1/6 of the data being thrown out. Visual inspection of the scans showed that only the first second or two of data showed different amplitudes, so we opted to excise a shorter interval of 2 seconds.

The EVLA operator log reports that the L-band receivers were not installed on antennas 6, 10, 17, 20 during this observations, so all baselines associated with

[6]http://casaguides.nrao.edu/index.php?title=EVLA_Continuum _Tutorial_3C391

Table 3: Summary of JVLA continuum observations of Sextans A

Program ID	Obs Date[a] [UTC]	Time[a] [UTC]	θ_{HPBW}[b,c,e,f] [arcsec]	θ_{LAS}[b,d,e,f] [arcmin]	T_{int}[g] [min]
L-band observations					
13A-467	07-Mar-2013	02:38	46	16.2	151.5
”	08-Mar-2013	02:04	”	”	151.5
				Total time:	303.0
S-band observations					
15B-307	15-Nov-2015	16:17	29.9	4.1	15.2
”	16-Nov-2015	15:26	”	”	15.2
”	29-Dec-2015	13:21	”	”	15.3
				Total time:	45.7
C-band observations					
15B-307	17-Dec-2015	08:05	15.6	2.0	15.8
”	22-Dec-2015	09:01	”	”	59.3
”	23-Dec-2015	07:59	”	”	59.3
				Total time:	134.4

[a] UTC date and start time of the observations
[b] All data were taken in **D**-configuration, with a maximum baseline distance between JVLA antenna of $B_{max} = 1.03$ km, and a minimum baseline separation $B_{min} = 0.035$ km.
[c] θ_{HPBW} is the resolution of the synthesized beam (half-power beam width, FWHM).
[d] θ_{las} is the largest angular scale structure which can be imaged by the synthesized array.
[e] For “snapshot” S- and C-band images, with incomplete U-V plane sampling, θ_{HPBW} is a factor of 1.3 larger, and θ_{las} is a factor of 2 smaller.
[f] From https://science.nrao.edu/facilities/vla/docs/manuals/oss/performance/resolution, the VLA Observational Status Summary.
[g] T_{int} is the total integration time on the Sextans A science field.

these antennas are flagged. The operator log also notes that the C-band receiver on antenna 13 was removed for repairs. No comment is made about the status of the L-band receiver on this antenna, but examining the data we find that the amplitudes associated with antenna 13 appear to be an order of magnitude less than the other baselines. We therefore flagged all baselines associated with this antenna as bad data.

3.3.2 RFI Flagging and Hanning Smoothing

The WIDAR correlator permits near-continuous spectral coverage between 1GHz and 2 GHz, distributed across 8 spectral windows with 128 MHz coverage each. Unfortunately, while the frequency ranges from 1400-1427 MHz and from 1660-1670 MHz have been reserved for astronomical observations, much of the L-band is available for telecommunications and microwave broadcasting. Sources of L-band radio frequency interference (RFI) have been characterized at the JVLA site [7], and include contributions from FAA and military radar installations, high altitude balloons, GPS and IRIDIUM satellites. The compact **D** configuration compounds the problem, because all the antennas will tend to see the same RFI sources. In order to properly calibrate and process the comparatively faint signals of extragalactic sources, channels affected by RFI must be flagged and removed from the measurement set.

Strong line sources will cause ringing across the entire spectral window due to the Gibbs phenomenon, rendering nominally unaffected frequency channels unusable. Prior to RFI flagging, we smooth with a Hanning window function to mitigate Gibbs ringing. This results in a factor of 2 loss in spectral resolution, but improvements in the background levels of the clean channels are immediately obvious.

3.3.2.1 L-band RFI Characteristics

The RFI characteristics of the observed L-band spectral windows are summarized in Table 4. Of the 8 spectral windows observed, 6 are heavily impacted by RFI.

[7] Guide to Observing with the VLA: Radio Frequency interference: https://science.nrao.edu/facilities/vla/docs/manuals/obsguide/rfi

Flagging by amplitude leaves very little data in these spectral windows, and even that is extremely noisy; we consider these windows to be effectively useless. The cleanest data are seen in spectral windows at 1.42 and 1.80 GHz. Most of the RFI in these spectral windows appears in the form of discrete, semi-regular noise spikes impacting most of the channels and baselines, but lasting < 1 second.

The bulk of the flagging is done at this stage, on the un-calibrated data, primarily by examining the visibility amplitudes as a function of time or average U-V distance. Since some of the affected data will be hidden by the widely varying phases of the uncalibrated data, we do a second stage of flagging after calibration.

In Figure 10, I display channel vs. time "waterfall" plots for all of the spectral windows listed in Table 4. Of the 9 primary 128 MHz spectral windows, all but three are saturated with RFI to the point of being unusable. Two of the remaining windows, spw0 and spw16, are only slightly offset from one another in frequency, so they are essentially identical. This means I only have two "clear" spectral windows to work with for my science observations: spw0 (1.42 GHz) and spw6 (1.8 Ghz).

Spectral Window	Channels	Frequency Range [GHz]	Channel Width [kHz]	Total Bandwidth [kHz]	Notes
128 MHz standard spectral windows					
9	256	1.000 - 1.127	500	128000	not usable
11	256	1.127 - 1.255	500	128000	not usable
14	512	1.256 - 1.384	500	128000	not usable
0	256	1.356 - 1.484	500	128000	usable
16	256	1.384 - 1.511	500	128000	usable
2	256	1.484 - 1.612	500	128000	not usable
3	256	1.612 - 1.740	500	128000	not usable
6	256	1.740 - 1.868	500	128000	usable
7	256	1.868 - 1.995	500	128000	not usable
RFI-avoidant custom sub-windows					
10	256	1.008 - 1.072	250	64000	not usable
12	128	1.139 - 1.171	250	32000	not usable
13	128	1.184 - 1.216	250	32000	not usable
15	128	1.269 - 1.301	250	32000	not usable
1	512	1.418253 - 1.419251	1.95	1000	HI line
4	128	1.622 - 1.686	500	64000	not usable
5	128	1.638 - 1.670	250	32000	usable, narrow[1]
8	128	1.884 - 1.916	250	32000	usable, narrow

Table 4: L-band spectral windows and RFI characteristics

Figure 9: L-band waterfall plots for all WIDAR spectral windows

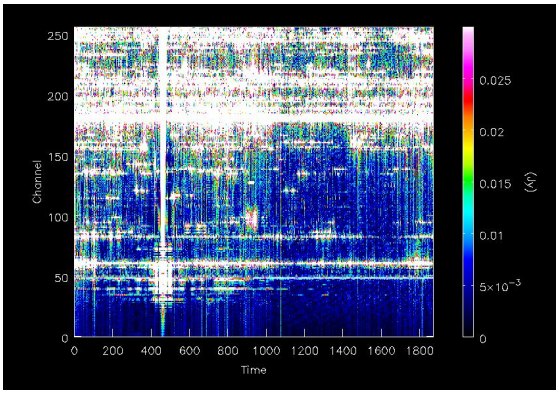

(a) Spw 9: 1.000 $\sim$ 1.128 GHz

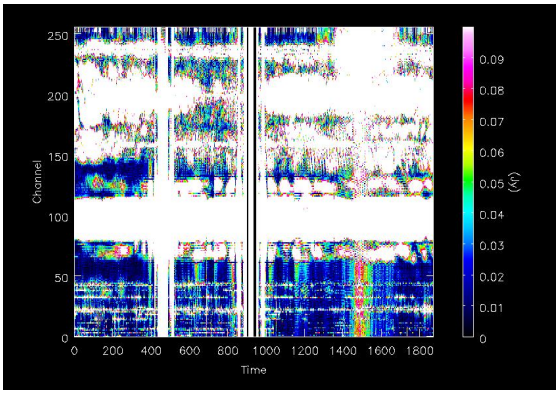

(b) Spw 11: 1.127 $\sim$ 1.255 GHz

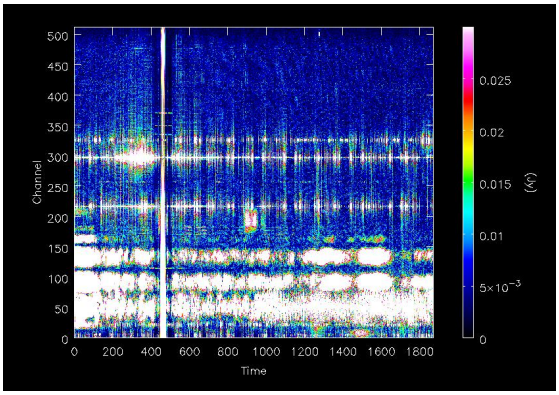

(c) Spw 14: 1.256 $\sim$ 1.384 GHz

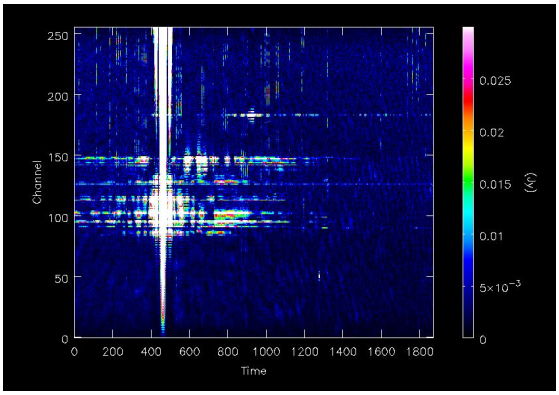

(d) Spw 0: 1.356 $\sim$ 1.484 GHz

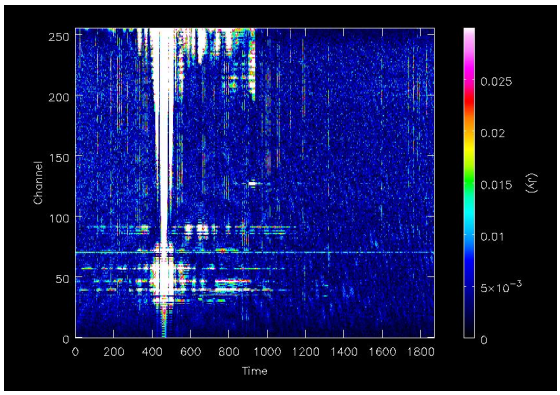

(e) Spw 16: 1.384 $\sim$ 1.511 GHz

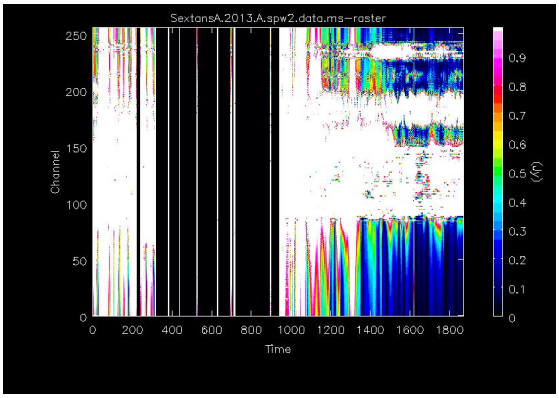

(f) Spw 2: 1.484 $\sim$ 1.612 GHz

Figure 9: (Cont'd.) L-band waterfall plots for all WIDAR spectral windows

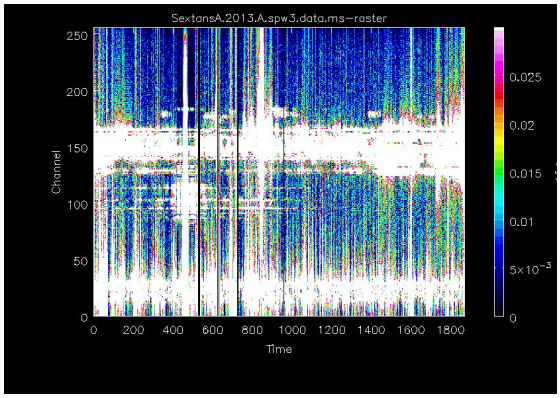

(g) Spw 3: 1.612 $\sim$ 1.740 GHz

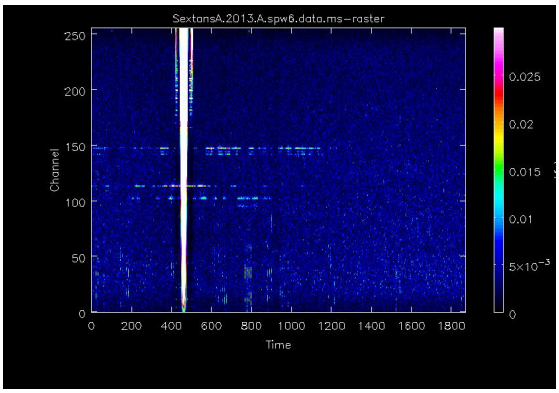

(h) Spw 6: 1.740 $\sim$ 1.868 GHz

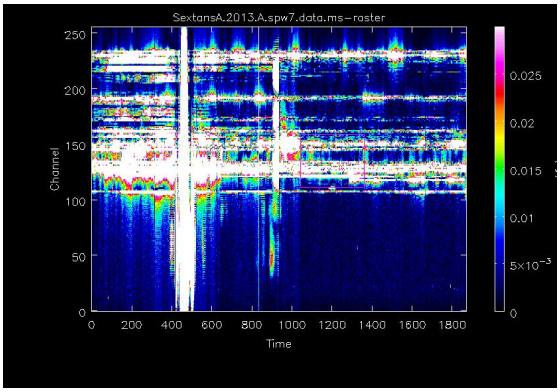

(i) Spw 7: 1.868 $\sim$ 1.995 GHz

Figure 9: (Cont'd.) L-band waterfall plots for all WIDAR spectral windows

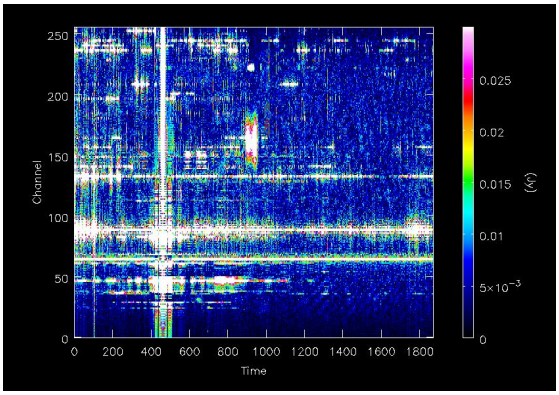

(j) Spw 10: 1.008 ∼ 1.072 GHz

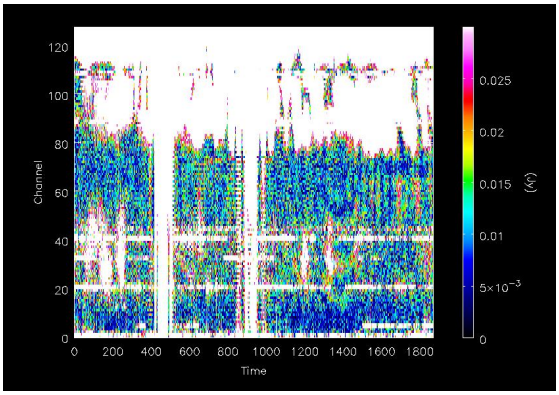

(k) Spw 12: 1.139 ∼ 1.171 GHz

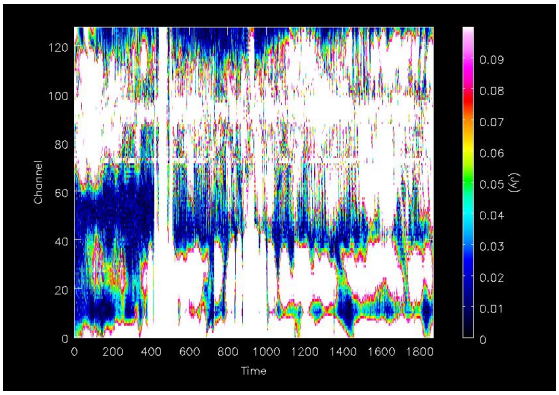

(l) Spw 13: 1184 ∼ 1216 GHz

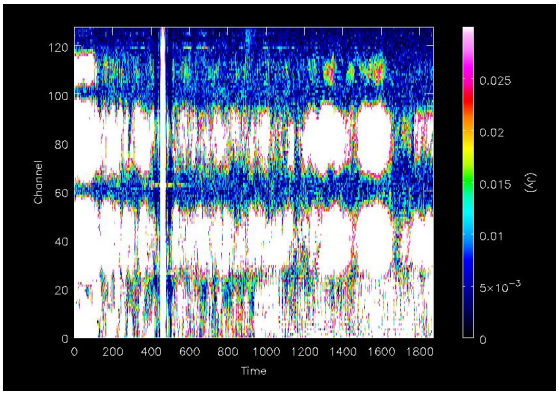

(m) Spw 15: 1269 ∼ 1301 GHz

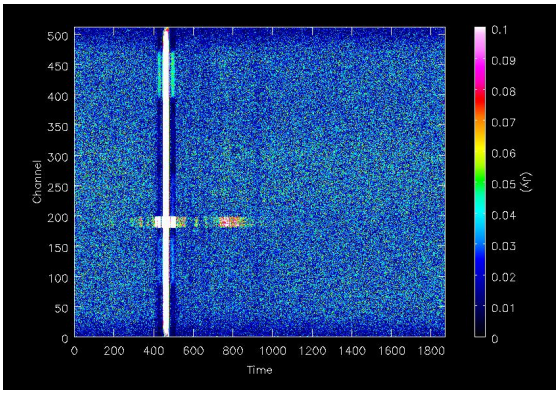

(n) Spw 1: 1.418253 ∼ 1.419251 GHz (HI)

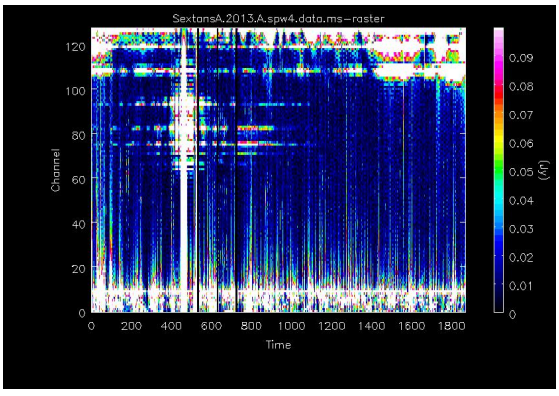

(o) Spw 4: 1.622 ∼ 1.686 GHz

Figure 9: (Cont'd.) L-band waterfall plots for all WIDAR spectral windows

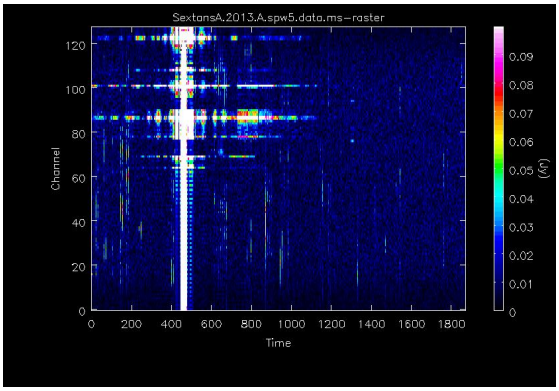

(p) Spw 5: $1.638 \sim 1.670$ GHz

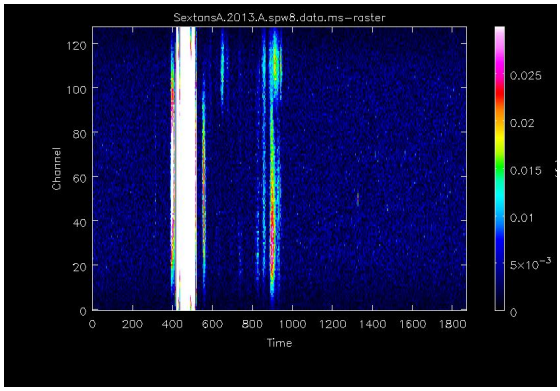

(q) Spw 8: $1.884 - 1.916$ GHz

Figure 10: Waterfall plots of all L-band spectral windows for the Sextans A science field. The spectral windows frequency ranges are given in Table 4.

3.3.2.2 S- and C-band RFI Characteristics

Because we expected less RFI at higher frequency, the standard S- and C-band correlator set-ups were employed for these data, with uniformly-spaced 128 MHz spectral windows. This spacing gives full coverage of the 2-4 GHz S-band, with minimal overlap (see Table 5. The WIDAR correlator cannot fully cover the 4-8 GHz C-band, so the sidebands were chosen to correspond to the expected RFI-free windows at 5 and 7 MHz.

The shorter observation times at these meant that it was more likely for the entire science observations to miss the bright geosynchronous satellites entirely, but also that there was some possibility of an entire observation being effectively ruined. In principle it should be possible to predict when the Sextans A science field will be coincident, and schedule the observations to avoid these times, the 15B observations were observed as filler time during the rest of the JVLA queue observing. This meant

that the JVLA queue observing system scheduled these dataset in between other higher rated long programs.

As it happens, the S- and C-band datasets appear to have missed the geosychronous window, and none of them are obviously impacted by the bright, multi-frequency source which is apparent in the L-band science data. The data were all examined and manually edited, and some temporally-varying sources were removed. But overall the

As expected, the higher frequency S- and C-band datasets were less impacted by RFI , though the geosynchronous signatures are still visible. For S-band, 616 spectral windows were deemed clear enough to calibrate and image; for C-band, 1016 spectral windows were used.

3.3.3 Calibration

Calibration is done on each spectral window separately. We perform the standard corrections to the observed visibilities: flux, bandpass, complex gain, and polarization.

The flux calibrator observed during the Sextans A observations is 3C286, a bright (14 Jy at 1.4 GHz) and stable radio source at redshift $z = 0.8$. 3C286 is polarized and marginally resolved, even in **D** configuration, so we use the L-band Stokes source model provided by the VLA Calibrator Resources[7]. We use 3C286 to set the flux scale, derive an initial phase solution, and measure the spectral responses of each antenna. We experimented with polynomial interpolations to model the frequency responses, but found that channel-to-channel interpolation did a better job fitting the edge of the bandpass.

Spectral Window	Channels	Frequency Range [GHz]	Channel Width [MHz]	Usable Bandwith [MHz]	Notes
8	64	1.998 - 2.114	2000	128000	not usable
9	64	2.116 - 2.242	2000	128000	not usable
10	64	2.444 - 2.370	2000	128000	not usable
11	64	2.372 - 2.498	2000	128000	not usable
12	64	2.500 - 2.626	2000	128000	usable
13	64	2.628 - 2.754	2000	128000	not usuable
14	64	2.756 - 2.882	2000	128000	usable
15	64	2.884 - 3.010	2000	128000	usable
0	64	2.988 - 3.114	2000	128000	usable
1	64	3.116 - 3.242	2000	128000	usable
2	64	3.244 - 3.370	2000	128000	usable
3	64	3.372 - 3.498	2000	128000	not usable
4	64	3.500 - 3.626	2000	128000	not usable
5	64	3.628 - 3.754	2000	128000	not usable
6	64	3.756 - 3.882	2000	128000	not usable
7	64	3.884 - 4.010	2000	128000	not usable

Table 5: S-band spectral windows and RFI characteristics

Once we have applied the bandpass correction, we are able to solve for the full complex gain solutions (amplitude g_i and phase ϕ_i) for all channels for all three observed calibrators: 3C286, Mrk 668, and J0943-0819. Because the observed flux, polarization and phase calibrators are widely separated on the sky, there are likely to be considerable phase offsets. We therefore derive the gain solutions for all three calibrators separately.

The polarization calibration involves two steps: 1. solving for the leakage terms and 2. solving for the polarization angle. The so-called "leakage" terms quantify the degree of instrumental polarization introduced by the system on an unpolarized

[7]http://www.aoc.nrao.edu/ $\sim$ smyers/calibration/

Spectral Window	Channels	Frequency Range [GHz]	Channel Width [MHz]	Total Bandwith [MHz]	Notes
8	64	4.228 - 4.414	2000	128000	not usable
9	64	4.416 - 4.542	2000	128000	not usable
10	64	4.544 - 4.670	2000	128000	not usable
11	64	4.672 - 4.798	2000	128000	not usable
12	64	4.800 - 4.926	2000	128000	usable
13	64	4.928 - 5.054	2000	128000	usable
14	64	5.056 - 5.182	2000	128000	usable
15	64	5.184 - 5.310	2000	128000	usable
0	64	6.188 - 6.314	2000	128000	not usable
1	64	6.316 - 6.442	2000	128000	not usable
2	64	6.444 - 6.570	2000	128000	usable
3	64	6.572 - 6.698	2000	128000	usable
4	64	6.700 - 6.826	2000	128000	usable
5	64	6.828 - 6.954	2000	128000	usable
6	64	6.956 - 7.082	2000	128000	usable
7	64	7.084 - 7.210	2000	128000	usable

Table 6: C-band spectral windows and RFI characteristics

source. For this correction we use the unpolarized source Mrk 668. To solve for the polarization angle we require a bright, highly-polarized source, so we return to 3c286, which is known to have a polarization fraction of 11% with a position angle of 66° on the sky.

We apply the flux scaling determined from 3c286 to the polarization and phase calibrator, and then apply the the appropriate calibration solutions—bandpass, complex gain, and polarization—to each calibrator field. The phase calibrator J0943-0819 has been chosen To calibrate the science field, I apply the gain solution from the phase calibrator J0943-0819, which has been chosen to be as close as possible on the sky to the Sextans A observations. Even so, there will be slight phase offsets between the

two fields, which I will not be able to correct for until the self-calibration phase of the reductions.

After calibrating, we make one last examination of the visibility amplitudes as a function of baseline and phase, and flag any newly-apparently RFI signals. We then split the Sextans A science observations at 1.42 GHz and 1.80 GHz into two separate datasets, and proceed with imaging.

3.3.4 Imaging, Deconvolution, and Self-Calibration

We image of the calibrated visibilities and perform the subsequent deconvolution of the EVLA beam pattern using the *CASA* implementation of the CLEAN algorithm (Högbom, 1974). At a wavelength of 20 cm, the *D*-configuration of the VLA has an interferometric resolution of 44 arcseconds; to insure adequate sampling of the beam pattern, we use an image pixel size of 6 arcseconds A total image size of 1024 by 1024 pixels insures that the primary beam and first sidelobes are imaged in their entirety. In order to match the imaging with all three spectral bands, duplicate the image size for the S-band and C-band data, with scaled-down pixels to match the improving resolution with increasing frequency.

In all spectral bands, the initial image produced by CLEAN is dominated by a bright unresolved source at (RA,Dec)= (10:10:31,-04:40:10). These coordinates correspond to a known 300 mJy source in the NVSS catalog. This object is in a problematic location for the S- and C-band observations: at these frequencies, it is located very close to the null at the outer edge of the JVLA primary beam, and moves in and out of the primary beam over the full frequency range of these spectral

bands. This source is very difficult to properly characterize and deconvolve during the CLEANing process, and leaves numerous bright fringes in the resulting

After masking and CLEANing this source, two additional point sources become apparent, at (RA,Dec) = (10:10:29;-04:37:51) and (10:10:51;-04:28:42), corresponding to a pair of NVSS sources with fluxes of 45 mJy and 100 mJy, respectively. After 4 CLEAN cycles and (a total of $\sim$ 2000 iterations at 8% gain), $7 > 20$ mJy point sources are detected and removed from both spectral bands during the initial CLEANing, leaving a background 5 mJy beam-to-beam rms noise remains.

These points sources are provided as the model for the initial round of self-calibration. As per the recommendations of the EVLA "advanced topics" tutorial[8], during the first round of self-calibration, we solve for phase only, with a long solution interval relative to the data sampling time (*solint* = 30s, vs. a sampling time of 1s).

After self-calibration, another round of CLEANing produces $\sim$ 10 additional point sources in both spectral windows, and leaves a residual background rms noise of 2 mJy. While none of these new point sources are listed in the NVSS, they all of have clear sidelobe patterns (prior to CLEANing), and are located at identical coordinates (though with slightly different flux ratios) in both the 1.35 GHz and 1.85 GHz images. We therefore included these sources in our update flux model for the Sextans A field, and performed another round of self-calibration with a slightly shorter solution interval (*solint* = 20s).

It should be possible to improve the phase calibration of the images via self-calibration, particularly given the bright background quasar in the field. However, this quasar's location near the edge of the primary beam compromises its reliability as a phase calibrator. For C-band, we did achieve improvements in the background rms and

[8]http://casaguides.nrao.edu/index.php?title=EVLA_Advanced _Topics_3C391

fringing via self-calibration. Self-calibration was much less successful in the S-band: after a single round of self-calibration, the image quality had deteriorated considerably, with bright fringes dominating most of the image. We therefore abandoned attempts at self-calibration, and stuck with our original gain calibration. Bright fringes from the nearby quasar are apparent in both the CLEANed S-band and C-band images.

We have the most success using self-calibration with the the L-band images, where the quasar is solidly inside the primary beam. In total, 4 rounds of CLEANing and self-calibration were performed separately on both spectral windows of the L-band data, with each showing successive improvements in the image quality. Starting with the third iteration of self-calibration, we shifted to simultaneous phase and amplitude solutions, and progressively shortened the solution intervals. Our stopping condition for each frequency was subsequent iterations of self-calibration failing to improve the rms noise characteristics of the CLEANed image. A total of ~ 50 point sources with flux $> 10mJy$ were CLEANed and added to the self-calibration flux model. All of the point sources CLEANed from the 1.42 GHz had clear counterparts in the 1.80 GHz image, and vice versa, a characteristic we would not expect from noise fringes at two different frequencies.

3.4 Results and Analysis

The CLEANed and self-calibrated images of Sextans A are show in Figures 11- 12b, overplotted with optical RGB color data f and narrow-band Hα imaging from the Local Volume Legacy Survey (LVL) (Dale *et al.*, 2009; Cook *et al.*, 2014b). While bright

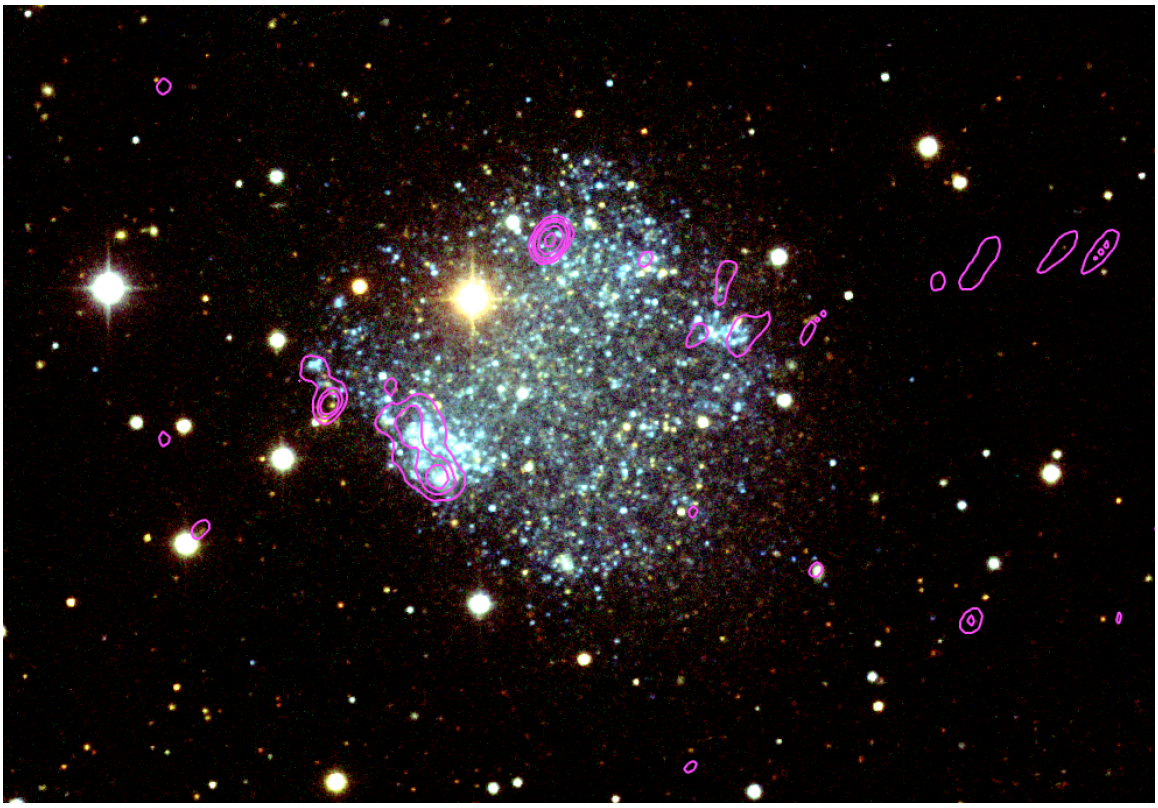

Figure 11: Sextans A C-band flux density contours are overplotted on RGB optical imagery from Cook *et al.* (2014b). Contours are at 30, 60, 90, 180, and 360, 540μJy/beam. RGB color assignments are red = R, green = V, blue = B. The optical image was acquired from the NASA Extragalactic Database (NED). the radio continuum flux is entirely associated with the bright star forming knot at the southern end of the galaxy.

fringes from the background quasar create considerable confusion, diffuse continuum emission associated with the brightest star forming regions is clearly apparent in all three spectral bands.

3.4.1 C- and S-band Continuum Emission from Sextans A

The C-band (4-8 GHz) radio continuum image is both the highest resolution and the highest sensitivity, with rms = 11.6μJy/beam. The S-band (2-4 GHz) image has

Figure 12: S- and C-band radio continuum vs. Hα emission of Sextans A

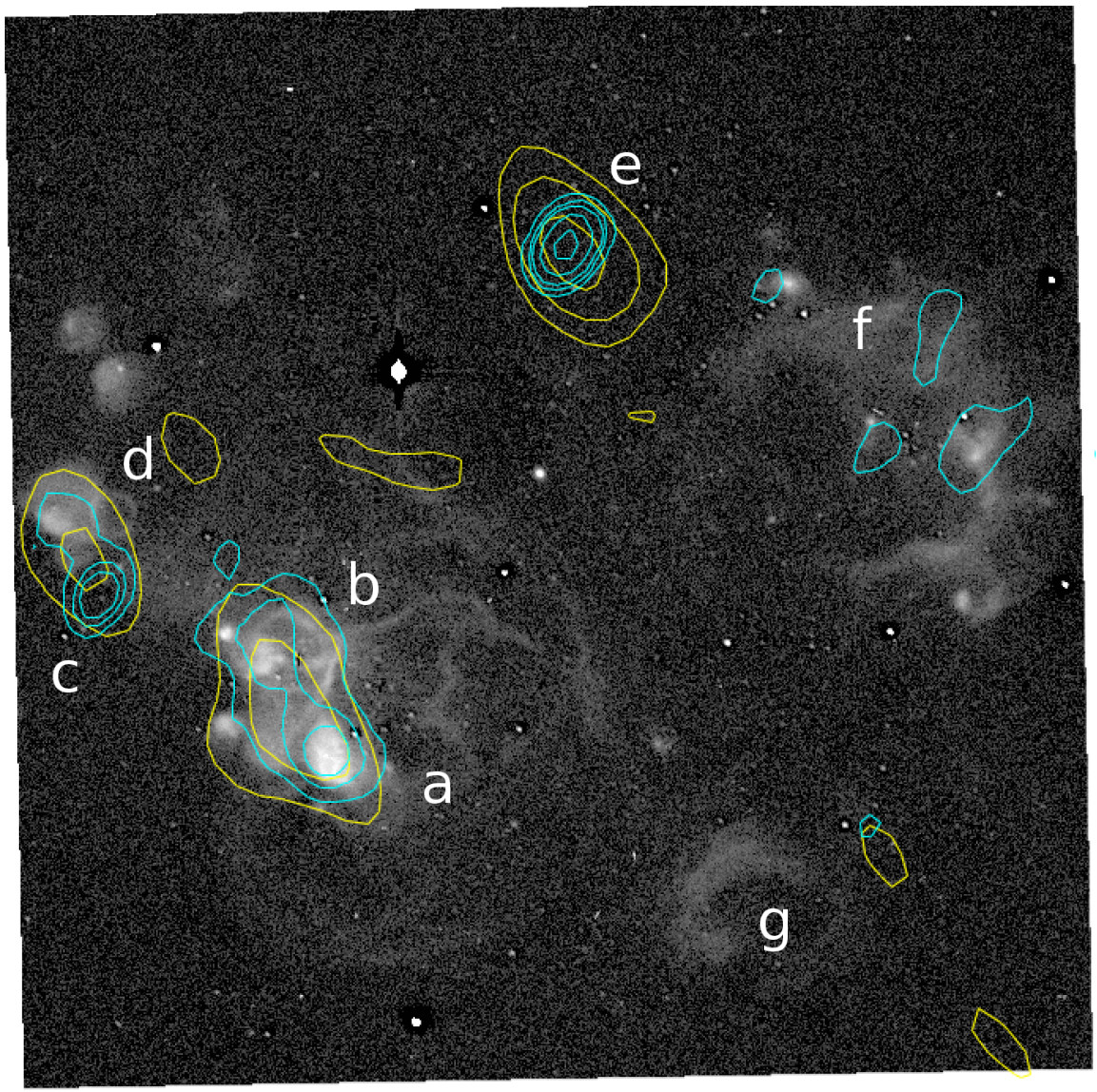

(a) S-band (yellow) and C-band (cyan) flux density contours overlaid on narrow-band optical Hα image of Sextans A. S-band contours are at 0.125, 0.25, 0.5, 0.75, and 1.5, 3.0 μJy/beam. C-band contours are identical to Figure 11. Underlying Hα image is from Dale *et al.* (2009), acquired via NED.

rms $\sim$ 75.0μJy in the areas of the image that are not affected by fringing from the bright quasar to the west of Sextans A; this increases to rms $\sim$ 120μJy when the fringed areas are included. Interferometric fringes from the bright quasar create is

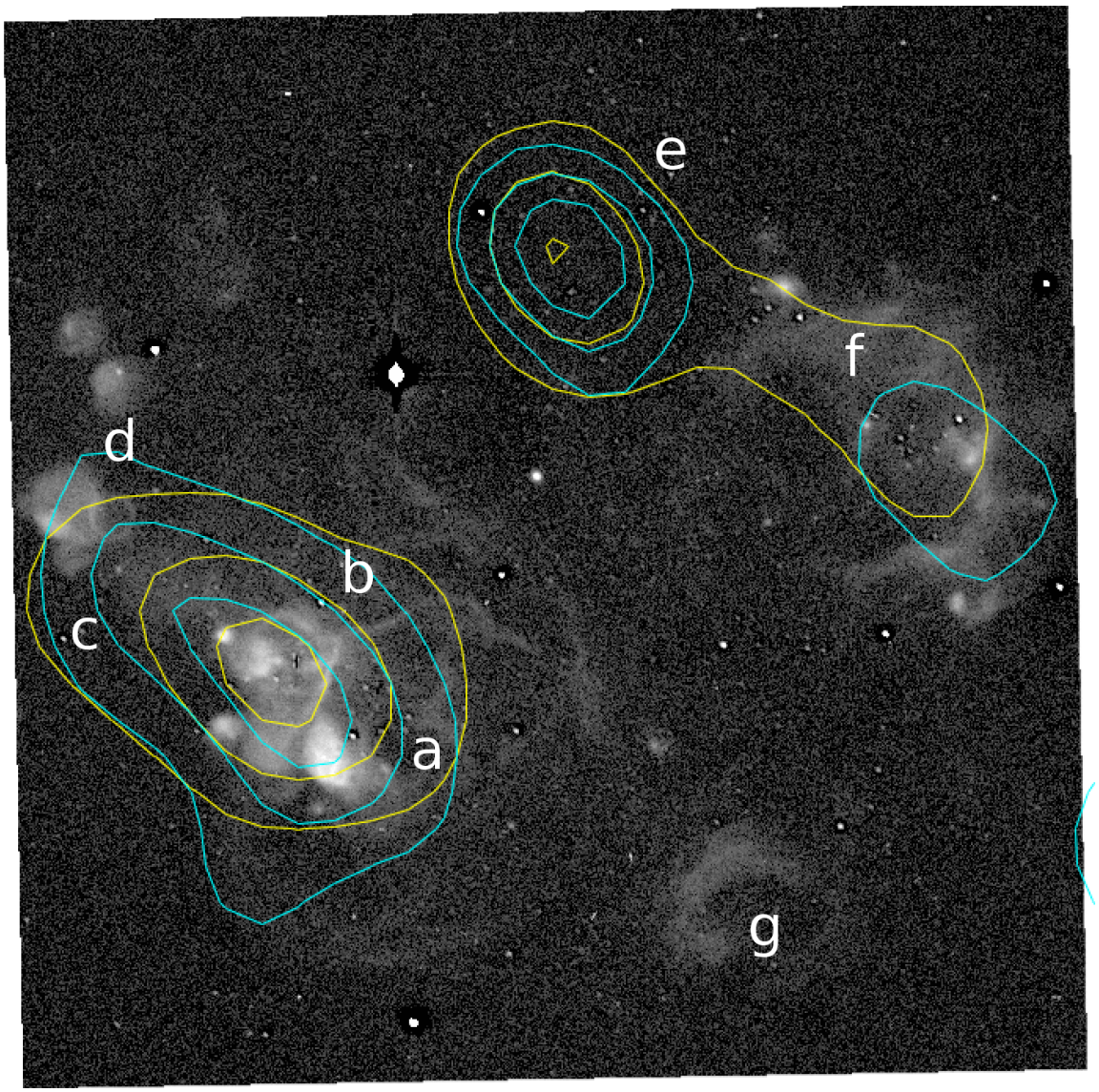

(b) L-band band flux density contours. Yellow contours are 1.42 GHz, with contours at 0.3, 0.6, 0.9, 1.8, 3.6 and 5.4 mJy/beam. Cyan contours are 1.8 GHz, with contours at 0.2, 0.4, 0.6, 1.2, 2.4 and 3.6 mJy/beam. Underlying Hα image is identical to Figure 12a.

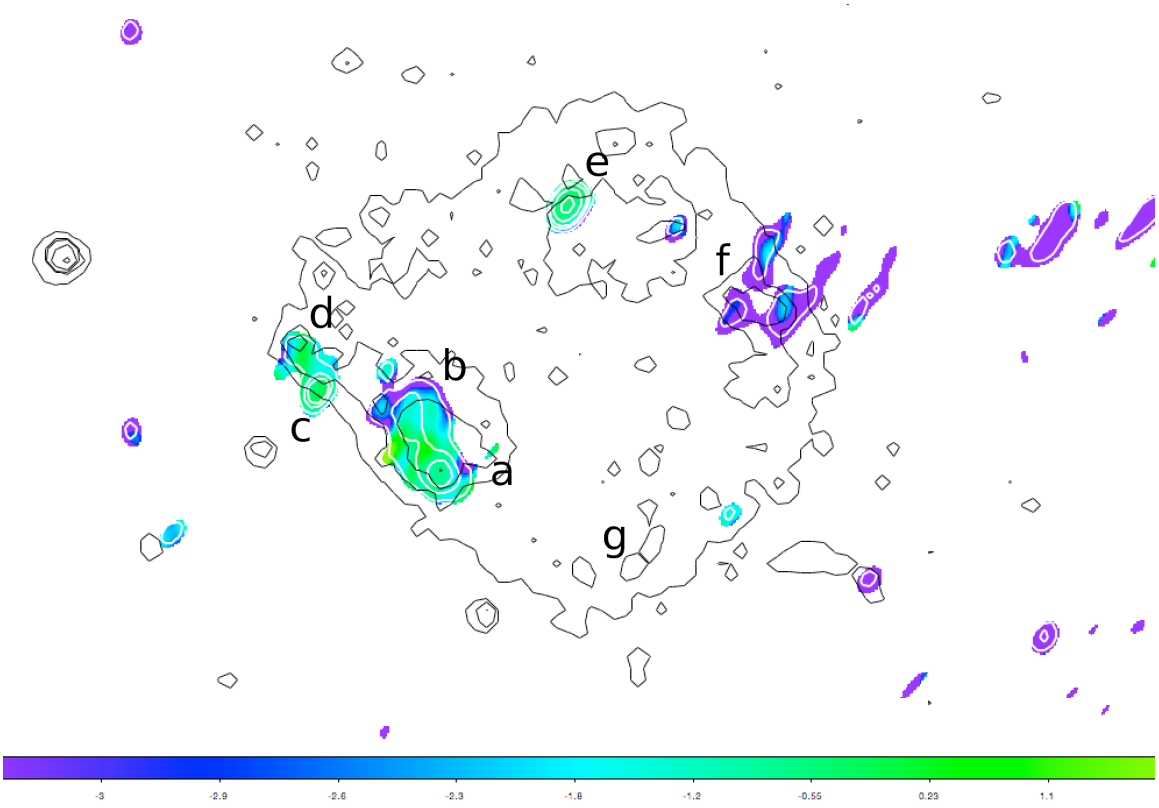

Figure 13: Map of C-band continuum power law slope α of Sextans A, as output by the CLEAN algorithm. Black contours are the optical B band image from Figure 11. White contours are identical to the C-band flux density contours in that image.

particularly bad in the S-band image. Nevertheless, radio continuum associated with the active star forming sites in Sextans A is readily apparent in all spectral bands

In the higher-resolution C-band images, the radio continuum is resolved into discrete areas of diffuse and compact emission associated with various Hα regions and optical point sources. These regions are individually labeled in Figure 12a, and their C-band properties are tabulated in Table 7. . The bright star forming regions on the east side of Sextans A (regions "a" and "b") are clearly detected in both images. Region "d" is somewhat complex, with faint continuum emission associated with the easternmost Hα knot, and none associated with the knots to the north west. There

is also spherical "Bubble"-type nebular apparent in the Hα image–this also has no obvious associated radio continuum.

The unresolved source "c"–which is only individually resolved in the C-band image–has a somewhat flatter spectral slope than the star-forming regions, and may be a background source. There is a bright optical source in quite close to the center of "c", but there are no known extragalactic sources at this position. Likewise, the unresolved source "e" has a flat spectrum indicative of a background quasar, but is not near the position of any known extragalactic sources. There is no optical counterpart to "e", but it is detected in all spectral bands, (including L-band).

The diffuse radio emission around the western Hα region "f" appears to be a marginal detection at best, but actually amounts to potentially significant flux when the entire region is summed. The large, faint Hα bubble at position "g" in the southern corner of the galaxy has no apparent radio continuum emission.

The spectral index maps output by CLEAN are plotted in Figure 13. These should be used with caution, as they are prone to systematic errors associated with changing primary flux and beam resolution over the wideband spectral range. However, most of the regions of interest are located around the center of the primary beam, and the estimate spectral index should be fairly robust for the brighter detections. We can test this robustness further by using the spectral indices derived from the comparison of L-, S-, and C-bands.

3.4.2 L-band Continuum Emission from Sextans A

Because we only have two valid 100 MHz spectral windows, at 1.42 and 1.85 GHz, we imaged these separately. These are displayed with the Hα emission in Figure 12b.

There are two emission peaks in Sextans A in the L-band images: an extended 2.0 ± 0.15 mJy source on the eastern side of the galaxy, associated with regions "a"-"d", and an unresolved source at the northern edge, at the same location as the presumed background source "e" in the higher frequency images. Once again, there is apparent flux associated with region "f", but the position is uncertain (due to fringing from the bright quasar to the west), and the detection is marginal at best.

The spectral index α is defined as follows:

$$\frac{S_1}{S_2} = \left[\frac{\nu_1}{\nu_2}\right]^{\alpha} \tag{3.1}$$

With detections in S-band and L-band, we can attempt to confirm the spectral slopes output by the C-band CLEAN alpha image. The spectral slopes range from $\alpha = -0.1$ to -2.0, with a flux-weighted average of $\alpha = -1.45$. This spectral index is steep compared to other dwarf galaxies in the literature: IC 10 has a measured spectral index of $\alpha = -0.35$, NGC 4449 has $\alpha_{=} - 0.41$ (Chyży *et al.*, 2003; Klein *et al.*, 1996), and NGC 3079 has $\alpha = -1.02$.

Because α is related to underlying electrons by $\alpha = (\delta - 1)/2$, where δ is the power-law index of the electron energy distribution, a steep synchrotron spectral index likewise implies a steep underlying energy distribution of electrons. The easiest way to create such an energy distribution is by losing the highest energy electrons to the intergalactic medium –not an entirely unfeasible scenario, given the low mass and shallow gravitational well of Sextans A, coupled with the large-scale Hα outflows.

Region[a]	RA [h:m:s]	Dec [d:m:s]	Flux density[b] [μJy]	α[c]	Type[d]
a	10:11:05.3	-04:42:40.3	410 ± 110	-0.7 ± 0.1	SF-C
b	10:11:06.4	-04:42:10.3	730 ± 170	-1.4 ± 0.5	SF-C/D
c	10:11:09.5	-04:41:56.7	136 ± 110	-0.2 ± 0.2	bkgd?
d	10:11:10.2	-04:41:34.9	131 ± 30	-0.1 ± 0.3	SF-C/D
e	10:11:01.0	-04:40:20.1	402 ± 140	-0.5 ± 0.1	bkgd
f	10:10:54.7	-04:41:14.5	490 ± 100	-2.2 ± 0.8	SF-D
g	10:10:57.5	-04:43:24.4	———	———	SF-N

Table 7: Radio continuum characteristics of Sextans A regions

[a] Radio continuum sources in Sextans A are labeled in Figure 12a.
[b] Uncertainties given are the flux density rms within the given continuum emission region. The rms of the Sextans A C-band image background for purposes of point source detection is 11.6 μJy.
[c] Spectral power law slope for 4-8 GHz, as output by the CLEAN algorithm.
[d] **SF-C** = star cluster; **SF-D** = diffuse; **SF-N** = no radio continuum; **bkgd** = possible background source. Region type determination is described in Section 4.5.7.

3.4.3 Magnetic field in Sextans A

Beck and Krause (2005) derive the relationship between the total (unordered) magnetic field B_{tot} and the measured non-thermal emission, assuming equipartition between the energy of the cosmic rays and the energy in the magnetic field:

$$B_{tot} = \left[\frac{4\pi(1-2\alpha)(K_0+1)I_\nu E_p^{2\alpha-1}(\frac{\nu}{2c_1})^\alpha}{-c_2\alpha L c_3(-2\alpha-1)} \right]^{\frac{1}{3-\alpha}} \tag{3.2}$$

where $I_\nu = S_\nu\Omega$ is the measured intensity of the non-thermal emission in ergs per steradian, K_0 is the ratio between proton and electron number densities, L is the mean path length through the synchrotron plasma, E_p is the proton rest energy, and

α is the synchrotron spectral index. (See Chyży *et al.* (2011), Appendix A; original derivation from Beck and Krause (2005).) The constants are defined as

$$c_1 = \frac{3e}{4\pi m_e^3 c^5} = 6.2648 \times 10^{18} erg^{-2} s^{-1} G^{-1} \tag{3.3}$$

and

$$c_2 = \frac{1}{4} c_4 \frac{\left(\frac{5}{3} - \alpha\right)}{(1-\alpha)} \Gamma\left[\frac{1-3\alpha}{6}\right] \times \Gamma\left[\frac{5-3\alpha}{6}\right], \tag{3.4}$$

with $c_4 = \sqrt{3}e/(4\pi m_e c^2) = 1.86558 \times 10^{-23}$ erg G^{-1} sterad^{-1} . For a completely regular magnetic field with inclination angle i relative plane of the sky, $c_3 = (cosi)^{(1-\alpha)}$. For a completely disordered, turbulent field, $c_3 = (2/3)^{(1-\alpha)/2}$. Lacking polarization measurements, we assume the latter case.

Because of the small physical size of Sextans A, and the fact that our detection is associated with only one star forming region, we set the synchrotron pathlength $L = 1$ kpc. The electron to proton ratio is set by the acceleration mechanism; for strong shocks in a non-relativistic medium, $K_0 \simeq 50$. In the solar neighborhood, K_0 is measured to be ~ 100 for cosmic rays in the energy range relevant to synchrotron emission.

Taking $K_0 = 100$ and $\alpha_n = -1.5$, our Sextans A detection implies a total magnetic field of $B_{tot} = 6.5\mu$ G — very weak compared to the magnetic fields of large spiral galaxies, but typical for most dwarf galaxies (Chyży *et al.*, 2011). Of course, the exact value is strongly dependent on our assumed α and K_0, neither of which is well-constrained: in Table 2 we therefore list the values of $B_{to}t$ derived for Sextans A, for $50 < K_0 < 150$ and $-1.0 < \alpha_n < -2.5$. In general, higher values of α and K_0 both lead to stronger magnetic fields. Based on these unknown, we use a nominal value of $B_{tot} = 5.0$ μG with an uncertainty of ± 1.5 μG. This value is two times higher

than the upper limit estimated by Chyży *et al.* (2011) ($B_{tot} < 3.1\mu$G), largely due to the steeper spectral slope.

One final source of uncertainty worth mentioning is the volume of by the magnetized plasma. We set the line-of-sight pathlength throughout the plamsa to 1 kpc based the typical size scale of outflows seen in edge-on dwarf galaxies; if all the emission is confined to the disk, the inferred magnetic field increases. Likewise, the areal extent of the emission is included in the radiation intensity $I_\nu = S_\nu \Omega$ where S_ν is our detected flux and Ω is the entire $5.9' \times 4.9'$ subtended by the galaxy (2.4 kpc $\times$2.9 kpc at the distance of Sextans A). But the actual detection was clearly localized around the brightest star forming region. If we restrict our solid angle Ω to the $44''$ beam resolution, our nominal total magnetic field strength increases to $B_{tot} = 15.2\mu$ G. The local magnetic fields in the observed HII region could higher still if our detection arises from an area much smaller than our resolution element.

Table 8: Total magnetic field strength B_{tot} of Sextans A, as a function of the proton-to-electron ratio K_0 and spectral index α_n.

K_0 vs. α_n	$\alpha_n = -1.0$	$\alpha_n = -1.5$	$\alpha_n = -2.0$	$\alpha_n = -2.5$
$K_0 = 50$	3.258 μG	4.323 μG	5.677 μG	7.148 μG
$K_0 = 100$	3.865 μG	**5.032 μG**	6.508 μG	8.093 μG
$K_0 = 150$	4.273 μG	5.503 μG	7.054 μG	8.707 μG

3.4.4 Star Formation Rate

A high Hα luminosity and low far-infrared luminosity imply very different star formation rates for Sextans A. The total far-IR luminosity from 40-120 μm can be estimated from the galaxy's *IRAS* 60 μm and 100 μm luminosity via Helou *et al.* (1988):

$$L(FIR) = 1.26\ [2.58\ L_{\nu}(60\mu m) + L_{\nu}(100\mu m)] \tag{3.5}$$

From this we can derive the star formation rate via the relation of Kennicutt (1998):

$$\frac{SFR(FIR)}{1 M_{\odot}\ yr^{-1}} = \frac{L(FIR)}{5.8 \times 10^{9} L_{\odot}} \tag{3.6}$$

For Sextans A $log[L(FIR)] = 6.217$, and $SFR(FIR) = 0.00028 M_{\odot}$ yr^{-1}. This is almost an order of magnitude less than the star formation rate derived from the extinction corrected Hα luminosity, $SFR(H\alpha) = 0.002 M_{\odot}$ yr^{-1} (Mateo, 1998; Kennicutt, 1983). Note that the Kennicutt SFR/FIR relation was originally calibrated via Hα observations of bright galaxies—so the Sextans A dwarf is very discrepant indeed.

How does the radio continuum relate to these conflicting star formation measures? The thermal contribution S_T to the measured L-band continuum flux can be estimated from the integrated Hα flux of the galaxy after Caplan and Deharveng (1986):

$$\left(\frac{S_T}{mJy}\right) = 3.57 \left(\frac{T_e}{10^4 K}\right)^{0.52} \left(\frac{\nu}{GHz}\right)^{-0.1} \left[\frac{F(H\beta)}{10^{-12}\ erg\ cm^{-2}\ s^{-1}}\right] \tag{3.7}$$

Because we are only able to detect the continuum emission from the brightest Hα complex, we subtract only the thermal contribution from these regions. Hodge *et al.* (1994) derived the luminosity distribution of the ionized regions of Sextans A via narrow-line Hα imaging. Our detection corresponds to their HII regions $\#16 - \#22$,

which have a combined Hα flux of 6.02×10^{-13} erg cm^{-2} s^{-1}. We refer to the spectroscopic observations of Sextans A by Skillman *et al.* (1989), and apply a ratio Hα/Hβ = 2.71, and an electron temperature $T_e = 2 \times 10^4$K. Intrinsic reddening is (unsurprisingly) found to be quite low in Sextans A. We derive a thermal free-free contribution to the 1.35 GHz emission of $S_T \sim 1.10$ mJy. The implied star formation rate of stars with $M \geq 5M_\odot$ can be estimated from the remaining non-thermal component via Condon (1992):

$$\frac{SFR(NT)}{1M_\odot\ yr^{-1}} \sim \left(\frac{GHz}{\nu}\right)^{\alpha} \left[\frac{L_{NT}}{5.3 \times 10^{21}\ WHz^{-1}}\right] \tag{3.8}$$

For a spectral slope of $\alpha = -1.5$ this relation yields an estimated star formation rate of $SFR(NT)) \sim 0.00017M_\odot$ yr^{-1}; for $\alpha = -2.0$, it yields $SFR(NT) \sim 0.0002M_\odot$ yr^{-1}. These values are an order of magnitude smaller than $SFR(H\alpha)$, consistent with the star formation rate derived from the far-infrared luminosity.

The agreement between SFR(NT) and SFR(FIR) does not necessarily mean that these should be preferred over SFRHα as the *true* star formation rates. Radio continuum and far-infrared deficiencies are often observed in extremely low-metallicity galaxies (see discussion below), and the Sextans A flux ratios are completely consistent with this interpretation.

3.4.5 Low Metallicity vs. Low Mass

Can we safely attribute the steep spectral slope (and the implied 2.64 GHz radio deficiency) of Sextans A to its extreme metallicity? The large infrared luminosity of most starburst galaxies is generally attributed to warm dust in the vicinity of high-mass star-formation produce less dust and consequently which generally attributed to lower dust masses. Extremely low metallicity environments are typically observed

to have lower intrinsic extinction and lower infrared luminosities (W08) and inferred smaller dust masses in the absence of metals, particularly when compared to their Hα luminosities and derived star formation rates.

The generally faint radio luminosities of Sextans A and other low-metallicity galaxies are in better agreement with the far-infrared luminosity than with the Hα flux. But the effects of metallicity are less clear when the radio/IR relation is viewed in detail. Hunt *et al.* (2005a) (HBM05) have compiled spectral energy distributions from 300 MHz to 6 GHz for a sample of low-metallicity blue compact dwarf galaxies. This sample includes 1 Zw 18 and SBS 0335-052, which have metallicities even lower than that of Sextans A (see previous section). In contrast to Sextans A, HBM find radio spectra which are generally *flatter* than usual, with $\alpha \leq 0.6$; three of their BCDs have essentially flat radio spectra, consistent with purely free-free thermal emission. HBM find q_{FIR} ratios for these objects which are higher than average; W08, meanwhile, find a general trend that q-values drop with metallicity.

The overall low luminosity the radio continuum and IR emission from Sextans A are both consistent with metallicity effects, but the steep spectral index is apparently unique among observed galaxies. Rather than being directly tied to metallicity, we suggest that the steep spectral index is more likely due to the observed outflows coupled with the low mass of the galaxy. Sextans A has a rotational velocity of $v_{HII} = 19 \pm 2$ km/s (Skillman *et al.*, 1988) and an estimated total mass of order $\sim M_{tot} = 4.0 \times 10^8 M_\odot$ (Mateo, 1998); very little energy is required to remove enriched gas permanently from this gravitational potential. The same outflows which remove the products of stellar evolution before they can be incorporated into the next generation of stars could likewise allow for the preferential escape of the highest-energy electrons,

producing a steep spectral index and an under-luminous radio continuum at higher frequencies.

3.5 Conclusions

We have detected radio continuum emission from the star-forming, low-metallicity dwarf galaxy Sextans A in L-band, S-band, and C-band. The primary detection is centered on the main star-forming region, with $S_{4.8GHz} = 1.3$ mJy ± 0.3 mJy. We measure a power-law index of $\alpha = -1.45$. This spectral index is considerably steeper than what has been observed for other nearby dwarf galaxies and low-metallicity galaxies. We derive a magnetic field strength of 5.0 μ G ± 2.5 μG, with most of the uncertainty arising from our assumptions about the physical size of the emission area, the proton-to-electron ratio of the plasma, and the exact slope of the synchrotron spectral index. This field strength is consistent with other dwarf galaxies in the Local Group.

Despite the intense star formation and large-scale winds seen in narrow-band Hα optical imaging of Sextans A, the detected radio continuum emission is very faint. The star formation rate derived from the non-thermal component is a full order of magnitude less than the rate derived from the galaxy's Hα luminosity, in line with the lower rate derived from the galaxy's faint far-infrared emission. This discrepancy between far-infrared and radio continuum luminosities and integrated Hα luminosity is consistent with observations of other low-metallicity galaxies. At higher frequencies, the steep spectral index $\alpha = -1.5$ implies radio emission deficiencies, which are apparent when we try to compare with the radio/far-IR relation measured for Local Group dwarfs at 2.64 GHz. Rather than a metallicity effect, we suggest that the steep

spectral slope may be more directly tied to the observed outflows and low overall mass of the Sextans A galaxy, which permits the easy escape of the highest-energy electrons, leaving behind a population of charged particles skewed towards the lowest energies.

Chapter 4

THE FAR-INFRARED RADIO RELATIONSHIP AT LOW METALLICITY

4.1 Introduction

Of the various empirical star-forming relationships commonly used to relate observable galaxy fluxes to overall star-forming rate (see Chapter 1), the radio/infrared correlation is perhaps the least well-understood. First presented by van der Kruit (1971, 1973), this relation links the radio continuum luminosity of a galaxy to its infrared luminosity. This relationship has proven to be extremely robust, with only 0.3 dex of scatter over 5 orders of magnitude in galaxy luminosity (Yun *et al.*, 2001) in the local universe. While it is expected that this relationship should change in the early universe, where the cosmic radiation background limits the ability of the dust to cool efficiently, to date the relationship has shown no change out to redshifts of $z \sim 2$ (Sargent *et al.*, 2010; Mao *et al.*, 2011).

The most straightforward description of the underlying physical processes driving the radio/IR correlation is the calorimeter model of Völk (1989). This model posits that all the ultraviolet output of the young stars is reprocessed by dust as infrared radiation– e.g. the dust acts as a UV photon calorimeter. Similarly, if all of the energy of the electrons accelerated by supernova is eventually lost in the form of synchrotron emission, the non-thermal radio continuum likewise behaves as a synchrotron calorimeter. Given the short lifetimes of massive stars, we expect their rate of creation to be effectively identical to their rate of destruction; we therefore expect the supernova rate to be

directly proportional to the current rate of on-going star formation. This simple model explains the linearity of the radio/IR relation over so many orders of magnitude.

For star-forming galaxies with low masses (below $< 10^9 M_\odot$) we would expect the assumptions of the calorimeter model to break down. In particular, we expect that as the dust mass decreases due to lower-metallicity environments, the ultraviolet radiation is able to escape without being converted into infrared radiation. Indeed, in Chapter 1, numerous authors reported just such a diminishing of the infrared radiation relative to the Hα luminosity. However no corresponding break-down of the radio/IR relationship is observed: the linearity of the radio/IR relationship appears to be preserved to the lowest luminosities currently measured. Bell (2003) describes this as a "conspiracy": both halves of the calorimeter model break down simultaneously at low mass, for astrophysically distinct reasons, but both with the effect of lowering the measured luminosity of the galaxy relative to the Hα luminosity. Because, these break-down are happening in parallel, the radio/far-infrared relation still appears to hold at low luminosities.

4.2 The Spectral Energy Distribution of Galaxies at Radio Frequencies

Figure 14 shows the spectral energy distributions (SEDs) of two bright, nearby star-forming galaxies, NGC4945 and M82, for which complete coverage of the radio to infrared wavelenghts is available from the *Planck* and *WMAP* missions (Peel *et al.*, 2011). The galaxy SEDs are modeled with a summation of three astrophysical emission sources: non-thermal synchrotron, thermal free-free, and thermal dust emission:

$$S_\nu = A_{sync}\ \nu^\alpha + S_{ff} + \frac{A_{dust}\ h}{k} \frac{\nu^{\beta+3}}{e^{h\nu/k_B T_{dust}} - 1} \tag{4.1}$$

In a normal starburst, the radio spectrum at frequencies below $\nu < 50$ GHz (the centimeter range) is dominated by non-thermal synchrotron emission; at frequencies above $\nu > 50$ GHz (the millimeter and sub-millimeter wavelength range), the SED is dominated by thermal dust emission. Depending on the age of the starburst, thermal free-free may dominate the middle frequency range between $10 < \nu < 200$ GHz, where the dust emission and synchrotron both fall off. I briefly describe the underlying physics of each of these three emissions mechanisms, and the consequent frequency dependence of the SED in the radio and far-infrared.

4.2.1 Graybody Dust Emission

For typical dust temperatures of $T_{dust} \sim 20$ K, we expect the radio SED to largely sample the Rayleigh-Jeans tail of the thermal dust emission. However, a fit to the far-infrared and microwave emission of M82 and NGC 4945 show that the actual frequency dependence rises more steeply than the expected $\sim \nu^{-3}$ power law of blackbody emission (Figure 14). The observed frequency dependence of the thermal dust is better described by the power-law formula for graybody emission:

$$S_{dust} = N_{grains}\ \pi a^2 Q_{abs}^2(\nu_0)\ (\frac{\nu}{\nu_0})^{\beta}\ B_{\nu}(T_{dust}) \tag{4.2}$$

where k_B is Boltzmann's constant, h is Planck's constant, and c is the speed of light. The additional exponent β is the dust emissivity which reflects the fact that dust grains of different sizes are imperfect absorbers, due to their quasi-quantum mechanical sizes, and consequently function as poor blackbodies. At millimeter and sub-millimeter

wavelegths, the thermal dust emission can be adequately described by the graybody equivalent of the Rayleigh-Jeans approximation, with $S_{dust} \sim \nu^{\beta+3}$.

The graybody approximation also changes the wavelength of the expected Wien peak emission for a given temperature:

$$\lambda_{max} T_{dust} = 2900 \ \frac{5}{\beta + 5} \ \mu m K \tag{4.3}$$

If the data include mid-and far-infrared observations, such that our SED adequately samples the Wien maximum, we will also be able to derive an estimate of the overall cold dust temperature, T_{dust}. A complete sampling of the Rayleigh-Jeans tail only exists for the handful of galaxies that are bright enough to resolve from the microwave background with *Planck* and *WMAP*, but mid- and far-infrared coverage of the Wien maximum does exist for many bright galaxies via *Herschel* and *Spitzer*. This is generally not the situation for the low-metallicity dwarf galaxies in my sample, as I will discuss in subsequent sections.

4.2.2 Synchrotron Emission

At centimeter wavelengths, the spectral energy output begins to rise again, as the non-thermal synchrotron emission begins to dominate the galaxy's output. Synchrotron emission is produced by relativistic charged particles accelerated in the presence of the galaxy's ambient magnetic field. The bulk of these particles are assumed to be electrons, whose low masses allow them to be accelerated more efficiently to relativistic velocities in e.g. supernova shocks. If the velocity of an electron is has a component

which is perpendicular to the ambient magnetic field of the galaxy, the trajectory will be deflected to spin the electron around the field line.

In the non-relativistic case this electron will emits radiation at the classic cyclotron gyrofrequency, $\nu_g = eB/2\pi m_e$. As the we increase the velocity of the electron into the mildly relativistic case $v < 0.1c$, an increasing amount of energy will be radiated at the harmonics of the gyrofrequency, where

$$\frac{(dE/dt)_{l+1}}{(dE/dT)_l} \approx (\frac{v}{c})^2 \tag{4.4}$$

where the integer value $l = 1, 2, 3...$ and $l = 1$ is the gyrofrequency. As the relativistic velocity increases, these harmonics will also broaden in frequency space, as the beamed emission from the radiating electron will be doppler shifted towards and away from the observer as it spins around the magnetic field line.

The fully-detailed derivation of the synchrotron spectrum of a single relativistic electron is quite complex (Ginzburg and Syrovatskii, 1965); the most thorough textbook analysis is widely acknowledged to be Rybicki and Lightman (1985). A somewhat more approachable (but not overly-simplified) treatment of the derivation is presented in Longair (1992, chapter 18). The general results are that the high frequency emissivity of the electron will be rapidly cut off at frequencies above the relativistic gyrofrequency:

$$\nu_c = \frac{3}{2}\gamma^2 \nu_g sin(a) \tag{4.5}$$

where γ is the relativistic Lorentz factor, ν_g is the cyclotron gyrofrequency, and a is the rotating pitch angle between the magnetic field and the plane of the particle's orbit (see Rybicki and Lightman, 1985, Figure 6.5). At frequencies below ν_c, the

electron's emissivity will be proportional to $\nu^{1/3}$. The beamed cone of radiation from the electron will be confined to a cone with opening angle $\sim 1/\gamma$, which means that the observer will only see a brief pulse of radiation for each orbit of the electron around the magnetic field.

Understanding the synchrotron emission from a distribution of electrons is actually quite a bit simpler than the single electron case. The shape of the resulting emission spectrum is set by the underlying energy distribution of the electrons, and not by the shape of the emission spectrum of an individual particle. If we have an energy distribution of relativistic electrons with $N(E)\ dE \sim E^{-p}\ dE$, our output synchrotron spectrum will be:

$$S_{nt}(\nu) \sim B^{\frac{p+1}{2}} \nu^{-\frac{p-1}{2}} \tag{4.6}$$

where B is the magnetic field strength. The measured spectral index α of the non-thermal continuum is therefore a direct tracer of the power-law index p of the underlying electron energy distribution, with $\alpha = (p-1)/2$.

Synchrotron emission is primarily characterized by the spectral index α, which I previously introduced in Equation 3.1. In the Milky Way, $\alpha = -0.8$ for frequencies above $\nu > 400$ MHz; for frequencies below $\nu < 400$ MHz, the spectral slope becomes shallower, $\alpha = -0.4$. Star-forming galaxies generally exhibit spectral continuum indices around $\alpha \sim -0.7$, though other extragalactic sources (quasars, radio halos) often have flatter or steeper spectral indices. Resolved star forming regions within nearby galaxies may also have distinct spectral indices; the steepening of the spectral index is usually interpreted as a marker of synchrotron aging, resulting from the most energetic particles losing energy over time (see e.g. Linden, 2017).

4.2.3 Thermal Free-Free Emission

The final component to the continuum radio spectrum of any star-forming galaxy is the free-free emission. In any hot plasma, free electrons will be periodically deflected by the ions they have been stripped from–hence the moniker "free-free". This periodic deceleration ("braking") of the electron requires the emission of a photon in order to conserve momentum. This the origin of the German word *bremsstrahlung*: "braking"–*brems* + "radiation"–*strahlung*.

While this emission mechanism is quite distinct from the "true" thermal blackbody emission, the electrons and nuclei are generally considered to be in thermal equilibrium; consequently this component of the radiation field is referred to as "thermal bremsstrahlung". Any hot plasma is expected to have plenty of free electrons and ions, so bremsstrahlung will always be associated with high-mass star forming regions, with an overall luminosity that depends on the gas temperature and density. At radio frequencies, the continuum emission from any star-forming galaxy to be a combination of non-thermal synchrotron and thermal bremsstrahlung emission.

Following the analysis from Chapter 3, I estimate the thermal contribution to the radio continuum from the Hα flux of the galaxy, using the relation of Caplan and Deharveng (1986) (see Equation 3.7). I fit the thermal free-free component in Equation 4.1 with a power law dependence of $S_{ff} \sim \nu^{-0.1}$.

4.2.4 The Expected Radio SED at Low Metallicities

From Figure 14 we can see that the radio/infrared SEDs of star-forming galaxies are all very similar, even for galaxies which are physically quite distinct. NGC 4594 is a

large spiral galaxy, almost ten times more massive the Milky Way; M82 is starbursting dwarf irregular, physically smaller than the Milky Way, but more than five times more luminous. Despite their apparent differences in size and morphology, their SEDs are qualitatively very similar, with similar dust temperatures ($T_{N4594} = 18.9$K; $T_{M82} = 24.8$K) and synchrotron spectral indices ($\alpha_{N4594} = -1.15$; $\alpha_{M82} = -1.11$).

At lower metallicities, we expect the astrophysical conditions regulating the shape of the SED to change. A lack of UV shielding and harder ionizing fluxes means that the dust temperature is expected to be warmer, though the overall column density of dust is expected to be lower. Higher plasma temperatures in ionized regions will lead to an increase in the relative contribution of the free-free emission. The escape of relativistic electrons into the IGM will reduce the contribution of the the non-thermal synchrotron emission, leading to flatter radio spectral indices.

Spitzer observations of blue compact galaxies have provided evidence for harder ionizing fields (see e.g. Wu *et al.*, 2006) and dramatically warmer dust temperatures in low metallicity environments (Houck *et al.*, 2004; Engelbracht *et al.*, 2008). There is less information about the lower frequency synchrotron continuum. For a handful of luminous blue compact galaxies, including the extreme dwarfs I Zw 18 and SBS 0335-052E, multi-frequency radio continuum observations indicate that the spectral slope of the radio continuum between 1.4 GHz and 20 GHz is flatter than typical, with $-0.1 < \alpha < -0.4$ (Hunt *et al.*, 2004, 2005b; Cannon *et al.*, 2005). These authors interpret these shallow slope as indicative of young star formation events, where the thermal free-free contribution approaches that of the non-thermal synchrotron. But as was shown in Figure 3, radio continuum observations of other low metallicity dwarf galaxies have mostly produced upper limits rather than detections (Wu *et al.*, 2008; Chyży *et al.*, 2011). The upgraded *JVLA* has the sensitivity to correct this situation,

as verified by our detection of Sextans A outlined in the previous chapter, and by recent observations of Local Group dwarfs by Hindson *et al.* (2018).

4.3 JVLA Observations

The data presented in this chapter were taken at the *JVLA* during the 2015B semester. The observed galaxies are a subset of the low-metallicity sample described in Chapter 2–specifically the subsample that has pre-existing mid- or far-infrared observations, which I will need in order to study the radio/IR correlation. The observations are summarized in Table 9.

Additional S- and C-band observations of Sextans A were also taken during the 2015B semester, under the same program ID; these are summarized separately in Chapter 3, with the 2013A L-band observations of that galaxy.

4.4 Data Calibration and Imaging

Unlike the Sextans A data, which were calibrated manually following the outline of the *JVLA* wideband continuum tutorials, all of the data in this chapter were initially calibrated using the JVLA pipeline in CASA v.4.7.2. While polarization calibrators were observed for each galaxy, this version of the pipeline was not able to do polarization calibration; this must be done separately afterwards. Most of this sample is expected to be too faint for meaningful polarization measurements, so this step was omitted in this analysis.

Table 9: Summary of JVLA observations of low-metallicity sample

Galaxy	RA	Dec	Obs Date[a] [UTC]	Time[a] [UTC]	T_{int}[b] [min]
L-band observations					
II Zw 40	05:55:42.6	+03.23.32.0	28-Dec-2015	03:55	30.6
Sextans B	10:10:10.1	+04:19:56.0	30-Dec-2015	13:28	15.2
C-band observations					
SBS 0335-052E	03:37:44.1	+05:02:40.2	24-Dec-2015	04:45	31.7
II Zw 40	05:55:42.6	+03.23.32.0	27-Dec-2015	03:48	31.6
HS 0822+3542	08:25:55.5	+35:32:31.9	18-Nov-2015	09:22	15.8
UGC 4704	08:59:00.3	+39:12:35.7	02-Jan-2016	06:52	31.7
I Zw 18	09:34:02.0	+55:14:28.1	29-Dec-2015	05:11	15.8
SBS 0940+544	09:44:16.6	+54:11:34.2	17-Nov-2015	09:26	15.8
Leo A	09:59:26.5	+30:44:47.0	27-Nov-2015	09:25	15.8
”	”	”	29-Nov-2015	09:13	15.8
”	”	”	22-Dec-2015	07:01	79.1
				Total (Leo A):	110.7
Sextans B	10:10:10.1	+04:19:56.0	07-Dec-2015	08:37	15.8
”	”	”	29-Dec-2015	08:00	59.4
”	”	”	23-Dec-2015	09:35	59.3
				Total (Sextans B):	134.5
SBS 1129+576	11:32:02.5	+57:22:45.6	10-Dec-2015	15:40	15.8
SBS 1415+437	14:17:01.4	+43:30:05.5	30-Nov-2015	16:33	15.8

[a] UTC time and date at start of JVLA observation.
[b] Total integration time on science field.

4.4.1 RFI Flagging

As in Chapter 3, man-made radio frequency interference (RFI) is a source of considerable noise in low-frequency radio data. The Sextans A field was particularly affected by these sources due to its proximity to the geosynchronous belt, at declination

$\delta = -4°$. The presence of bright RFI sources in my data may cause amplifier ringing in the correlated data, which can completely destroy the usability of an entire spectral window. For the Sextans A science field I was forced to throw out the majority of the spectral windows in L-band, and over 1/3 of the available frequency range in C-band. Even with these omissions, so much of the data was impacted by RFI that nearly 50% of the remaining data had to be excised using a combination of automatic and manual flagging.

Fortunately, no additional targets in my low metallicity dwarf sample fall within the geosynchronous belt at $0° < \delta < -5°$ (as seen from the JVLA's latitude). All of the 2015B data were visually examined before pipeline calibration to ascertain the overall impact of RFI, and any extreme interference was manually excised. After pipelining, the calibrated data were flagged automatically using the TFCROP algorithm, and inspected again. As in the case of Sextans A, I determined that entire spectral windows needed to be excised from the calibrated data; the final spectral windows match those listed in Tables 5 and 6. In general, however, these data are much cleaner than the Sextans A fields, at all equivalent frequencies. As a result, these observations tend to reach better or comparable detection thresholds than the Sextans A observations, even with much shorter integration times.

4.4.2 Self-calibration and imaging

After pipeline calibration and RFI flagging, the science fields for each observation were split into separate measurement sets and imaged with the CLEAN algorithm.

Approximately half of the science fields contained one or more bright point sources ($S_\nu \geq 6$ mJy) within the primary beam, which permitted at least one round of self-

calibration. These include HS0822+3542 (6 mJy), SBS 1129+576 (35 mJy), SBS1415 (45 mJy), and Sextans B. At 23 mJy, II Zw 40 is sufficiently bright by itself to serve as a self-calibration source, though the combination of unresolved and diffuse flux makes it comparatively trickier to CLEAN (see Section 4.5.1 for more details). SBS 1129+576 and II Zw 40 both showed significant improvement in both interferometric fringing and background rms. Self-calibration does not significantly improve or degrade the detection thresholds or fringing for HS0822+3542 and SBS1415+437. The C-band image of Sextans B was significantly degraded after self-calibration, so the self-calibration was discarded.

The rest of the science fields–Leo A, SBS 0940+540, I Zw 18, and UGC 4704–lack sufficiently bright sources for self-calibration. For these fields, the phase component of the gain calibration was derived from the phase calibrator, which was typically several degrees distant on the sky. This solidly within the phase calibration tolerances for L-band and C-band low frequency observations at the *JVLA*. When observing at L-band and C-band, the phase angle should be well-constrained over a 30 minute integration, and bracketing observations of a bright phase calibrator within 5-10° do generally provide adequate gain calibration for the fainter sources.

4.5 Results

The final imaged radio continuum data for the entire 2015B galaxy sample are presented in Figure 15- 22. The radio contours are overlaid on optical imaging of the galaxies, which demonstrates general association between young star clusters and the radio continuum emission. The optical imaging of this sample comes from a fairly heterogenous collection of sources. For the blue compact galaxies, high resolution

Hubble Space Telescope imaging is preferred, but this is not always available, and typically not in the sample wavebands. Hα imaging is especially valuable, as this shows the position and intensity of current and ongoing star formation.

In the following sections, I discuss the imaging general results for each galaxy separately.

4.5.1 II Zw 40

II Zw 40 is both the most metal-rich and the brightest source in my *JVLA* sample: with $f_\nu = 23$ mJy, it is bright enough to use a self-calibration source. The measured flux of the galaxy is a combination of both resolved and unresolved components, which requires a custom deconvolution strategy. I obtained the best results by performing a shallow point-source CLEAN on the central, unresolved source ($N_{iter} = 50 - 80$ cycles), followed by a deeper CLEAN of all the point sources revealed at this point. I then re-ran CLEAN on the same image with multi-scale components, and removed the diffuse emission around II Zw 40. A single round of self-calibration subsequently produced significant improvement interferometric fringing associated with II Zw 40, and improved the background rms by 33%.

Interpreting optical imagery of II Zw 40 can be a bit tricky due to its position in the sky: it is at a Galactic latitude of ($b = -10.77°$), in the constellation Orion. This puts it squarely behind one of the closest and most well-known molecular cloud complexes in the Milky Way, along a severely reddened line of sight with $E(B-V) = 0.728$. This situation is unfortunately not uncommon among dwarf starbursts: two other well-known starbursts in the local volume, IC10 and NGC 1569, are both at comparable Galactic latitudes, with $b = -3.33°$ and $11.24°$ and $E(B-V) = 1.386$ and 0.613,

respectively (see Table 1). In the UV/optical range, most of the ultraviolet and blue light from II Zw 40 will be extincted, and emission line diagnostics such as the Balmer decrement will be unreliable. At longer wavelengths, Galactic synchrotron and infrared cirrus may contaminate the science field. The larger angular size scales of Galactic emission should average out over the *JVLA* field of view, but caution is warranted.

In ground-based optical and near-infrared imagery, II Zw 40 exhibits a highly disturbed structure, with two broad tidal tails extending to the south and southeast to form an inverted "V" (Figure 15a). The Hα emission is strongly concentrated the core of the galaxy, near the apex of the "V", with fainter clumps of star formation regions scattered along both tails (Figure 15b). The radio continuum emission is likewise concentrated around the core, but there is considerable diffuse emission tracing the extended star formation features, particularly along the southeastern tidal tail. 40-50% of the total radio continuum of II Zw 40 originates with the diffuse component. Archival *HST* images of II Zw 40 (PI: Chandar, Prop ID: 9739; first published and described by Kepley *et al.* (2014)) taken with the Advanced Camera for Surveys High Resolution Camera (ACS/HRC) reveal two bright cores, consistent with a recent major merger (Figure 15c). Kepley labels these Super-Star Clusters North and South (SSC-N and SSC-S). The *HST*/ACS $F568N$ narrow-band Hα filter reveals that the bulk of the starburst activity is concentrated around SSC-N.

The *JVLA* should not have sufficient resolution to separate these two cores at low frequencies in *D*-configuration, but CLEAN deconvolution models the emission as a point source near the position of SSC-N, offset from a broader component centered around SSC-S, which is qualitatively similar to the *HST* Hα image. The diffuse component of the radio continuum traces the Hα emission in the tidal tails, with more emission concentrated along southeastern tail than along the southern tail. Diffuse

infrared emission associated with the southeastern tail was also observed by Wu *et al.* (2006) at 22 μm. It may be possible to a small-scale ($d < 1$ kpc) analysis of the infrared/radio relation in this galaxy, similar to the analyses of Tabatabaei *et al.* (2007, 2013b,a).

In Figure 15e, I overplot the radio continuum spectral index α, as estimated by the CLEAN algorithm, with the flux density contours from Figure 15a. Estimating the spectral index requires flux density measurements at two different frequencies, with α defined in Equation 3.1. Even after discarding spectral windows most impacted by RFI the WIDAR correlator provides near-continuous spectral coverage of the C-band frequency range between 4.8-7.2 GHz (see Table 6). This means that the spectral index maps output by the CLEAN algorithm should be fairly robust in high SN regions. However, there are some caveats: the angular size of the primary beam varies by 30% over the observed frequency range, so the total flux correction will varies according to frequency across the field of view. The CASA task *widebandpbcor* corrects for this effect, but the spectral index maps will still be unreliable around the edges of the primary beam. Likewise, the interferometrically resolved beam also varies by a factor of 30%; between the varying beam size and the lower SN, the often wildly-varying α values at the outer edges of point sources should probably be regarded as spurious.

What does the spectral index tell us? Potentially it can tell us about the fractional contribution of the thermal and non-thermal emission, the strength of the magnetic field, and the age of the most recent star forming episode. Recall that the expected spectral index of free-free thermal emission is $\alpha = -0.1$, while the spectral index of the Milky Way's non-thermal synchrotron flux is $\alpha \sim -0.7$. Synchrotron emission can have a variable spectral index, depending on the magnetic field and the energy distribution of the generating relativistic electron population; the most energetic

electrons lose their energy fastest, generally as it the spectrum steepens as the electron population "ages".

Several authors have observed the radio continuum II Zw 40 in the past, though this is the deepest and most sensitive study to date. In particular, Kepley *et al.* (2014) imaged the core of the II Zw 40 with the pre-upgrade *VLA*, using the $B-$, $A-$, and $A+$ Pie Town configurations, using the C, X, and K band receivers (4.86, 8.46, and 22.46 GHz). Their highest-frequency images achieve a beam resolution of $0.14\ddot{} \times 0.12\ddot{}$, which is within a factor of two of the *HST* resolution ($0.06\ddot{}$). They measure a flux density of 10.1 mJy for the central region of II Zw 40, which is consistent with the flux within the central 10öf my images; the A-configuration data are not sensitive to the diffuse component. Their spectral coverage gives them a solid handle on the spectral index: the ratio of the X- and K-band fluxes are consistent with $\alpha \sim -0.1$, or purely thermal emission. The C-band flux is higher than a purely thermal model would suggest, implying a non-thermal synchrotron component of 20% in the center of the galaxy.

I use the ratio of their C- and X-band flux densities to test the robustness of the spectral index maps output by the CLEAN algorithm. From Kepley et al.'s Table 3, they find $S_{4.86} = 10.1$ mJy and $S_{8.46} = 8.0$ mJy; from the equation 3.1, this gives $\alpha = -0.42$, which is quite close to CLEAN's spectral index of $\alpha = -0.3$ for the core of II Zw 40.

Figure 14: The radio-infrared spectral energy distribution of a normal star-forming galaxy

(a) NGC 4945

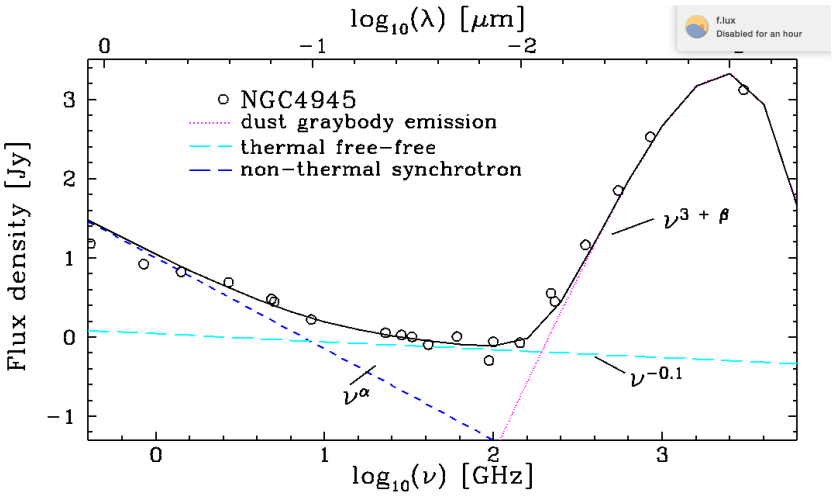

(b) M82

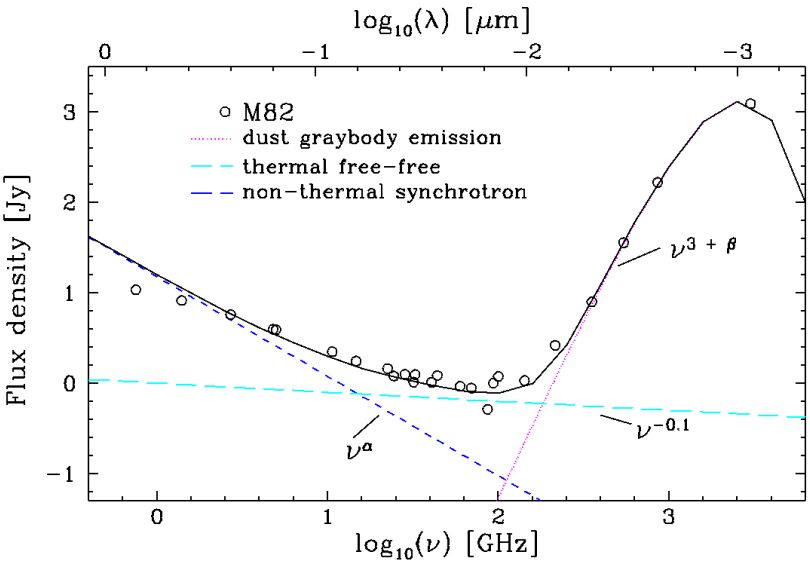

(c) Spectral energy distributions (SEDs) of a normal star-forming galaxies (NGC 4945) and a starbursting dwarf galaxy (M82), from Peel *et al.* 2011. The microwave data are from the *Wilkinson Microwave Anisotropy Probe (WMAP)*; the far-infrared data are from *Planck*; archival data points are from ground-based radio observations and the *IRAS* satellite. The magenta dashed line is the fit to the non-thermal synchrotron; red is the thermal free-free emission; blue is the thermal blackbody emission from gray dust with T= 20K. The solid black line is the combined fit of all three emission components.

Figure 15: II Zw 40

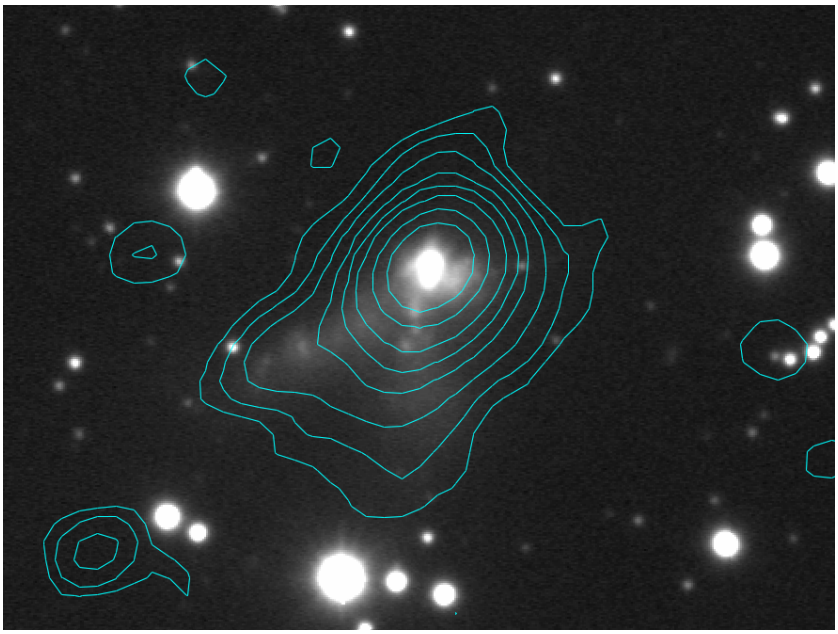

(a) C-band flux density contours for II Zw 40. Radio continuum contours are at 0.025, 0.05, 0.1, 0.25, 0.5, 1, 2, and 5 mJy/beam. Underlying image is R,-band, from Gil de Paz *et al.* (2003a), obtained via NED. Radio continuum is a combination of a bright unresolved core, centered on the starburst, and a diffuse component which traces the visible tidal tails.

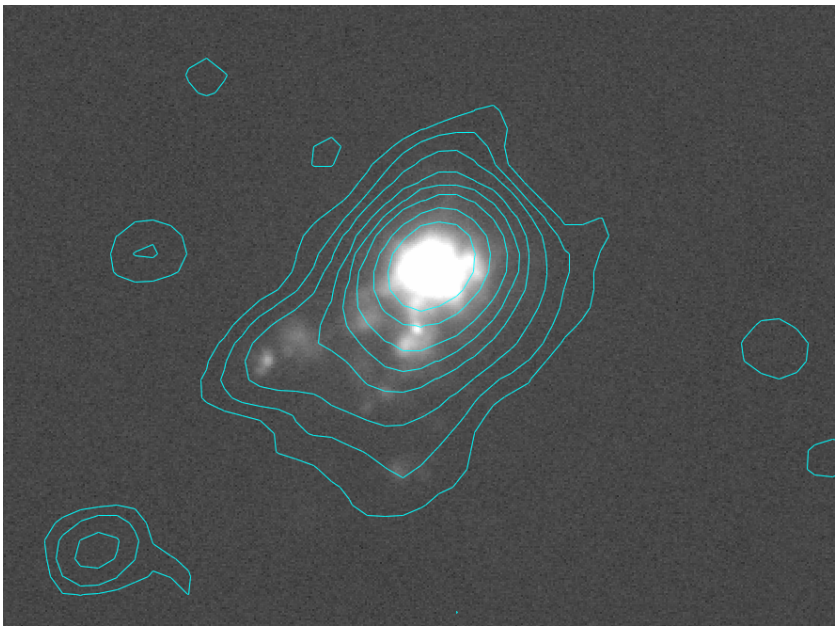

(b) C-band flux density contours for II Zw 40, compared to Hα emission. Radio continuum contours are identical to above. Underlying image is Hα from Gil de Paz *et al.* (2003a), obtained via NED. .

Figure 15: II Zw 40

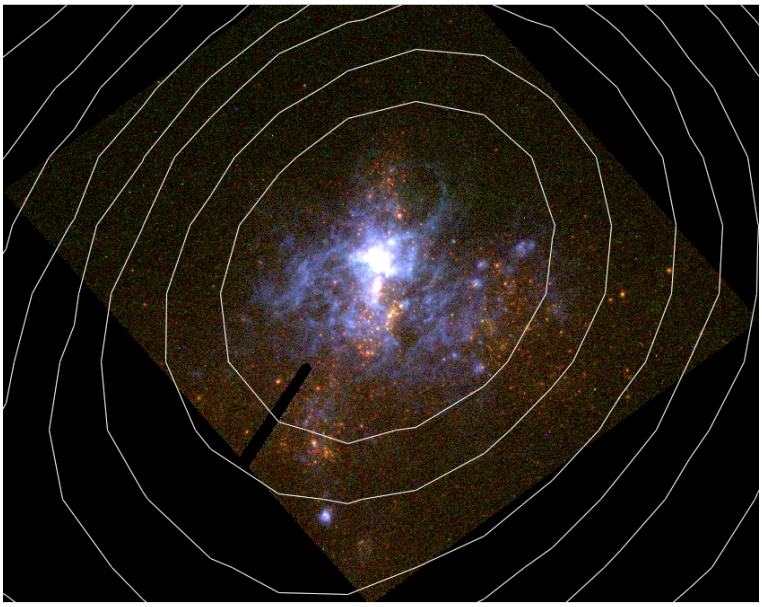

(c) Comparison of C-band radio continuum with the high-resolution HST/ACS imaging of the core of II Zw 40. Radio continuum contours are identical to Figure 15a. RGB color assignments are R = $F814W$, G = $F555W$, B = $F658N$ (Hα). HST images were obtained via MAST. At higher resolution, the central area of II Zw 40 is resolved into two bright cores. While both cores are comparably bright in wide-band imaging, the northern-most core is considerably bright in Hα. The JVLA does not resolve these two separate cores in D-configuration, and the C-band emission is not clearly centered on one or the other.

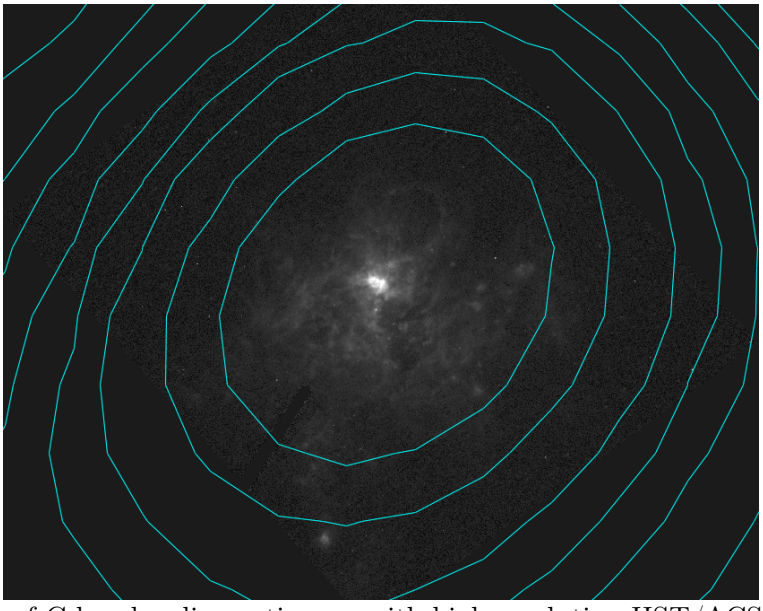

(d) Comparison of C-band radio continuum with high-resolution HST/ACS imaging of the Hα emission. Radio continuum contours are identical to Figure 15a. Hα imaging is from Dale *et al.* (2009), obtained via NED. The Hα regions in Leo A are very faint and diffuse, and not clearly associated with star clusters or other optical point sources. The radio continuum is similarly faint, and tends to be associated with Hα regions, though the association is not as strong as in Sextans B. The labeled sources are listed in Table 10.

Figure 15: II Zw 40

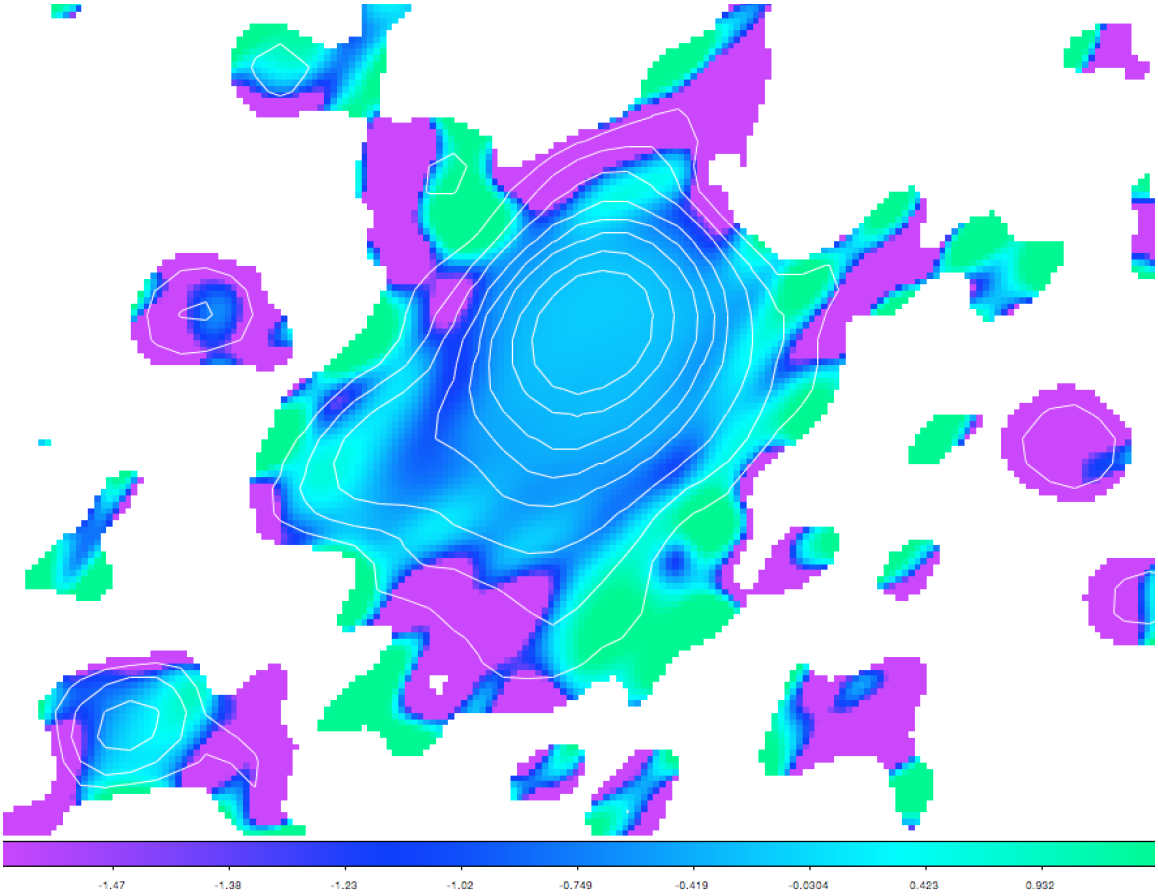

(e) Map of C-band continuum power law slope α of II Zw 40, as output by the CLEAN algorithm. White contours are the C-band flux density (see Figure 15a). The central regions of the starburst have a very flat spectral index, $\alpha \sim -0.3 \pm 0.2$. The spectra indices derived from CLEAN become less reliable farther out, particularly at the edges of the diffuse emission, where the difference in the size of the resolved beam between 4 - 8 GHz becomes the dominant effect. Nevertheless, a steepening of the spectral index ($\alpha \sim -0.7$) is apparent along the eastern and southeastern tails.

4.5.2 HS 0822+3524

Discovered by Kniazev *et al.* (2000), this blue compact dwarf is a true XMD, with an oxygen abundance less than 1/20th Solar. In most ground-based imaging (including

my own emission-line observations) this galaxy appears as a single point. Gil de Paz *et al.* (2003a) report that this may be one of the few extremely compact objects in their sample (along with I Zw 18 and Pox 186) which lacks a fainter underlying halo of evolved stars; however in their broad band B and R imaging there is a hint of an extended, redder disk extending north-westward of the compact source (see Figure 16). An extended underlying disk is faint but clearly discernible in the *HST* imaging.

While the C-band continuum flux is squarely centered on the dominant star forming region, the large *JVLA* beam in this configuration covers the entirety of the extended disk, so contributions from the rest of the disk cannot be completely ruled out without higher resolution imaging.

4.5.3 UGC 4704

UGC 4704 is a nearby edge-on disk galaxy. Its recession velocity puts it well outside of the Local Group, but it still near enough to be included in the Local Volume sample ($D < 11$ Mpc) of Dale *et al.* (2009). The galaxy's general morphology and some individual star clusters are well-resolved in ground-based imaging. Despite its edge-on orientation, no dust lane is visible, consistent with its low circular velocity and the $v_c < 120$ km/s transition observed by Dalcanton *et al.* (2004). In fact, the broad band colors of the galaxy are strikingly blue, suggesting either a very young or an extremely metal poor stellar population.

The C-band continuum contours and spectral slope are shown in Figure 17 Despite its blue color, the C-band continuum detections are rather weak, with a few unresolved point sources centered on a handful of brighter star clusters. The galaxy is detected in the mid-infrared by Dale *et al.* (2009), with a comparably low luminosity. Overall, the galaxy appears to be in a fairly quiescent state, suggesting the blue integrated color is almost entirely due to the metal poor older population of stars.

4.5.4 I Zw 18

I Zw 18 was famously regarded as the most metal-poor galaxy in the known universe for several decades, eventually losing this title to SBS 0335-052W and then to the recently-discovered Leoncino dwarf. Consequently, it has been heavily studied by almost every observatory in the past few decades, at almost every available

wavelengths. (For example: it is already listed as a planned GTO target with JWST, with observations planned for every instrument on the telescope!)

4.5.5 SBS 0940+544

Also a true XMD dwarf, this galaxy is resolved in ground based imaging, and exhibits an asymmetic disturbed morphology (Gil de Paz *et al.* (2003a)), suggestive of a recent or ongoing interaction. Using the morphological classification system of Loose and Thuan (1986), Gil de Paz classifies the object as BCD type iI, M, an apparent merger.

The observed radio continuum flux associated with SBS 0940+544 is plotted in Figure 18. Unfortunately, this object has not been observed with HST, and no higher-resolution images are currently available; however the Gil de Paz et al. images do provide a general idea of the galaxy's morphology. The radio continuum emission is centered on the bright Hα region, with no apparent emission from the older stellar disk extending to the southeast.

SBS 0940+544 was observed with MIPS Wu *et al.* (2008), as part of their effort to constrain the low-metallicity behavior of the radio-infrared relation. Thye report an infrared detection with MIPS, but only an upper limit in L-band. This is therefore the first radio continuum detection of this object.

4.5.6 Leo A

With a nebular oxygen abundance of $12 + (O/H) \sim 7.3$, Leo A had the distinction of being the most metal-poor galaxy currently forming stars in the Local Group prior to the discovery of Leo P. The star formation is quite low, [number??], making it the most challenging object in this sample to detect, despite being in a favorable part of the sky as viewed from the *JVLA* site ($\delta \sim 33^{\circ}$), with excellent U-V coverage and little RFI contamination.

The radio continuum emission from Leo A is shown in Figure 19. When compared with the broad-band optical and Hα imaging of Leo A, many of the unresolved C-band sources (including several marginal detections) are clearly associated with optical point sources and the faint Hα nebulae. These are labeled a - m, and their measured continuum properties are tabulated in Table 10.

Compared with Sextans B, it is more difficult to clearly delineate which radio continuum sources clearly are and aren't associated with Leo A, and therefore which should or shouldn't be included in the total C-band flux for the galaxy.

Sources a, c and j, are all associated with diffuse Hα nebular emission. Source d is a region of Hα emission with no obvious radio emission–however, when the C-band flux over the area is summed, it is positive, with a S/N of 1.5σ. The cluster of brighter flux sources just north of regions *c* and *d* have no counterparts in any optical imaging, and are assumed to be coincident background quasars. These are excluded from the total flux calculation.

Sources b, e, f, g, i, and l all have reddish, unresolved optical counterparts. Source *b* is associated with a faint point source immediately adjacent to *a*, and is included in the total flux of Leo A simply because its location makes it difficult to avoid.

A position search of the coordinates in NED produces an infrared source, but no nearby background galaxies. Sources e and f, on the other hand are associated with background galaxies: SDSS J095925.46+304509.1 and SDSS J095917.81+304523.0, respectively, with g magitudes of 18.4 and 21.6. Sources f and i are also background galaxies: f is 2MASX J09592000+3045173, with magntitude $g = 18.4$ and redshift $z = 0.19$; i is SDSS J095915.85+304346.3, with magnitude $g = 18.1$ and redshift $z = 0.15$. Sources e, f,g, and i are excluded from the total flux of Leo A.

Regions m and n likewise have reddish, unresolved optical counterparts. These are identified on NED as SDSS J095932.43+304159.7 and SDSS J095940.30+304140.9, respectively, with g magnitudes of 18.6 and 18.5. Both objects are identified as galaxies, but spectroscopic redshifts do not exist for either. Due to their apparent distance from the main stellar concentration of Leo A, the continuum flux from these regions is excluded from the total radio continuum for the dwarf galaxy.

Source h appears as a pair of bright point source in both the broad band and the Hα images, but no radio continuum is apparent at this location–in fact, the sum of the flux for this area is negative. Sources k and l appear as faint point sources in the Hα image, and are included in the total flux for Leo A.

The total flux of Leo A was determined in CASA by drawing a polygon which included a, b, c, d, h, j, k, and l, but excludes all the other sources. This polygon captures some unresolved flux, as well as the point sources. The unresolved flux is about 20% of the total flux. While some of this flux could potentially come from unresolved background sources as well as from Leo A, it is necessary to include it in order to compare with the more distant blue compact galaxies (which will have any diffuse component included as part of their unresolved detected.)

The infrared flux from Leo A is comparably faint. It is not detected by *IRAS*, and

Region[a]	RA [h:m:s]	Dec [d:m:s]	Flux density[b] [μJy]	α[c]	Type[d]
a	09:59:33.3	+30:44:33.3	31.4 ± 5.8	-0.1 ± 0.2	SF-D
b	09:59:32.5	+30:44:28.4	25.7 ± 6.8	-1.2 ± 0.3	SF-C/D
c	09:59:30.5	+30:44:36.8	22.3 ± 4.0	-2.0 ± 1.0	SF-D
d	09:59:27.8	+30:44:56.3	11.1 ± 4.3	———	SF-D/N
e	09:59:25.6	+30:45:09.8	18.2 ± 4.5	-1.7 ± 0.6	bkgd
f	09:59:20.2	+30:45:18.0	76.0 ± 21.2	-0.7 ± 0.1	bkgd
g	09:59:17.8	+30:45:23.3	21.4 ± 10.8	-2.2 ± 0.2	bkgd
h	09:59:07.0	+30:44:27.4	———	———	SF-C/N
i	09:59:15.7.	+30:43:47.3	172 ± 37.2	-1.4 ± 0.2	bkgd
j	09:59:17.6	+30:44:04.5	35.9 ± 5.8	-1.4 ± 0.1	SF-D
k	09:59:20.2	+30:44:01.6	48.7 ± 8.8	$+0.7 \pm 0.2$	SF-C
l	09:59:22.2	+30:44:08.3	37.0 ± 9.3	-1.2 ± 0.2	SF-C
m	09:59:32.5	+30:41:58.6	40.4 ± 9.1	-2.2 ± 0.8	bkgd
n	09:59:40.3	+30:41:42.3	96.2 ± 26.3	-3.4 ± 0.3	bkgd?

Table 10: 4-8 GHz radio continuum characteristics of Leo A regions

[a] Radio continuum sources in Sextans B are labeled in Figure 20b.
[b] Uncertainties given are the flux density rms within the given continuum emission region. The rms of the Leo A C-band image background for purposes of point source detection is 8.8 μJy.
[c] Spectral power law slope for C-band (4-8 GHz), as output by the CLEAN algorithm.
[d] **SF-C** = compact/cluster; **SF-D** = diffuse; **SF-N** = no radio continuum; **bkgd** = possible background source. Region type determination is described in Section 4.5.7.

Dale *et al.* (2009) report only an upper limit from MIPS; however Cigan *et al.* (2016) is able to determine a total infrared flux by smoothing the Dale et al. MIPS images to match longer wavelength data from the *Herschel* PACS instrument (P. Cigan, priv. communication). I use MIPS 70 μm and MIPS 160 μm fluxes provided by P. Cigan in this analysis; unfortunately the smoothed MIPS 24 data still only provide an upper limit, so the 24 μm flux must be inferred from SED fitting.

4.5.7 Sextans B

Sextans B is located at the outer edge of the Local Group, and is often considered part of a pair with Sextans A (which is discussed in detail in Chapter 3). It has a very similar metallicity to Sextans A, which puts it among the most metal-poor objects in the Local Group. (Only Leo A is more extreme.) In optical imaging, Sextans B resembles a nearby version of HS 0822+3542, with a handful of bright clusters and discrete knots of star formation centrally concentrated in a dim, larger-scale disk of older stars. When the broad band images are smoothed to the point where the indivdual stars are no longer discernible, the long axis of the outermost optical contours of the galaxy are tilted with respect to on another, suggestive of low-level spiral structure.

The radio continuum emission from Sextans B is mapped in Figure 20. The emission is extremely localized, mostly associated with bright star clusters or Hα knots. In Figure 20b I have labeled the brightest individual continuum sources and Hα regions; the continuum properties of these regions are summarized in Table 11. I define the following continuum source types: ***SF-C***, star formation-cluster: these radio continuum sources are associated with knots of Hα emission and bright star clusters. **SF-D**, star formation-diffuse: these sources have diffuse Hα emission, but no obvious stellar cluster in the broad-band optical. **SF-N** star formation-no radio: Region g is a moderately bright Hα shell with no radio counterpart counterpart. **bkgd**, apparent background source: Regions h and i do not have obvious optical counterparts in either the broad-band or Hα imaging. These are assumed to be background quasars,

Region[a]	RA [h:m:s]	Dec [d:m:s]	Flux density[b] [μJy]	α[c]	Type[d]
a	10:10:03.1	+05:20:22.1	80.5 ± 13.7	-0.7 ± 0.3	SF-C
b	10:10:00.7	+05:20:28.4	118 ± 24.5	-0.7 ± 0.3	SF-C
c	10:09:57.4	+05:21:04.9	63.6 ± 16.8	-0.5 ± 0.2	SF-C/D
d	10:09:58.0	+05:19:39.6	139 ± 18.7	-0.2 ± 0.2	SF-C
e	10:10:00.8	+05:19:39.5	15.0 ± 7.8	0.5 ± 0.4	SF-D
f	10:10:01.9	+05:18:42.6	69.4 ± 12.8	-1.3 ± 0.2	SF-D
g	10:10:05.1	+05:19:19.0	———	———	SF-D/N
h	10:10:07.0	+05:18:27.4	60.6 ± 10.8	-0.7 ± 0.3	bkgd
i	10:10:07.3	+05:18:01.6	332 ± 87.4	-1.0 ± 0.1	bkgd?

Table 11: 4-8 GHz radio continuum characteristics of Sextans B regions

[a] Radio continuum sources in Sextans B are labeled in Figure 20b.
[b] Uncertainties given are the flux density rms within the given continuum emission region. The rms of the Sextans B C-band image background for purposes of point source detection is 7.7 μJy.
[c] Spectral power law slope for 4-8 GHz, as output by the CLEAN algorithm.
[d] **SF-C** = star cluster; **SF-D** = diffuse; **SF-N** = no radio continuum; **bkgd** = possible background source. Region type determination is described in Section 4.5.7.

though unresolved supernova remnants at the distance of Sextans B cannot be strictly ruled out with D-configuration data.

4.5.8 SBS 1129+576

Blue compact galaxy SBS 1129+576 is clearly elongated even in ground-based imaging (Figure 21a). *Hubble Space Telescope* images taken from MAST (PI: Prestwich; Prop ID 12018) reveal it to be an edge-on disk, comparable to UGC 4704 (Figure 21b. A small red background galaxy is apparent just east of the disk SBS 1129+576, at coordinates (α, δ) = (11:32:02.76, +57:22:50.5). This position corresponds to IRAC

detection SSTSL2 J113202.85+572250.0 (Capak *et al.*, 2013; Hanish *et al.*, 2015). The clear IRAC and F814W detection plus the complete lack of flux at F606W and F438 suggest that this is an R-band Balmer break dropout galaxy, at redshift $z \sim 1$. This galaxy appears to be associated with the peak of the radio continuum flux, which is also offset slightly from the disk of the nearer galaxy SBS 1129+576. The alpha image output by CLEAN (Figure 21c) gives a spectral index $\alpha = -1.2 \pm 0.2$ for the southern half of the radio continuum source associated with SBS1129+576; the spectral index flattens to $\alpha \sim -0.8$ in the peak associated with the background galaxy. It will be necessary to deblend the flux of a point source at the location of SSTSL2 J113202.85+572250.0 from the extended flux associated with the disk of the foreground galaxy disk.

The background galaxy likewise has problematic implications for infrared detections associated with SBS 1129+576. The main infrared detection comes from IRS observations by Wu *et al.* (2006); while this S/N was insufficient to produce a full IRS spectrum, SBS 1129 detected by the 16 μm and 22 μm peak-up cameras. At the resolution of Spitzer in the mid-IR it is likely this detection is a combination of flux from both SBS 1129+576 and the background galaxy.

Figure 16: HS0822+3542

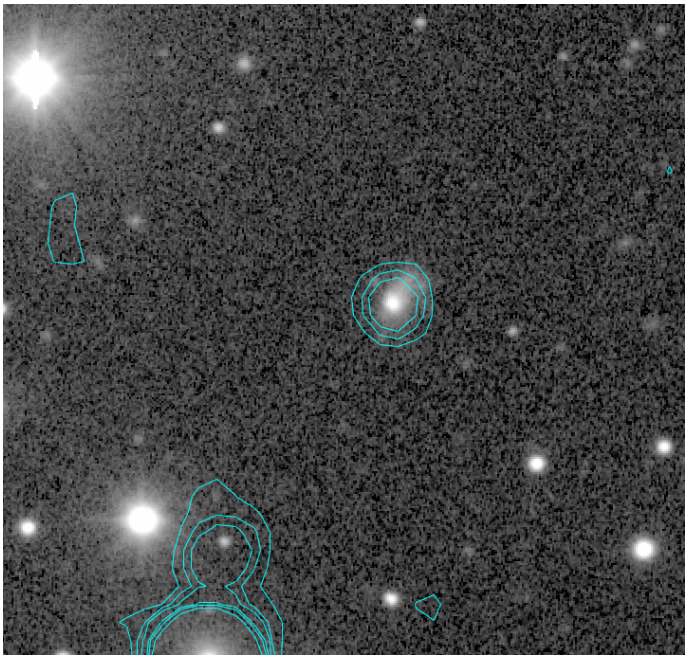

(a) HS 0822+3542 C-band flux density contours. Contours are at 30, 60, 90, 180, 240 and 360 μJy/beam. Underlying image is R-band, from Gil de Paz *et al.* (2003a). While this blue compact dwarf most appears as a point source ground-based imaging, in deeper R-band imaging the compact star-forming region is clearly embedded with a larger, resolved disk.

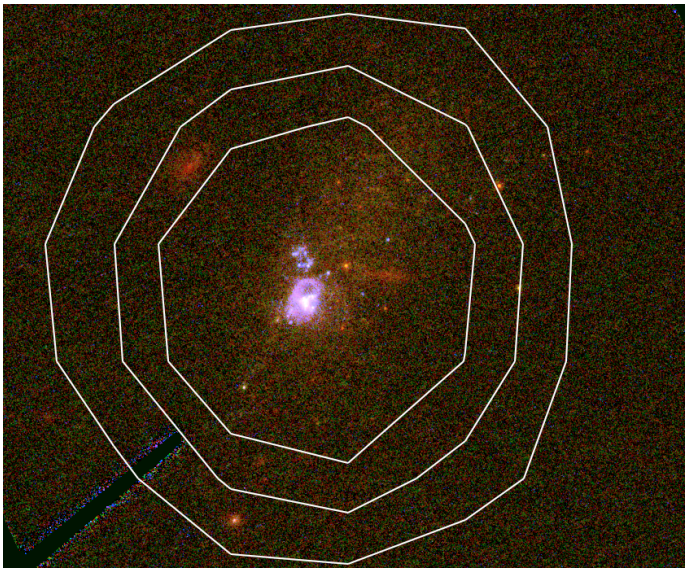

(b) HS 0822+3542 C-band flux density contours, zoomed in and overlaid on the Hubble ACS image from Corbin et al. (Prop ID: 10108). False color RGB assignments are F330W for blue, F550W for green, and F814W for red. C-band contours are identical to Figure 16a. The faint underlying disk of presumed older stars is barely visible in the F814W image. The radio continuum source is centered on the primary star forming region, but the JVLA beam in *D*-configuration covers the entire area of the disk.

Figure 16: HS0822+3542

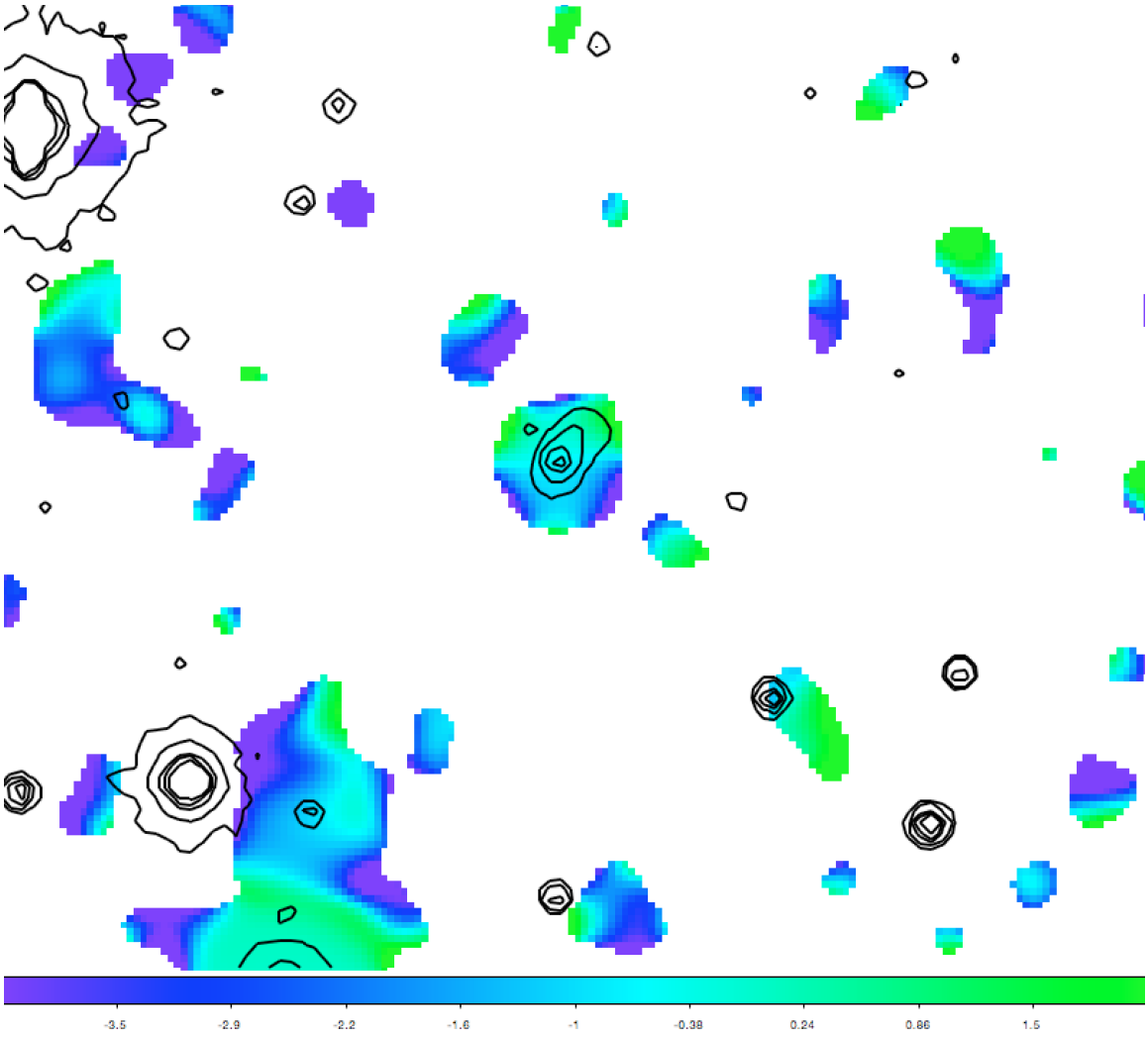

(c) Map of the C-band continuum power law slope α of HS 0822+3542, as output by the CLEAN algorithm. Optical R image contours are from Figure 16a. The continuum detection associated with the blue compact source has a power law slope of $\alpha \sim -0.7 \pm 0.2$. Spectral slope measurements at the edges of point source detections are generally unreliable, due to changing beam resolution with frequency and low S/N, but there is some suggestion of a flattening of the spectral slope over the underlying disk, in the direction northwest of the central point source.

Figure 17: UGC 4704

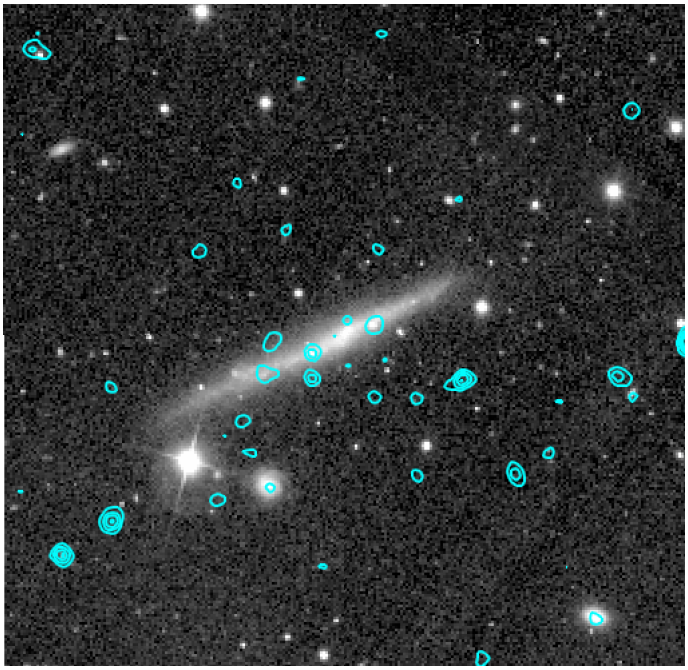

(a) UGC4704 C-band flux density contours. Contours are at 20, 40, 60, 80, and 100 μJy/beam. Underlying image is SDSS g-band.

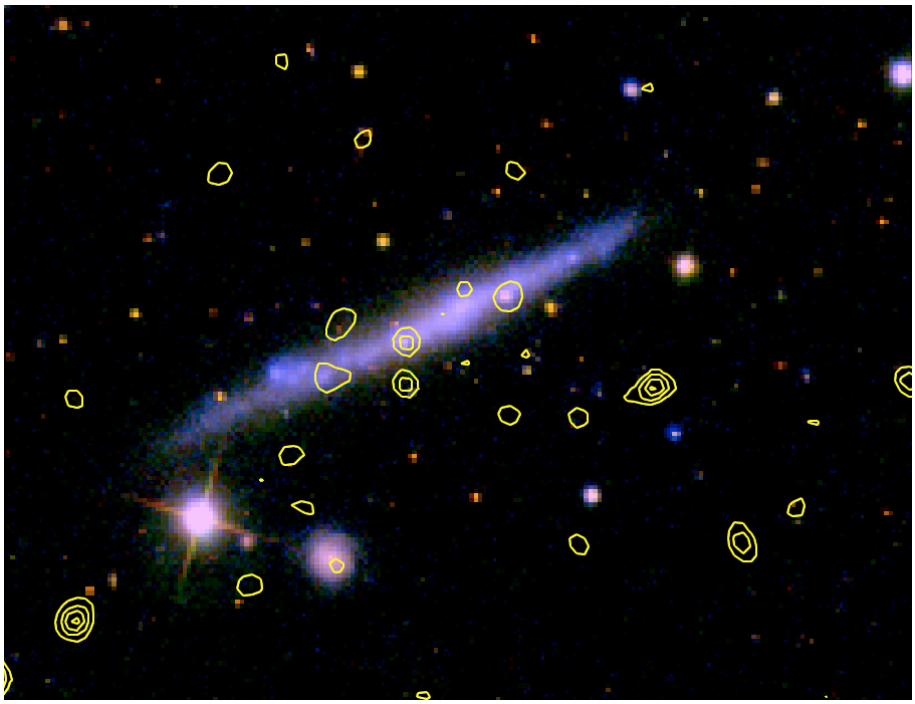

(b) Radio continuum flux density compared with RGB color image of UGC4704. C-band flux density contours are identical to Figure 17a. RGB color assignments are SDSS r for red, g for green, and *GALEX* NUV for blue.

Figure 17: UGC 4704

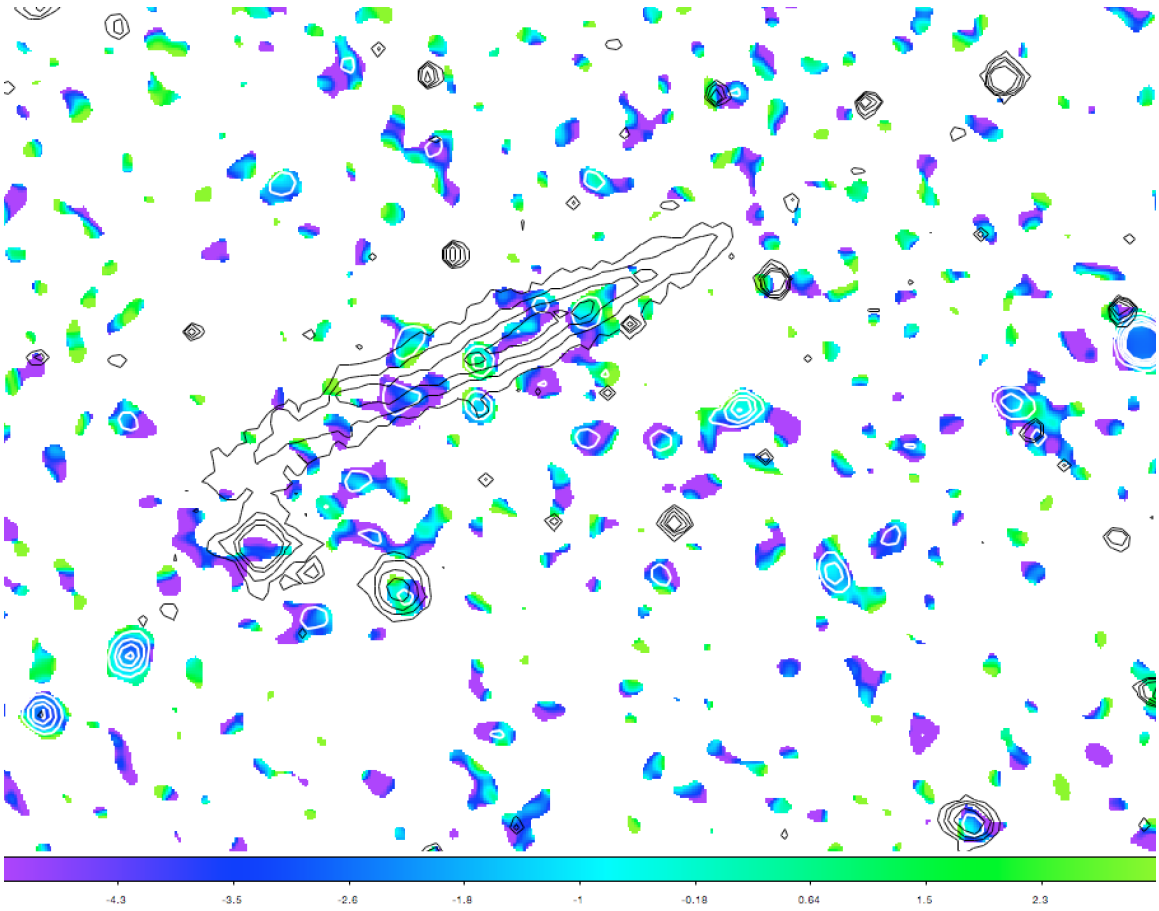

(c) Map of the C-band continuum power law slope α for UGC 4704, as output by the CLEAN algorithm. Black contours are the optical B image. White contours are the C-band flux density contours, and are identical to Figure 17a. Continuum detections associated with star clusters generally have a flatter spectral slope than background point sources.

Figure 18: SBS 0940+544

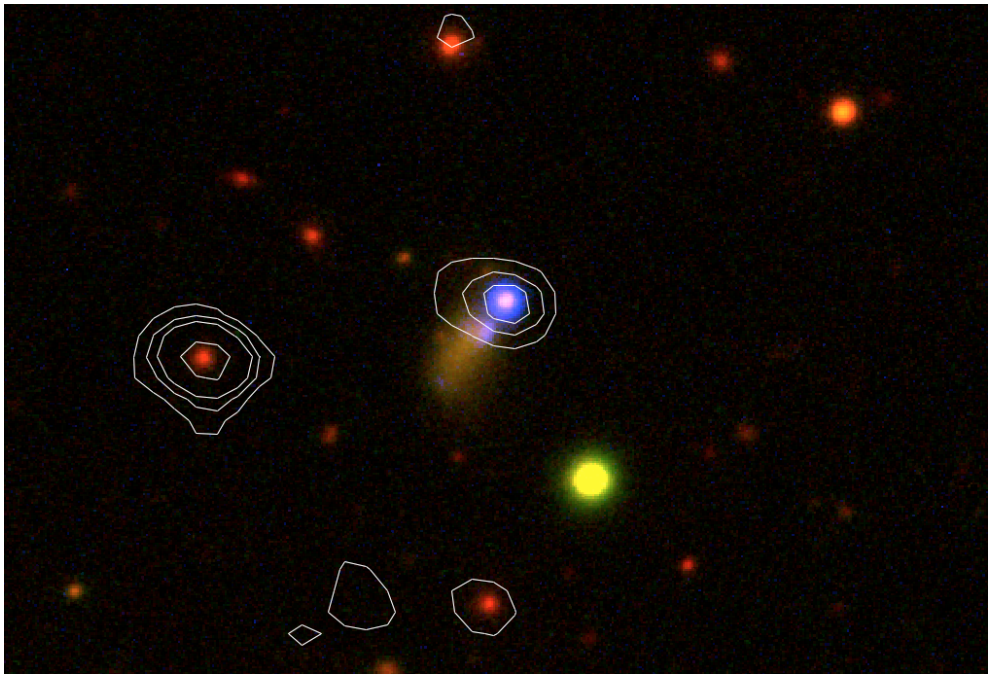

(a) SBS 0940+544 C-band flux density contours. Contours are at 30, 60, 90, 180, and 360, 540μJy/beam. Underlying image is from Gil de Paz *et al.* (2003a), obtained via NED. RGB color assignments are red = R, green = B, blue = Hα. The radio continuum emission is centered on the Hα source, with no apparent emission from the galaxy disk.

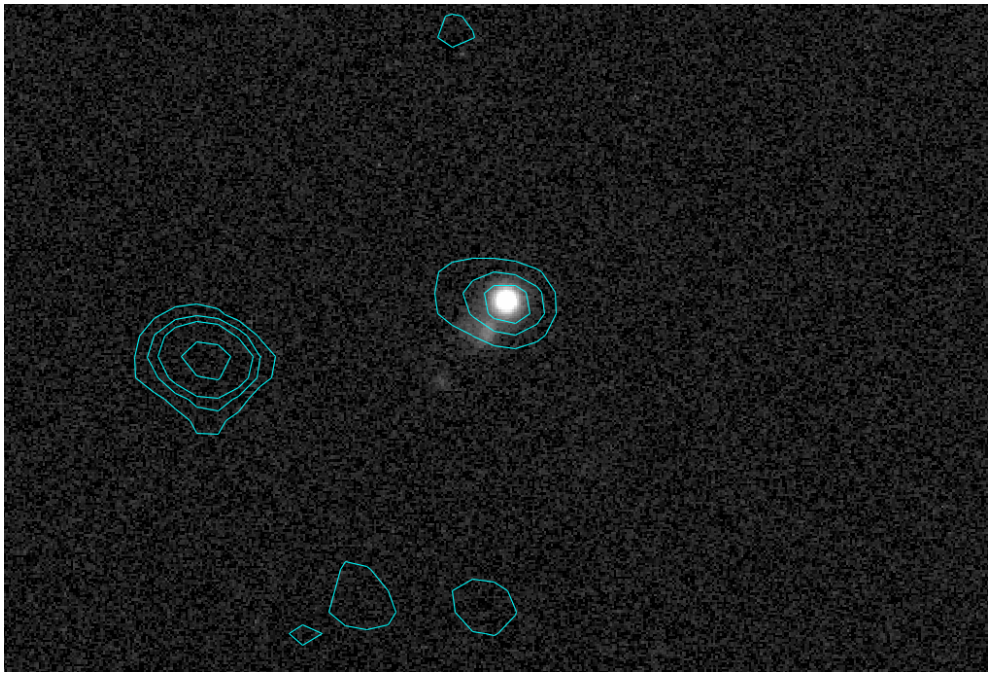

(b) SBS 0940+544 C-band flux density contours. Contours are identical to Figure 18a. Underlying image is Hα from Gil de Paz *et al.* (2003a), obtained via NED.

Figure 18: SBS 0940+544

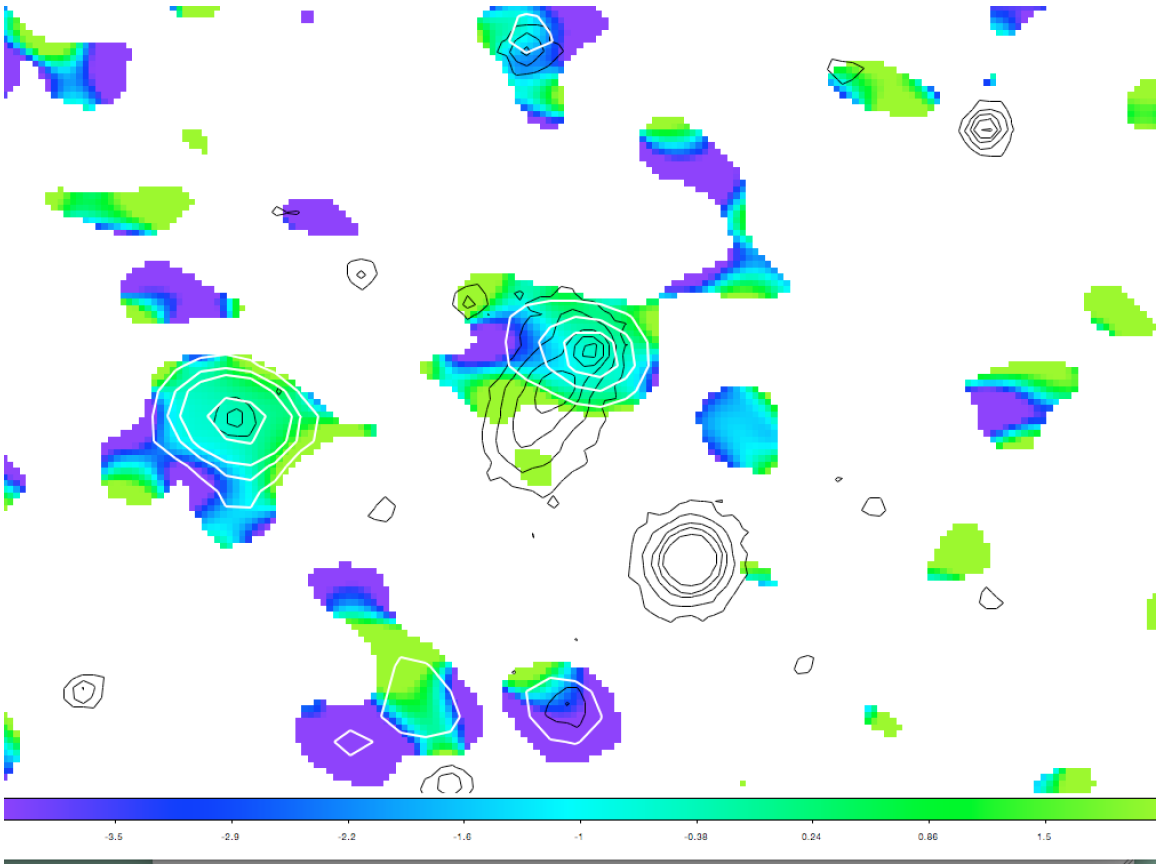

(c) Map of C-band continuum power law slope α of SBS 0940+544, as output by the CLEAN algorithm. Black contours are the optical B band image. White contours are the C-band flux density (see Figure 18a).

Figure 19: Leo A

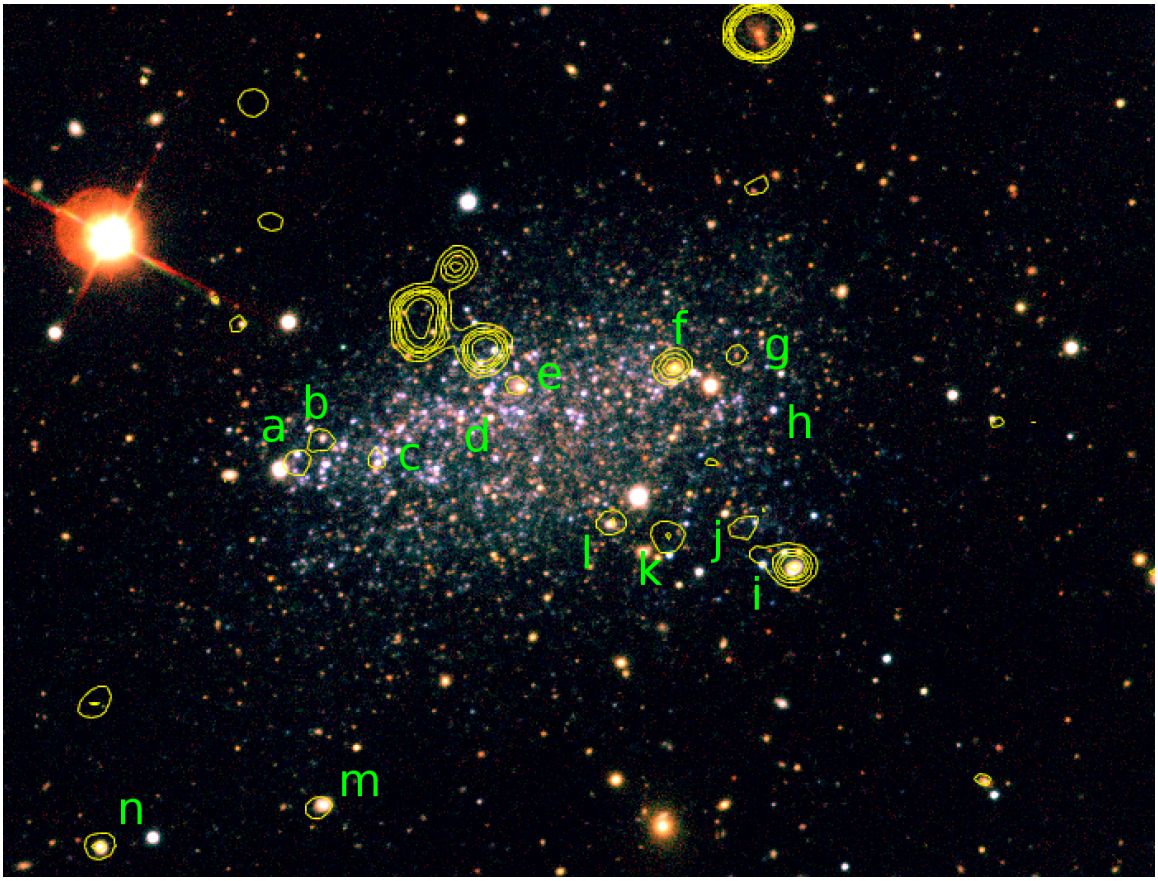

(a) C-band flux density contours for Leo A. Radio continuum contours are at 7.5, 15, 22.5, 30, 45, and 75 μJy/beam. Underlying image is R, V, and B from Cook *et al.* (2014b), obtained via NED. Radio continuum emission from Leo A is extremely faint, localized, and unresolved, and is associated with a handful of optical point sources and diffuse nebulae. Several suspected background sources with no corresponding Hα emission are detected in the Leo A field as reddish optical point sources with associated unresolved radio continuum. The labeled sources are listed in Table 10.

Figure 19: Leo A

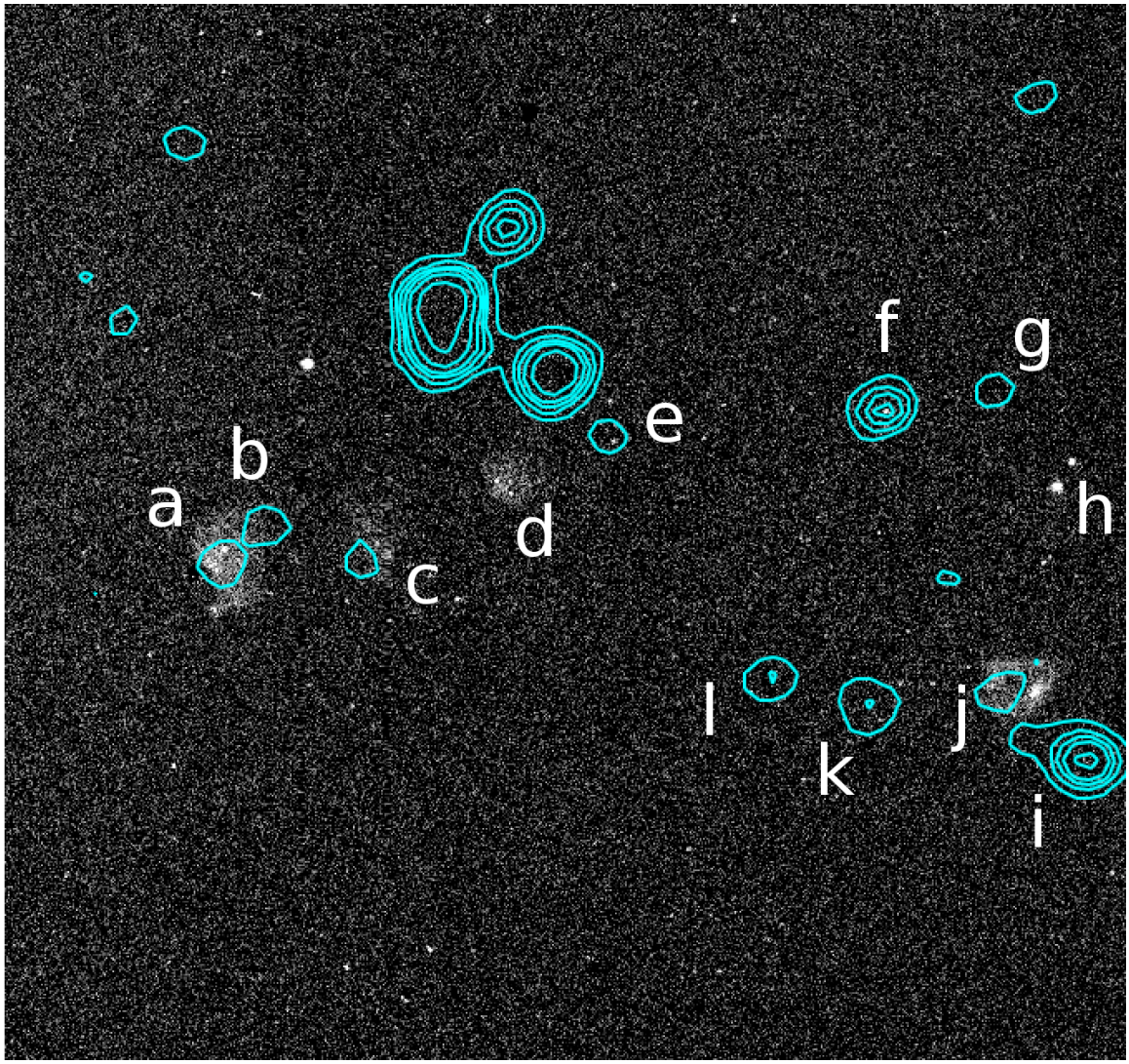

(b) Comparison of C-band radio continuum with Hα emission. Radio continuum contours are identical to Figure 20a. Hα imaging is from Dale *et al.* (2009), obtained via NED. The Hα regions in Leo A are very faint and diffuse, and not clearly associated with star clusters or other optical point sources. The radio continuum is similarly faint, and tends to be associated with Hα regions, though the association is not as strong as in Sextans B. The labeled sources are listed in Table 10.

Figure 19: Leo A

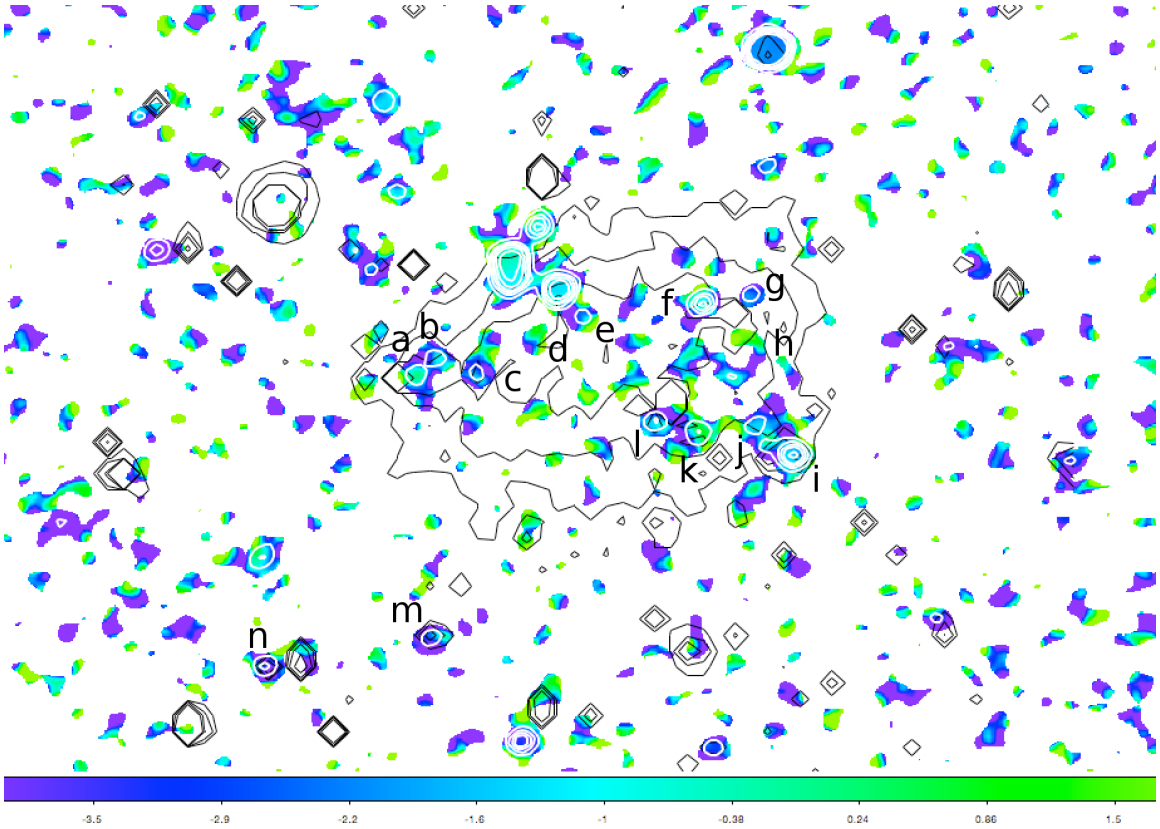

(c) Map of C-band continuum power law slope α of LeoA, as output by the CLEAN algorithm. Black contours are the optical B band image, smoothed with a 10Ǵaussian kernel. White contours are the C-band flux density (see Figure 19a). The properties of the labeled sources are summarized in Table 10.

Figure 20: Sextans B

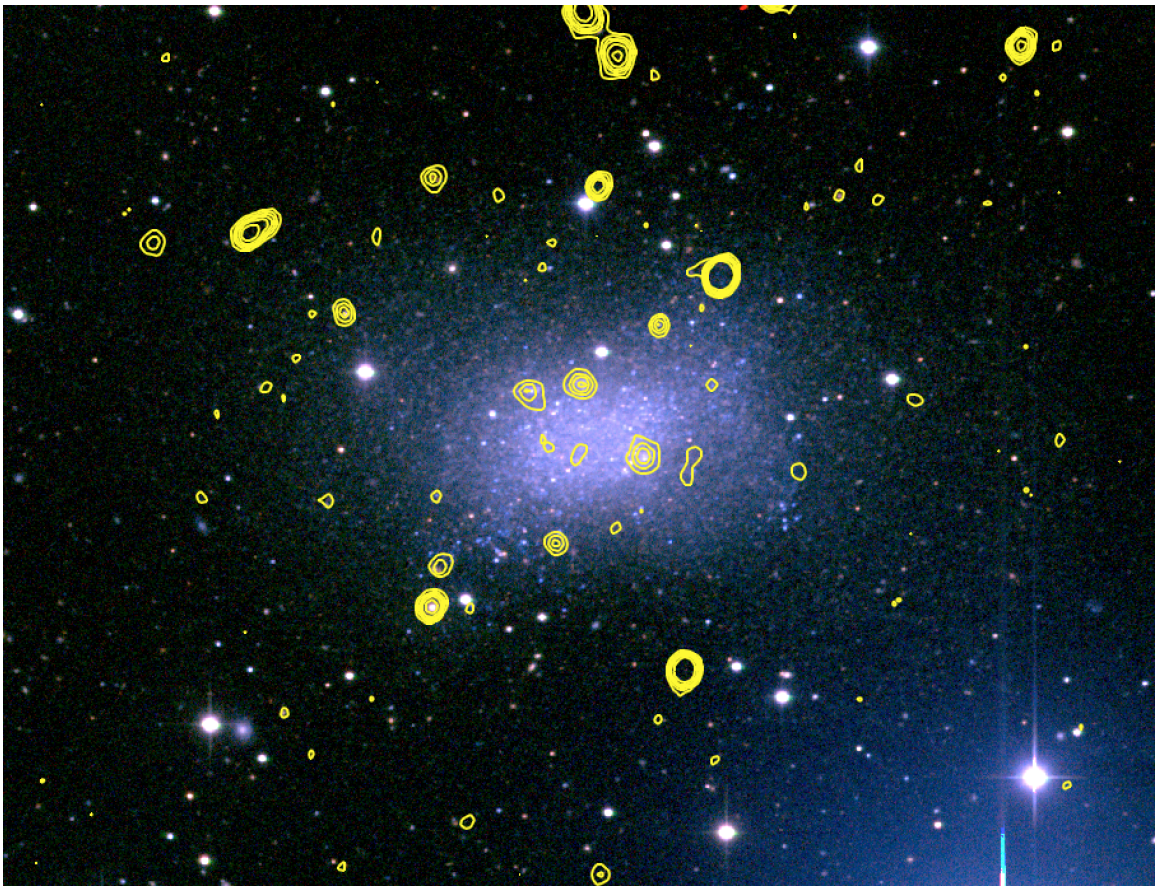

(a) C-band flux density contours for Sextans B. Radio continuum contours are at 10, 20, 30, 40, 60, and 100 μJy/beam. Underlying image is R, V, and B from Cook *et al.* (2014b), obtained via NED. Radio continuum emission from Sextans B is discrete, localized, unresolved, and strongly associated with bright star clusters.

Figure 20: Sextans B

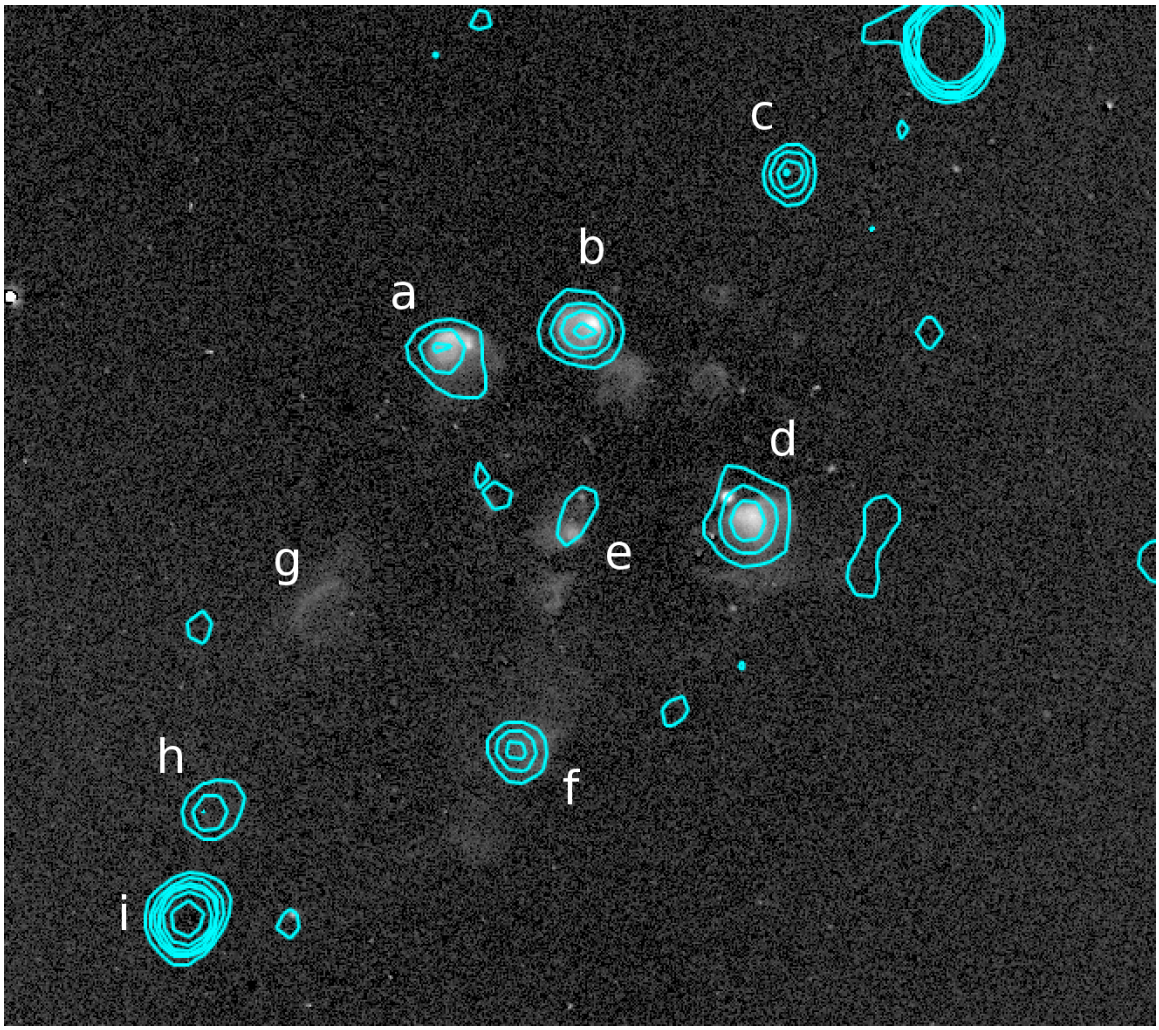

(b) Comparison of C-band radio continuum with Hα emission. Radio continuum contours are identical to Figure 20a. Hα imaging is from Dale *et al.* (2009), obtained via NED. Radio continuum emission is strongly correlated with Hα.

Figure 20: Sextans B

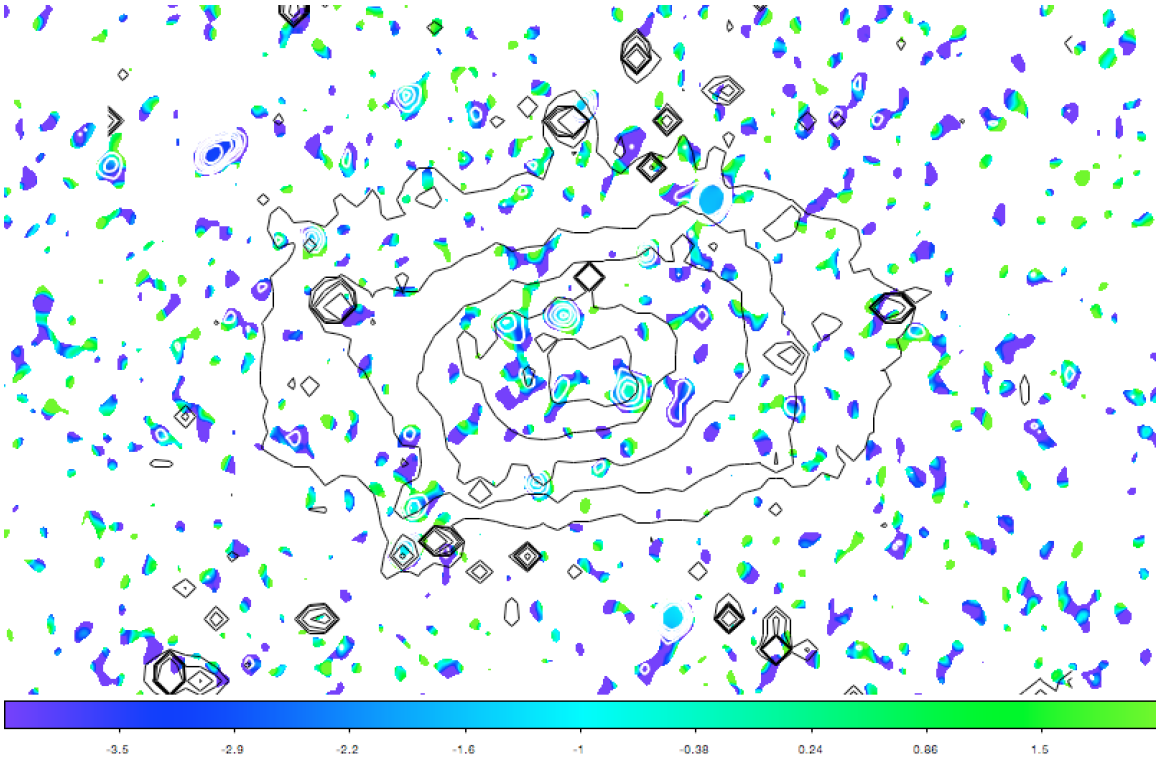

(c) Map of C-band continuum power law slope α of SextansB, as output by the CLEAN algorithm. Black contours are the optical B band image, smoothed with a 10Ǵaussian kernel. White contours are the C-band flux density (see Figure 20a). The continuum sources with clear Hα counterparts have flatter spectral slopes, $\alpha \sim -0.5 \pm 0.3$. Continuum sources without corresponding optical recombination line emission are assumed to be background quasars or galaxies, and generally have $\alpha \sim -1.5$ See Table 11 in the text.

Figure 21: SBS 1129+576

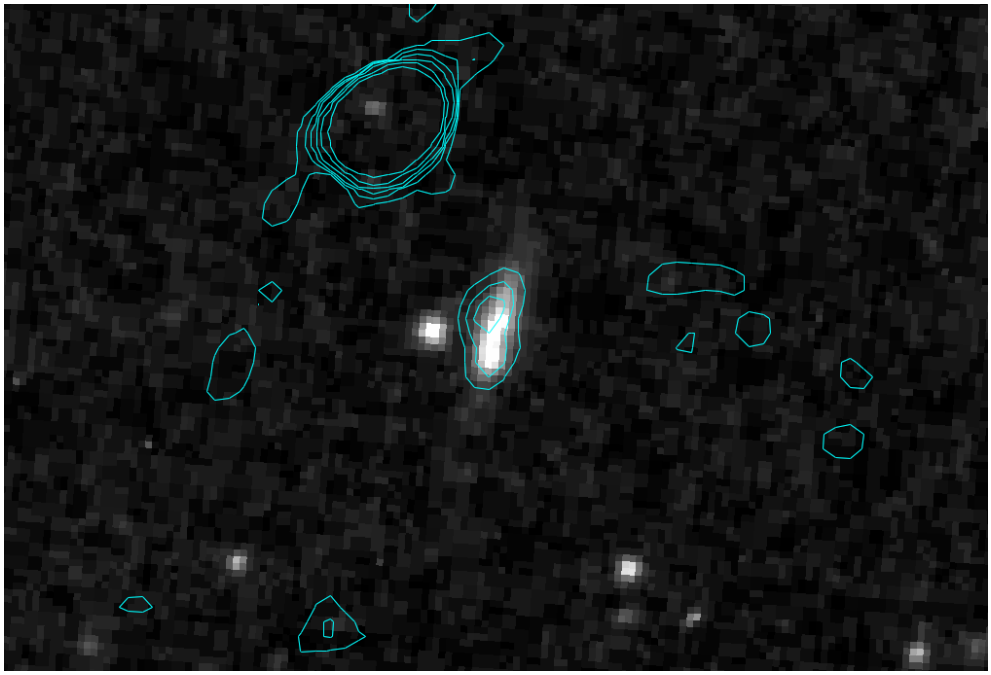

(a) SBS 1129+576 C-band flux density contours. Contours are at 30, 60, 90, 180, and 360, 540μJy/beam. Underlying image is Hα from Gil de Paz *et al.* (2003a), obtained via NED.

Figure 21: SBS SBS 1129+576

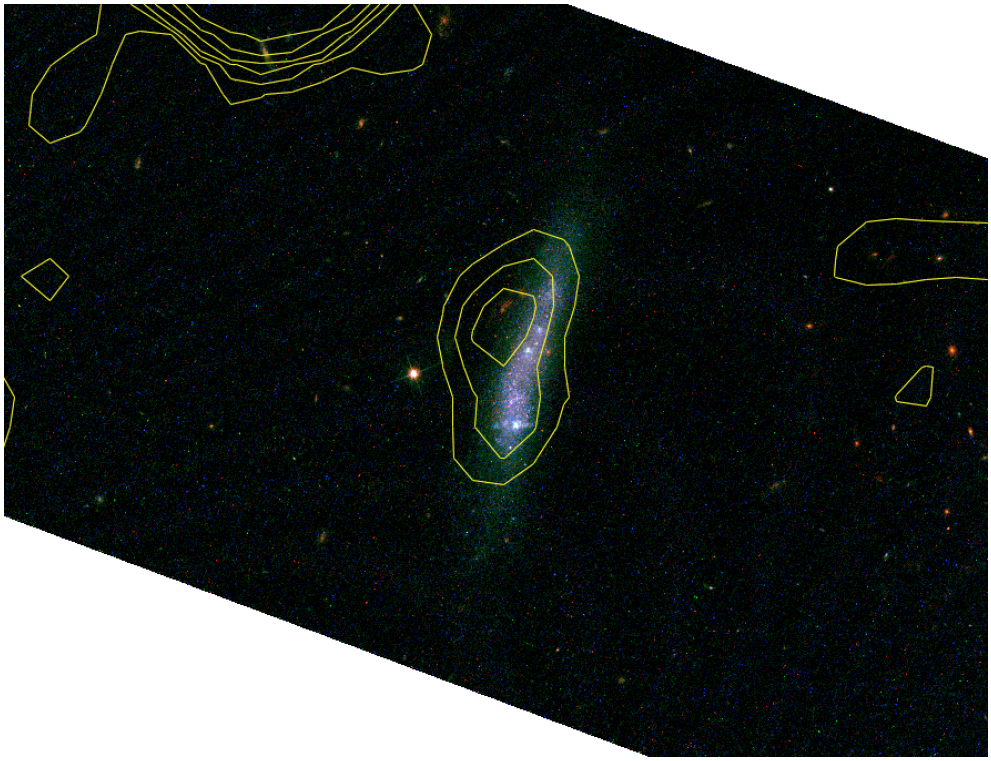

(b) C-band flux density contours overlaid on the HST imaging of SBS 1129+576. Contours are identical to Figure 21a. Underlying HST images obtained from MAST (PI: Prestwich; Prop ID: 12081). RGB color assignments are red = $F814W$, green = $F606W$, blue = $F438W$. The higher resolution of HST reveals a small red background galaxy just to the east of the SBS 1129+476 galaxy disk, associated with the peak of the continuum flux. The HST images have not been cleaned of cosmic rays.

Figure 21: SBS SBS 1129+576

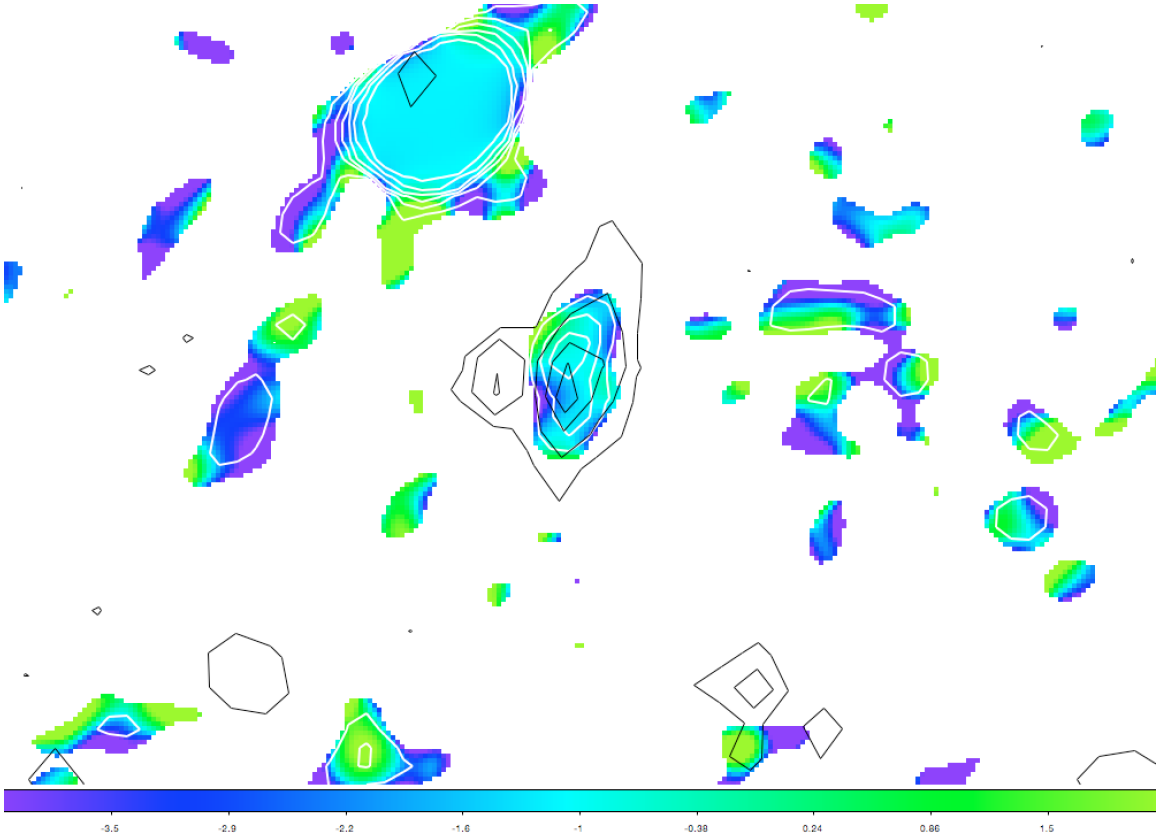

(c) Map of C-band continuum power law slope α of SBS 1129+576, as output by the CLEAN algorithm. Black contours are the optical B band image. White contours are the C-band flux density (see Figure 21a).

4.5.9 SBS 1415+437

SBS 1415+437 is a blue compact galaxy which has previously been observed by Gil de Paz *et al.* (2003a), and which has been targeted by several HST imaging campaigns, including some snapshot narrow-band Hα and [OIII] emission line observations with the ACS $F458N$ narrow filter and the $FR505N$ ramp filter (PI: Aloisi; Prop ID: 9361).

SBS 1415+437 was also included in the observations of Wu *et al.* (2008). They detect this galaxy in both the infrared with MIPS and in the L-band.

As with SBS 0940+544, this galaxy has a very asymmetrical appearance, with a luminous star-forming Hα region offset to the southwest of the fainter disk of old stars. C-band radio continuum is entirely associated with this burst of star formation, even though there are smattering of fainter, diffuse Hα scattered throughout the rest of the galaxy disk.

Figure 22: SBS 1415+437

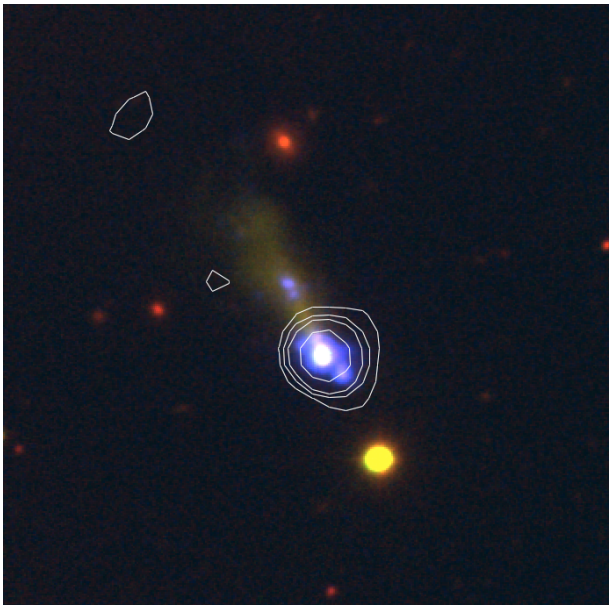

(a) SBS 1129+576 C-band flux density contours. Contours are at 30, 60, 90, 180, and 360, 540μJy/beam. Underlying image is Hα from Gil de Paz *et al.* (2003a), obtained via NED. RGB color assignments are red = R, green = B, blue = Hα. While there are smatterings of Hα emission visible in the northern parts of the disk, the radio continuum flux is entirely associated with the bright star forming knot at the southern end of the galaxy.

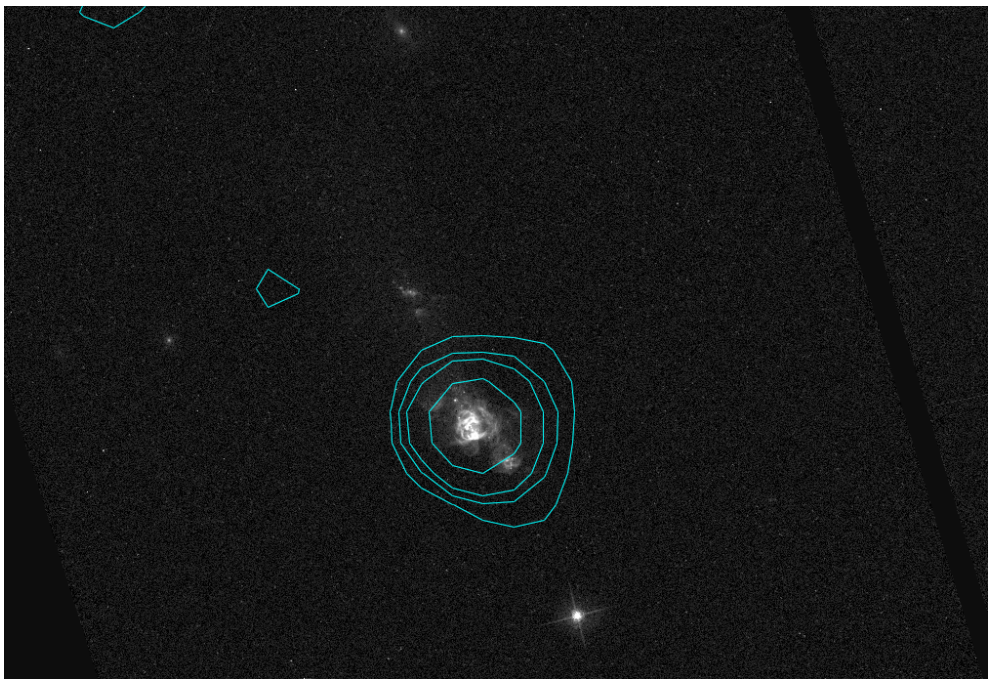

(b) C-band flux density contours overlaid on a higher resolution $F458N$ (Hα) image of SBS 1415+437. Contours are identical to Figure 22a. Underlying HST ACS/WFC image obtained from MAST (PI: Aloisi; Prop ID: 9361).

Figure 22: SBS SBS 1415+437

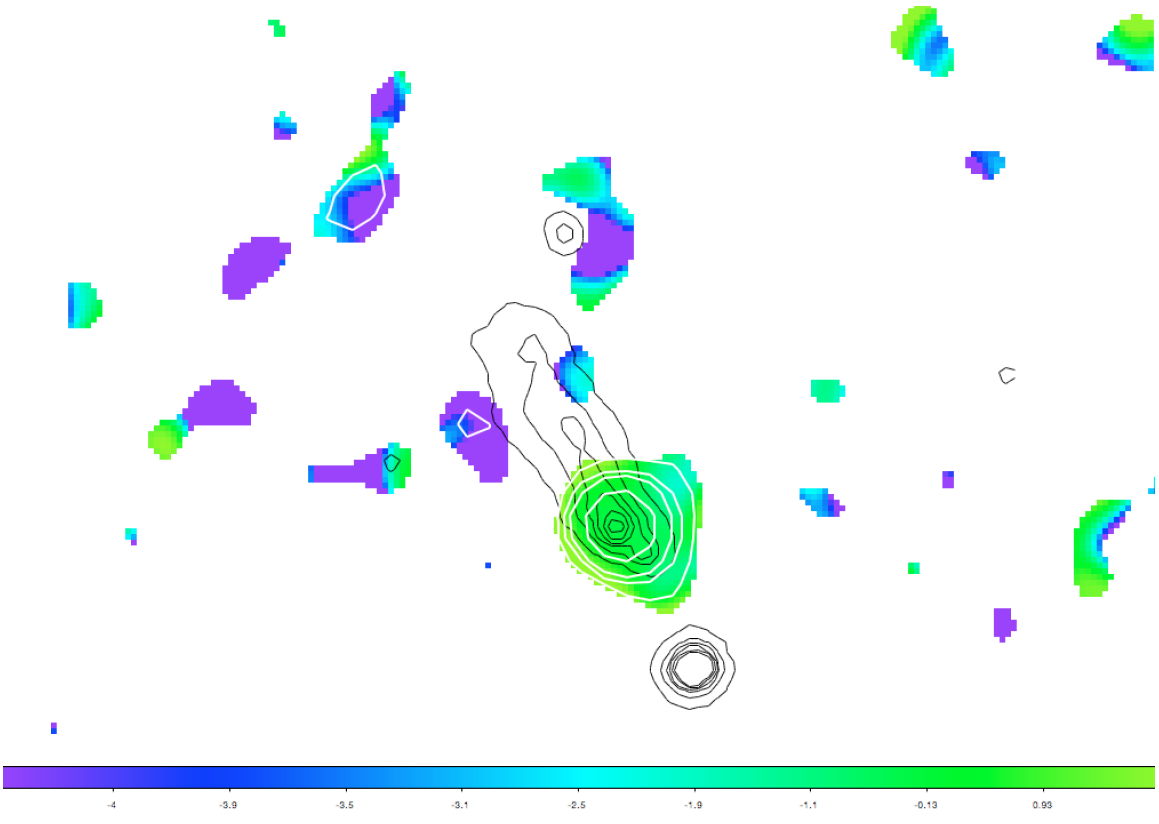

(c) Map of C-band continuum power law slope α of SBS 1415+437, as output by the CLEAN algorithm. Black contours are the optical B band image from Figure 22a. White contours are identical to the C-band flux density contours in that image.

Table 12: Radio and Infrared fluxes of low metallicity sample.

Galaxy	12+(O/H)	24 μm flux[a] [Jy]	70 μm flux[a] [Jy]	C-band flux[b] [Jy]	4.8 GHz flux[c] [Jy]	α	Refs
II Zw 40	8.06	1.60E0 ± 3.0E-2	5.58E0 ± 2.8E-1	2.30E-2 ± 1.3E-5	2.45E-2 ± 3.2E-5	-0.21	2
HS 0822+3542	7.40	4.02E-3 ± 1.8E-4	4.05E-2 ± 5.6E-3	1.68E-4 ± 6.2E-5	1.59E-4 ± 8.3E-5	-0.32	2
UGC 4704		1.05E-2 ± 1.2E-3	1.35E-1 ± 2.2E-2	2.75E-4 ± 1.2E-5	1.85E-4 ± 2.8E-5	0.04	1
I Zw 18	7.17	6.29E-3 ± 2.3E-4	3.49E-2 ± 4.8E-3	1.33E-3 ± 1.7E-5	1.34E-3 ± 4.5E-5	-0.10	2
SBS 0940+544	7.48	2.13E-3 ± 8.5E-5	–	1.26E-4 ± 1.2E-5	7.82E-5 ± 3.7E-5	-0.20	3
Leo A	7.38	<1.08E-2	1.75E-1 ± 5.0E-2	3.74E-4 ± 8.8E-6	3.52E-4 ± 2.1E-5	-1.20	5
Sextans B	7.53	2.10E-2 ± 2.4E-3	1.21E-1 ± 2.9E-2	6.62E-4 ± 7.7E-6	7.42E-4 ± 1.6E-5	-0.70	1
Sextans A	7.54	3.78E-2 ± 4.2E-3	7.32E-1 ± 9.4E-2	2.28E-3 ± 1.2E-5	2.05E-3 ± 2.8E-5	-1.40	1
SBS 1129+576	7.42	1.40E-3[d] ± 1.0E-4	–	1.27E-4 ± 1.8E-5	1.28E-4 ± 4.1E-5	-0.90	4
SBS 1415+437	7.59	1.96E-2 ± 8.4E-5	–	6.72E-4 ± 2.0E-5	6.96E-4 ± 5.6E-5	-0.13	3

[a] MIPS 24 μm and 70 μm fluxes.
[b] C-band: 4.8 - 7.2 GHz flux, $\bar{\nu} = 6.0$ GHz. See Table 6.
[c] Spectral window 12 only, $\bar{\nu} = 4.86$ GHz. See Table 6.
[d] 22 μm flux, from the IRS pop-up camera Wu *et al.* (2006). No error is estimated with this measurement, but Wu et al. assign an upper limit of 0.1 mJy to their undetected sources, so I use this as their uncertainty.

References: *Infrared fluxes from:* (1) Dale *et al.* (2009); (2) Engelbracht *et al.* (2008); (3) Wu *et al.* (2008); (4) Wu *et al.* (2006); (5) P. Cigan, private communication.

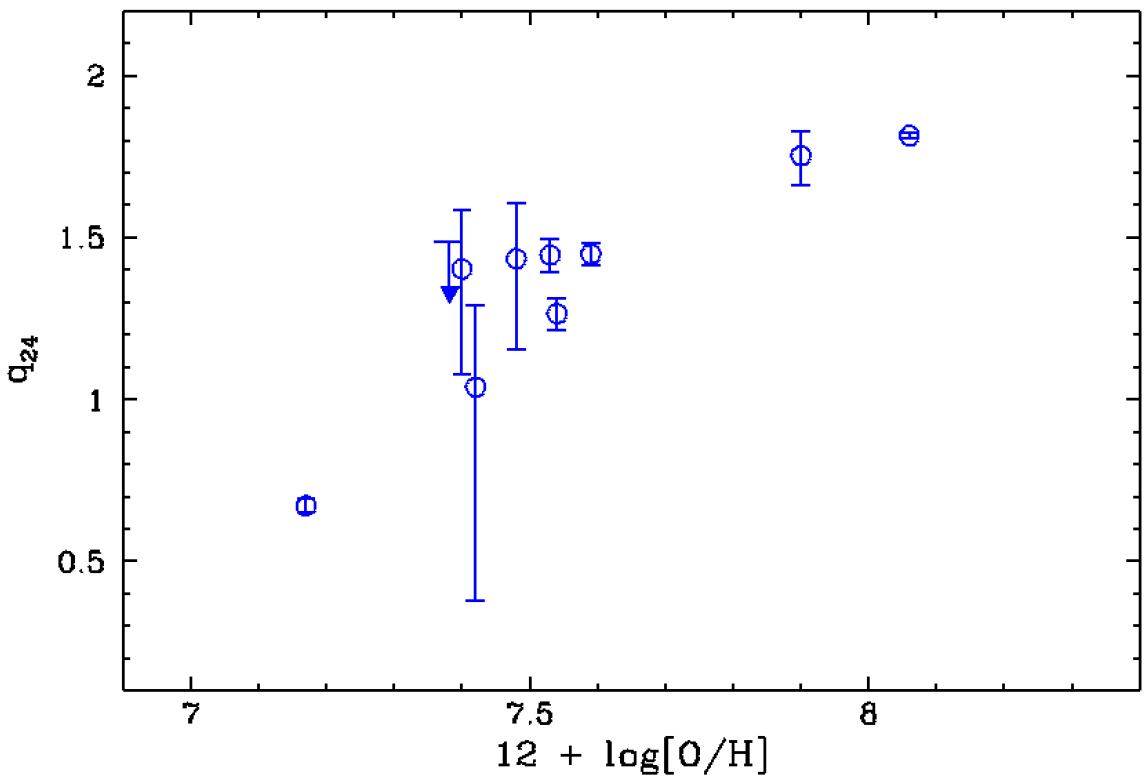

Figure 23: The infrared/radio continuum emission ratio q_{24-C} as a function of nebular oxygen abundance. Blue open circles are the XMD/low metallicity sample from this work. Note that Leo A is an upper limit, due to a non-detection at 24 μm. (Leo A has been detected at 70 μm and longward by both MIPS and the PACS instrument on *Herschel* (P. Cigan, private communication).

4.6 Integrated C-band Properties and the Radio/IR Relationship

In Table 12 I summarize the total radio continuum properties for all of the galaxies in my low-metallicity dwarf sample. The C-band fluxes are from this work, and include all usable spectral windows between 4-8 GHz. For galaxies which are resolved into multiple distinct continuum sources, I include the flux contributions from all diffuse and compact sources with Hα counterparts that are not associated with any known

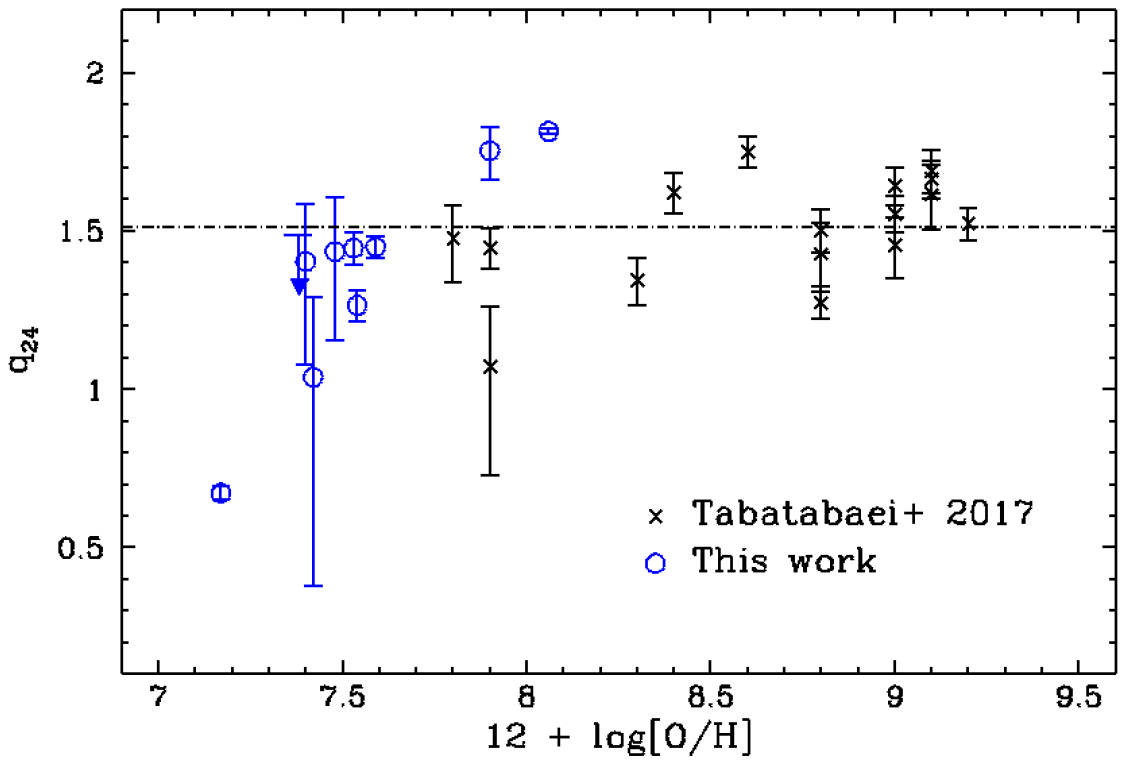

Figure 24: The infrared/radio continuum emission ratio q_{24-C} as a function of nebular oxygen abundance. Black crosses are 4.8GHz radio continuum measurements of LVL/KINGFISHER galaxies from Tabatabaei *et al.* (2017), cross-correlated with MIPS 24 μm measurements from Dale *et al.* (2009) and metallicity estimates from Cook *et al.* (2014a). The dashed line represents the mean q_{24-C} value of the KINGFISHER galaxies. Blue open circles are the XMD/low metallicity sample. The XMDs are all below the mean q_{24-C} value of the normal galaxies.

background sources. In these cases, the total fluxes were obtained by masking the pixels to be included within the CASA viewer environment and outputting the region statistics. These were compared with the simple summation of the fluxes from the included regions (as given in the preceding tables), and were found to be in good agreement.

The spectral index α listed with each galaxy is also determined from the CASA statistics output for C-band. As discussed in Section 4.5.1, some care is necessary when extracting the spectral index from a wide band continuum observation, because

the angular size of the interferometric beam varies by almost a factor of 2 over the bandpass. CASA does include a correction for this effect, but generally the measured α at the edges of a discrete detection are unstable and unreliable, as can be seen in e.g. Figure 18c and Figure 21c. CASA's statistical output of α is weighted towards regions of higher flux and therefore greater statistical reliability. For three galaxies (Sextans A, Sextans B, and II Zw 40), I do have multiple bandpasses, making it possible to fit α over a wider frequency range; generally the C-band α output by CASA is within the errors of these fits. Note that the beam size mismatch is even greater between L-band and C-band (see Chapter 3). Most of the XMDs have spectral indices that are flatter than that of the Milky Way ($\alpha = -0.7$) or of other "normal" star-forming galaxies in the nearby universe. This is consistent with prior observations of I Zw 18 by Hunt *et al.* (2005b) and SBS 0335-052E by Hunt *et al.* (2004), and suggests that the bulk of the radio continuum in these galaxies is from thermal free-free emission rather than synchrotron. Without better multi-band observations of these galaxies, it is impossible to separate the thermal and non-thermal components cleanly, and so I do not attempt to calculate magnetic fields for these objects (as I did for Sextans A in Chapter 3).

In addition to the total C-band fluxes, which include all usuable spectral windows between 4-8, I have also separately split, imaged, and CLEANed the 4.8 GHz flux window. This facilitates comparison with archival datasets of normal-metallicity galaxies, which typically have much smaller C-band bandpasses of $\Delta\nu \sim 100$ MHz centered on the 4.8 GHZ spectral window.

This particular sample of galaxies was selected for availability of archival infrared data, in order to facilitate the measurement of the radio/IR correlation. *Spitzer* MIPS

24 μm and 70 μm fluxes are listed for all galaxies, except for SBS 1129+576, which has a 22 μm measurement from the IRS instrument.

4.6.1 Best Indicator of Dust Mass

When studying the radio/IR relationship, does it make the most sense to compare the radio continuum to mid-infrared flux, far-infrared flux, or a combined "bolometric" estimate such as TIR(5-1000μm)? The exact choice of infrared emission measure varies from reference to reference, typically according to the data available for the specific sample. The original reports of a tight radio/IR correlation from van der Kruit (1971, 1973) used 10 μm observations of galaxies (with and without active nuclei) from Kleinmann and Low (1970b,a). Several modern sources use multi-wavelength estimates of the total bolometric infrared luminosity, though other authors use monochromatic infrared measures.

There are many technical and theoretical consideration when choosing an infrared star formation indicator. In principle, mid-infrared flux should be a better tracer of current star formation, because the warm and hot dust will be more strongly associated with high mass stars. But old stars can also heat dust: far-infrared and bolometric luminosities will include the contribution from the cold dust associated with evolved populations, and may not accurately reflect the *current* epoch of star formation.

For this study, the decision is based on data availability. Particularly for faint sources, mid-infrared 20 μ *IRAS* and 24 μm *Spitzer* data may be available when longer wavelength measurements are not, due to the greater sensitivity of current mid-infrared detectors. In recent years, the *WISE* satellite has provided 22 μm measures for a

number of sources. Several of my galaxies lack far-infrared detections longward of 60 μm, but most of them have 24 μm MIPS detections. Of the two galaxies that don't have 24 μm detections, SBS 1129+576 has a 22 μm detection from the IRS red peak-up camera. Leo A is a true non-detection at this wavelength, but has numerous near- and far-infrared detections from IRAC, MIPS and the *Herschel* mission (P. Cigan, private communication). This means that Leo A's 24 μm flux is fairly well bracketed, and can be inferred from SED fitting.

4.6.2 The Radio/IR Relationship in Extremely Metal-Deficient Environments

The radio-infrared relation is most often characterized by the q-parameter, which is essentially the ratio of the infrared luminosity and the radio luminosity. For bolometric measures such as FIR, this often takes on a slightly more complicated form, e.g.:

$$q_{FIR} = \frac{1.26 \times 10^{14} \, (2.58 \, S_{60\mu m} + S_{100\mu m})}{3.75 \times 10^{12} F_{1.4GHz}} \tag{4.7}$$

The measured C-band flux densities for my low-metallicity dwarf sample are listed in Table 12 alongside the MIPS 24 μm and 70 μm infrared fluxes. All of the galaxies in my sample have 4-8 GHz C-band radio continuum, while only three (Sextans A, Sextans B, and Leo A) have 1-2 GHz L-band data, so I conduct my initial analysis of the radio/IR relation using the higher frequency C-band data. Most existing C-band radio continuum surveys have used narrower bandpasses centered around a mean frequency of $\bar{\nu} \sim 4.8 - 4.9$ GHz. My wider-band data has a mean frequency $\bar{\nu} = 6.0$ GHz– in order to compare with dataset for higher-metallicity galaxies, I will need to estimate the 4.8 GHz flux density. My dataset has sufficient S/N to allow me to split off the 100 MHz spectral window centered on 4.8 GHz, re-image, and CLEAN.

The other option would be to extrapolate using the estimated spectral index α. Both methods yield similar flux estimates for 4.8 GHz, with comparable uncertainties.

I plot the calculated q_{24-C} ratio as a function of nebular oxygen abundance in Figures 23 and 24. For a high-metallicity comparison sample, I use the 4.8 GHz *JVLA* observations of the KINGFISHER sample, by Tabatabaei *et al.* (2017). I obtain MIPS 24 μm fluxes for the KINGFISHER galaxies by cross-correlating the Tabatabaei et al. sample with the Dale *et al.* (2009) LVL sample; the metallicities come from Cook *et al.* (2014b) and Moustakas *et al.* (2010).

In Chapter 1, I showed the tentative evidence for a deficit in q_{24-L} (the 1.4 GHz radio/IR measure) for a sample of blue compact dwarfs from Wu *et al.* (2008). I only have 1.4 GHz observations for 3 of my XMD dwarf galaxies: Sextans A, Sextans B, and II Zw 40. For the rest of the sample, I use the C-band spectral index α output by the multi-frequency CLEAN algorithm to extrapolate the 1.4 GHz fluxes and errors. The comparison between my XMDs and the Wu et al. BCDs is plotted in Figure 25.

Finally, it is necessary to ask the questions that opened this chapter: does the calorimeter model of the radio/IR correlation break as expected at low luminosities? And does metallicity play a role? Is there a "conspiracy" at low luminosities, such that breakdowns between the UV-to-infrared conversion and supernova-energy-to-radio-synchrotron conversion happen in parallel, in such a way to preserve the radio/IR relation despite the overall collapse of the calorimeter model?

To determine the answers, in Figure 26 I plot the ratio of the infrared and radio continuum fluxes to the integrated Hα fluxes of the XMD dwarf galaxies, as a function of metallicity. Here I am treating Hα as a best available proxy for the overall star

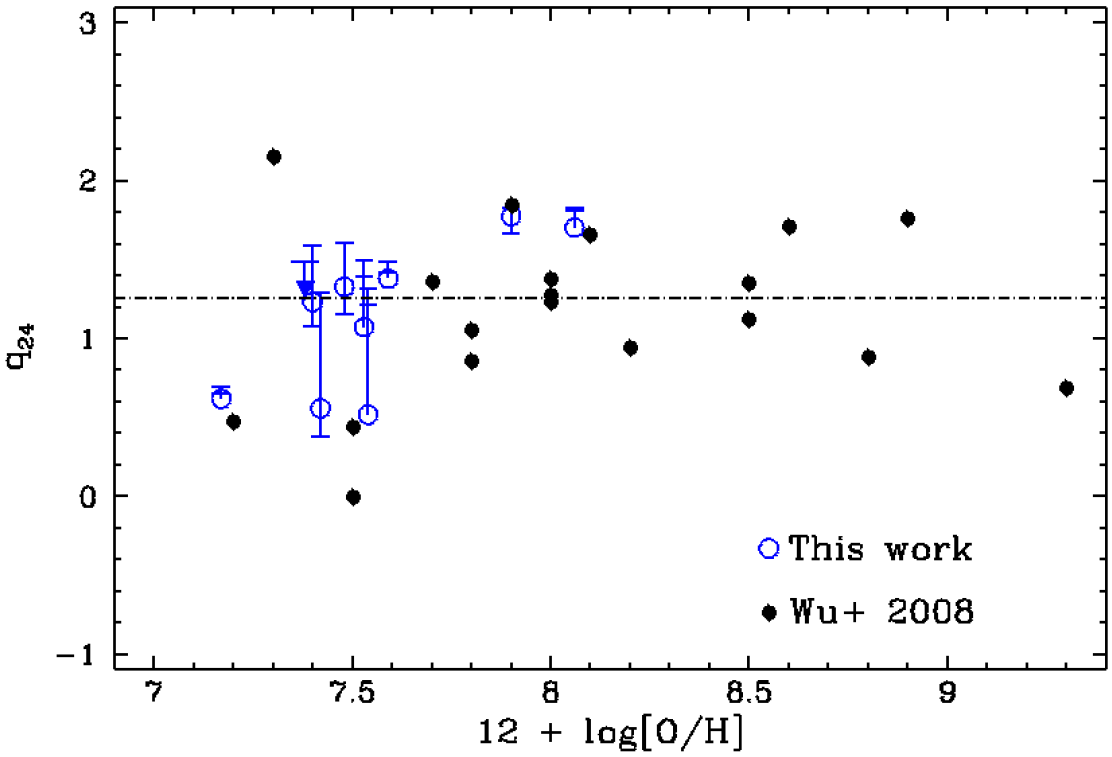

Figure 25: The 1.4 GHz infrared/radio continuum emission ratio q_{24-L} as a function of nebular oxygen abundance. L-band measurements were available for Sextans A, Sextans B, and II Zw 40; for the rest of the sample, they were extrapolated from the C-band spectral index. Filled black circles are the 1.4GHz radio continuum measurements for the BCD sample from Wu *et al.* (2008). The dashed line represents the mean q_{24-L} value of the Wu et al. galaxies. Blue open circles are the XMD/low metallicity sample.

formation rate. Various caveats to this assumption are discussed in Chapter 1, but overall Hα is the safest choice. Hα fluxes come from Lee *et al.* (2009a) for dwarfs included in the 11HUGS/LVL sample, and from Gil de Paz *et al.* (2003b) for the more distant blue compact dwarfs.

The offset between 24μm/Hα (blue dots) vs 4.8 GHz/Hα (red squares) in Figure 26 is identical to the value of q_{24-C} for each object in Figure 24. It is a little dangerous to draw conclusions from sparse sampling such as this, but in generally speaking, the ratio of mid-infrared to Hα appears decline steadily at lower metallicity, while the

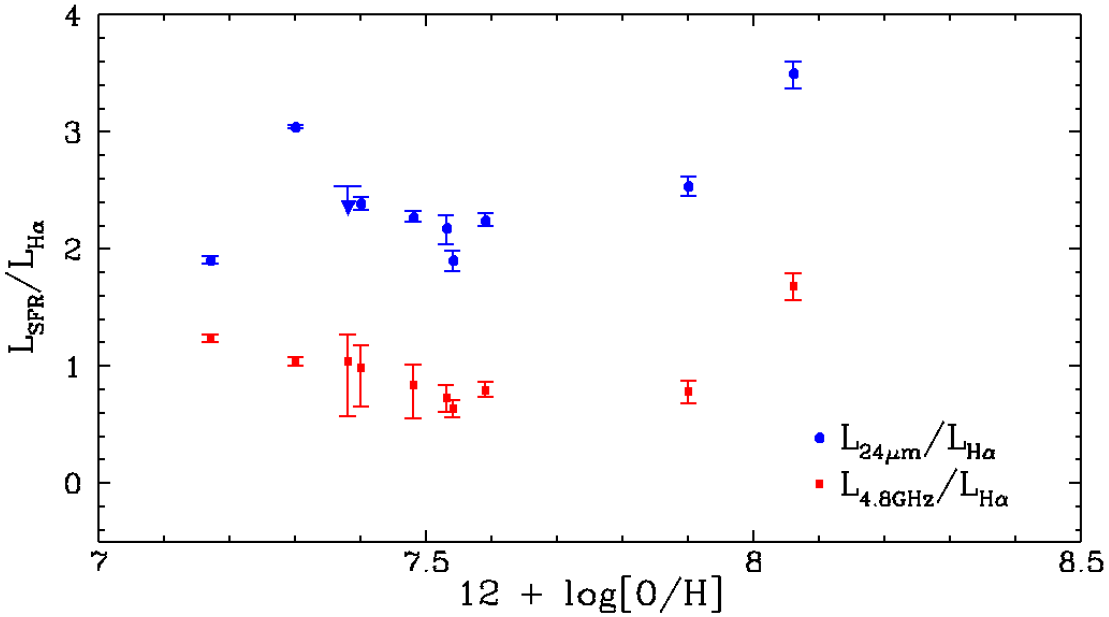

Figure 26: The ratio of 24μm/Hα (blue dots) vs 4.8 GHz/Hα (red squares) as a function of metallicity for the XMD sample. The offset between the two relations is real, and reflects the mean value of q_{24-C} (see Figure 24. While the ratio of mid-infrared to Hα generally declines at lower metallicity, the ratio of radio continuum to Hα appears to plateau and even rise slightly below $12 + (O/H) < 8.0$.

ratio of radio continuum to Hα plateaus or even rises slightly below $12 + (O/H) < 8.0$. These ratios are plotted separately in Figures 27a and 27b, with normal-metallicity galaxies from the KINGFISHER dataset for comparison. Both the infrared and the radio continuum ratios are reduced from the high-metallicity mean by a factor of $\sim$ 10, indicating the calorimeter model has broken down in exactly the way expected. However, while the infrared-to-Hα ratio appears to decline at metallicities below $12 + (O/H) < 8.0$, perhaps suggesting a continuous depletion of dust extreme metallicities, the radio continuum-to-Hα ratio stabilizes or even start to return to the higher metallicity mean. If these suggested trends were real, they could be consistent

with the interpretation that the bulk of the radio continuum at these metallicities is thermal free-free emission, which is directly tied to the ionized gas and the Hα.

Figure 27: Ratios of infrared and radio star formation indicators to Hα flux, for XMDs vs. KINGFISHER galaxies

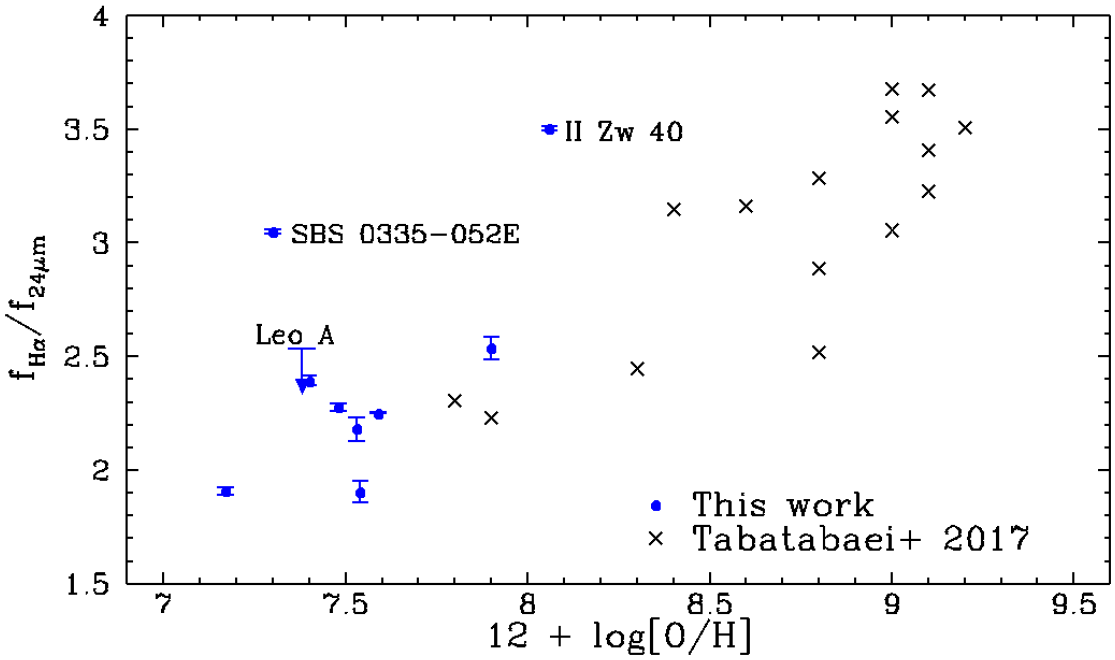

(a) Ratio of 24μm to Hα flux as a function of nebular oxygen abundance, for my low- and high-metallicity dwarf galaxies. Blue filled circles are my XMD sample. Black crosses are the LVL/KINGFISHER nearby dwarf sample of Tabatabaei *et al.* (2017). Leo A is marked as a upper limit. The ratio of 24μm/Hα is generally below that of the higher metallicity galaxies, and continues to decline below $12 + (O/H) < 8.0$

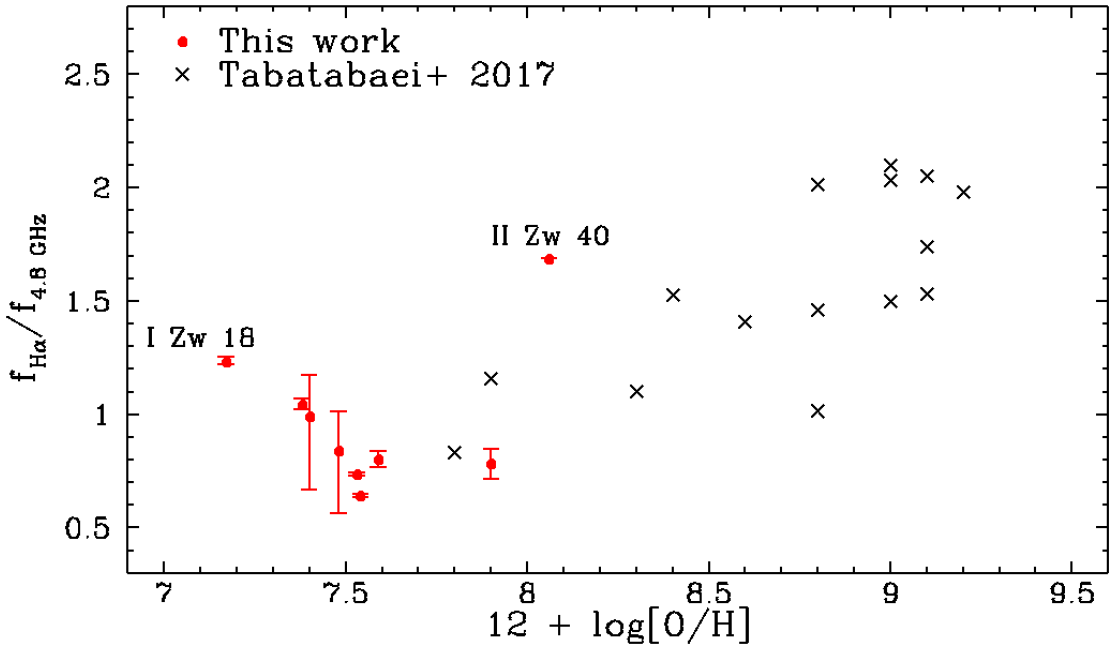

(b) Ratio of 4.8 GHz to Hα flux as a function of nebular oxygen abundance, for my low- and high-metallicity dwarf galaxies. Red filled circles are my XMD sample. Black crosses are the LVL/KINGFISHER nearby dwarf sample of Tabatabaei *et al.* (2017). Leo A is detected. The ratio of 4.8 GHz/Hα for the XMD sample is generally below that of the higher metallicity galaxies.

Chapter 5

CONCLUSIONS AND FUTURE WORK

5.1 Summary

I have obtained multi-wavelength radio continuum observations of a sample of 10 nearby dwarf galaxies with oxygen abundances between 1/5th and 1/50th of the Solar value, or $7.1 < 12 + (O/H) < 8.1$. All but one of these galaxies are "extremely metal-deficient" (XMD) dwarfs, with nebular oxygen abundances less than 1/10th Solar. I have detected all 10 of the galaxies at 4.8 GHz with the *JVLA*; for seven of these galaxies–Leo A, UGC 4704, HS 0822+3542, SBS 0940+544, and SBS 1129+476–these are the first detections of radio continuum flux. These new detections allow me to better constrain the impact of gas-phase metallicity on the radio/IR relationship. I find that the radio/IR q-factor for XMDs does exhibit at slight deficiency as a function of nebular oxygen abundance at 4.8 GHz. This relationship is less clear at 1.4 GHz.

Assuming there is a genuine deficit in q_{24} at lower metallicities, does this reflect a greater change in mid-infrared or radio behavior? Both of these star formation indicators are found to exhibit deficiencies relative to Hα luminosities. Engelbracht *et al.* (2008) similarly finds hat that they are both deficient relative to neutral HI mass at low metallicity–e.g. proof that the calorimeter model of Völk (1989) is breaking down. However the low-luminosity "conspiracy" of Bell (2003) does not hold at low metallicity: the deficiency of q_{24} at $12 + (O/H) < 8.0$, and the comparison of the 24μm and 4.8GHz ratios with Hα suggests indicates that the infrared deficiency is more pronounced at low metallicities than the radio deficiency, and consequently that

that the ultraviolet-to-mid-infrared luminosity conversion is breaking down faster than the electron-energy-to-radio continuum conversion.

This confirms that there is a comparative shortage of dust in the XMD dwarf galaxies relative to other comparably low-luminosity dwarf galaxies. It isn't necessarily surprising that a low-metallicity environment is deficient in dust–but recall that the radio/IR "conspiracy" depends on the infrared deficiency tracking the low luminosity, not the metallicity. So let us consider where infrared dust comes from. In a low-metallicity star-forming environment, the infrared emission depends on the rapid creation of dust by asymptotic giant branch (AGB) stars. The timescales for AGB stars are hundreds of millions or even billions of years, while the timescales for O/B stars and core collapse supernovae are millions or tens of millions of years. As we have discussed in previous sections, star formation in dwarf galaxies is "bursty", with long periods of relative quiescence interspersed by short period of rapid star formation; we have also discussed that these low mass galaxies have shallow gravitation wells, so a handful of supernovae can easily produce enough energy to eject the majority of the dwarfs interstellar medium into intergalactic space.

Core collapse supernovae timescales are far shorter than the timescales for AGB stars. While they may efficiently eject the gas fueling the current burst of star formation in a dwarf galaxy, the lower-mass stars can still inject dust at a later time. This suggests that 24 μm-bright dwarfs such as SBS 0335-052 and IIZw40 (Figure **??**) are actually experiencing their *second* major star forming event within the half billion years, and the observed dust was already in place when the current episode began.

What can we learn from the deficiency of radio continuum emission in these galaxies? Radio continuum is a combination of free-free emission from the star forming region and synchrotron from accelerated cosmic rays in supernova shocks; the

timescales for these mechanisms are shorter than the timescales for dust formation that drives the infrared luminosity. While Sextans A has a strikingly steep spectral slope, suggestive of rapid synchrotron aging, the majority of low metallicity dwarf galaxies exhibit flat spectral indices. This makes the separation of the thermal and non-thermal radio continuum components difficult, and suggests that a very large fraction of the continuum flux is actually thermal Bremsstrahlung radiation, rather than synchrotron radio. The morphology of the radio flux backs this assertion up: while there is some evidence for diffuse flux in several sources, the bulk of the radio continuum flux from all galaxies is strongly correlated with the Hα-bright star formation regions, consistent with a thermal origin. For a sample of bright star clusters in normal spiral galaxies, Linden (2017) finds that the spectral slope of the radio continuum correlates with the stellar age of the cluster, with flatter slopes associated with the very youngest clusters. In future work, it would be interesting to constrain the ages of the associated star clusters using e.g. broad band optical colors and SED fitting, to determine if the spectral slopes do indeed correlate with the cluster ages. It would also be tremendously useful to acquire higher frequency radio continuum observations, e.g X-, Ka, or Q-band, in order to better constrain the thermal vs. non-thermal components.

5.1.1 What Is Best Indicator of Star Formation Rate?

This dissertation has focused on understanding the low-mass, low-metallicity behavior of one of these canonical star-forming relationships: the IR/radio relationship. Since we cannot readily count the true number of stars "born" every year in a galaxy, we must contrive observational measures which most accurately reflect the underlying rate of star formation. Integrated Hα luminosity is most commonly used as the raw

measure of "true" star formation rate of a galaxy: Ultraviolet light would perhaps be the more accurate observational measure, but it can be extremely difficult to estimate losses due to extinction from the ultraviolet slope β alone.

The current standard is the Calzetti H$\alpha + 24\mu$m luminosity. This Calzetti Hα measure attempts to capture both the ionizing UV (in the form of recombination emission) and the reprocessed contribution from the warm dust. There are still caveats, of course: to begin with, this measure has been calibrated only for galaxies with $12 + (O/H) > 8.1$. Resolved studies of Hα suggest that not all H-alpha is concentrated in active star formation regions; up to half of the total Hα luminosity may originate in the diffuse ionized medium.

Not all modes of star formation include the creation of high-mass stars. Because high mass stars represent a relatively small fraction of the standard IMF, in the Milky Way it is possible to have regions of low-intensity star formation without any high-mass stars at all. In the Milky Way we see two very different modes of star formation: there are high-mass, high-intensity star formation regions such as Orion, but also lower intensity, low-mass star formation regions such as Taurus. Assuming that the underlying initial mass function of stars is the same–and we do assume this for the Milky Way (Luhman, 2018; Myers *et al.*, 2011)–the main difference between Orion and Taurus is simply the presence or absence of high mass stars, which is determined simply by number statistics. Lacking high mass stars, these stars may remain embedded in their molecular clouds for a prolonged period of time, with little ionizing radiation to disassociate or ionize the surrounding interstellar medium. Very little H-alpha emission will be associated with these regions, and hence the true star formation rate may be underestimated.

5.2 Dwarf Starbursts as Protogalaxy Analogs

Modern dwarf starbursts are imperfect analogs for protogalaxies at best: despite their extreme metallicities, we now know that most if not all of these galaxies do have pre-existing stellar populations. We are therefore not observing truly primordial objects that simply got a "late" start; rather, XMDs in the modern universe have maintained their unenriched ISM through a combination of efficient stellar winds and fueling from near-primordial gas reservoirs. The utility of local XMDs as cosmological tools ultimately depends on the degree to which their physical properties emulate their high redshift counterparts. This will require better estimates of the primordial luminosity function, and of the evolution mass-metallicity relationship at early times.

One potential difference between protogalaxies and modern XMDs is the intensity and overall level of star formation. While modern-day dwarfs are increasingly important sites of star formation in the modern day universe due to "down-sizing"–the shutting off of star formation in massive galaxies at late times–modern dwarfs span a range of star formation intensities, from almost-quiescent objects such as Leo A to powerful starbursts such as II Zw 40 or SBS 0335-052E. Low-metallicity starbursts are particularly rare in the modern universe; most of the truly local ($D < 2Mpc$) galaxies in my sample are forming stars at a lower rate. While it would be useful to create a volume-complete sample of XMDs out to at least 30 Mpc, such a sample would necessarily be weighted towards lower-SFR objects.

One feature of dwarf starbursts which this work has only briefly touched on is the presence of outflows and galactic-scale winds. These are nearly ubiquitous features of high-redshift starbursts. In the modern universe, outflows are presumed to play an important role both in regulating the bursty star formation rates of dwarf galaxies,

and in maintaining the extremely low metallicities observed in XMDs. However, there currently a pronounced lack of observational evidence directly confirming outflows in XMD dwarf galaxies in the low-redshift universe.

5.3 Future Work

For future work, I plan to request more time from the JVLA to expand my radio continuum survey to the full XMD list, and to obtain higher-frequency observations which would allow me to better separate the thermal vs. non-thermal component. I have obtained emission-line Hα and Hβ imaging of all of the galaxies in my radio continuum sample–this will allow me to compare more directly with Hα luminosities, and explore the geometry of the dust via the Balmer break. Near-UV and far-UV colors for *GALEX* would allow me to calculate the ultraviolet slope β, which is also commonly used as a dust indicator. A comparison of Hα and UV luminosities as a function of metallicity would verify or refute assertions that dust and metallicity do not play a role in the discrepancies in the UV/optical star forming indicators for dwarf galaxies Lee *et al.* (2009a); McQuinn *et al.* (2015).

High-resolution, absorption-line spectroscopy towards bright star-forming regions in these galaxies might confirm the supposition that modern XMDs maintain their extreme metallicities via the ejections of their enriched stellar products in galactic winds. Emission line studies of the atomic and molecular gas can likewise provide information about the gas reservoirs fueling the current star formation episodes in these dwarf galaxies. Molecular observations are particularly exciting, because CO observations of metal-poor dwarf galaxies have historically resulted in non-detections. Just as the *JVLA* has been able to expand our radio continuum data sets to lower

luminosity sources, *ALMA* has likewise opened up the possibility of observing low metallicity galaxies which were previously undetectable with single-dish observations (Rubio *et al.*, 2015).

Abel, T., G. L. Bryan and M. L. Norman, "The Formation of the First Star in the Universe", Science **295**, 5552, 93–98 (2002).

Alloin, D., S. Collin-Souffrin, M. Joly and L. Vigroux, "Nitrogen and oxygen abundances in galaxies", A&A, **78**, 200–216 (1979).

Aloisi, A., G. Clementini, M. Tosi, F. Annibali, R. Contreras, G. Fiorentino, J. Mack, M. Marconi, I. Musella, A. Saha, M. Sirianni and R. P. van der Marel, "I Zw 18 Revisited with HST ACS and Cepheids: New Distance and Age", ApJL, **667**, L151–L154 (2007).

Anders, E. and N. Grevesse, "Abundances of the elements - Meteoritic and solar", GeoCoA, **53**, 197–214 (1989).

Asplund, M., N. Grevesse and A. J. Sauval, "The Solar Chemical Composition", in "Cosmic Abundances as Records of Stellar Evolution and Nucleosynthesis", edited by T. G. Barnes, III and F. N. Bash, vol. 336 of *Astronomical Society of the Pacific Conference Series*, p. 25 (2005).

Asplund, M., N. Grevesse, A. J. Sauval and P. Scott, "The Chemical Composition of the Sun", ARA&A, **47**, 481–522 (2009).

Atek, H., J. Richard, M. Jauzac, J.-P. Kneib, P. Natarajan, M. Limousin, D. Schaerer, E. Jullo, H. Ebeling, E. Egami and B. Clement, "Are Ultra-faint Galaxies at z = 6-8 Responsible for Cosmic Reionization? Combined Constraints from the Hubble Frontier Fields Clusters and Parallels", ApJ, **814**, 1, 69 (2015).

Barone, L. T., A. Heithausen, S. Hüttemeister, T. Fritz and U. Klein, "Molecular gas in blue compact dwarf galaxies", MNRAS, **317**, 649–657 (2000).

Bastian, N., K. R. Covey and M. R. Meyer, "A Universal Stellar Initial Mass Function? A Critical Look at Variations", ARA&A, **48**, 339–389 (2010).

Bechtold, J., R. J. Weymann, Z. Lin and M. A. Malkan, "The integrated ultraviolet radiation field from QSOs", ApJ, **315**, 180–197 (1987).

Beck, R. and M. Krause, "Revised equipartition and minimum energy formula for magnetic field strength estimates from radio synchrotron observations", Astronomische Nachrichten **326**, 414–427 (2005).

Bell, E. F., "Estimating Star Formation Rates from Infrared and Radio Luminosities: The Origin of the Radio-Infrared Correlation", ApJ, **586**, 794–813 (2003).

Berg, D. A., E. D. Skillman, A. R. Marble, L. van Zee, C. W. Engelbracht, J. C. Lee, R. C. Kennicutt, Jr., D. Calzetti, D. A. Dale and B. D. Johnson, "Direct Oxygen Abundances for Low-luminosity LVL Galaxies", ApJ, **754**, 98 (2012).

Bergvall, N. and G. Östlin, "Massive (?) starburst hosts of blue compact galaxies (BCGs). Optical/near-IR observations of 4 BCGs and their companions", A&A, **390**, 891–915 (2002).

Bernard, E. J., M. Monelli, C. Gallart, G. Fiorentino, S. Cassisi, A. Aparicio, A. A. Cole, I. Drozdovsky, S. L. Hidalgo, E. D. Skillman, P. B. Stetson and E. Tolstoy, "The ACS LCID Project - VIII. The short-period Cepheids of Leo A", MNRAS, **432**, 3047–3061 (2013).

Binney, J. and S. Tremaine, *Galactic dynamics* (Princeton University Press, 1987).

Blain, A. W., I. Smail, R. J. Ivison, J. P. Kneib and D. T. Frayer, "Submillimeter galaxies", PhR, **369**, 2, 111–176 (2002).

Blanton, M. R., M. A. Bershady, B. Abolfathi, F. D. Albareti, C. Allende Prieto, A. Almeida, J. Alonso-García, F. Anders, S. F. Anderson, B. Andrews and et al., "Sloan Digital Sky Survey IV: Mapping the Milky Way, Nearby Galaxies, and the Distant Universe", AJ, **154**, 28 (2017).

Borthakur, S., T. M. Heckman, C. Leitherer and R. A. Overzier, "A local clue to the reionization of the universe", Science **346**, 6206, 216–219 (2014).

Bothun, G., *Modern cosmological observations and problems* (Taylor & Francis, London; Bristol, Pa., 1998).

Bourne, N., L. Dunne, R. J. Ivison, S. J. Maddox, M. Dickinson and D. T. Frayer, "Evolution of the far-infrared-radio correlation and infrared spectral energy distributions of massive galaxies over z= 0-2", MNRAS, **410**, 2, 1155–1173 (2011).

Bowman, J. D., A. E. E. Rogers, R. A. Monsalve, T. J. Mozdzen and N. Mahesh, "An absorption profile centred at 78 megahertz in the sky-averaged spectrum", Nature, **555**, 7694, 67–70 (2018).

Bromm, V. and A. Loeb, "The formation of the first low-mass stars from gas with low carbon and oxygen abundances", Nature, **425**, 6960, 812–814 (2003).

Calzetti, D., R. C. Kennicutt, C. W. Engelbracht, C. Leitherer, B. T. Draine, L. Kewley, J. Moustakas, M. Sosey, D. A. Dale, K. D. Gordon, G. X. Helou, D. J. Hollenbach, L. Armus, G. Bendo, C. Bot, B. Buckalew, T. Jarrett, A. Li, M. Meyer, E. J. Murphy, M. Prescott, M. W. Regan, G. H. Rieke, H. Roussel, K. Sheth, J. D. T. Smith, M. D. Thornley and F. Walter, "The Calibration of Mid-Infrared Star Formation Rate Indicators", ApJ, **666**, 870–895 (2007).

Cannon, J. M., F. Walter, E. D. Skillman and L. van Zee, "The Nature of Radio Continuum Emission at Very Low Metallicity: Very Large Array Observations of I Zw 18", ApJL, **621**, 1, L21–L24 (2005).

Capak, P. L., H. I. Teplitz, T. Y. Brooke, R. Laher and S. Science Center, "Science Quality Mosaics and Source List for the Spitzer Heritage Archive", in "American Astronomical Society Meeting Abstracts #221", vol. 221 of *American Astronomical Society Meeting Abstracts*, p. 340.06 (2013).

Caplan, J. and L. Deharveng, "Extinction and reddening of H II regions in the Large Magellanic Cloud", A&A, **155**, 297–313 (1986).

Casey, C. M., D. Narayanan and A. Cooray, "Dusty star-forming galaxies at high redshift", PhR, **541**, 2, 45–161 (2014).

Christensen, C. R., R. Davé, F. Governato, A. Pontzen, A. Brooks, F. Munshi, T. Quinn and J. Wadsley, "In-N-Out: The Gas Cycle from Dwarfs to Spiral Galaxies", ApJ, **824**, 1, 57 (2016).

Chyży, K. T., J. Knapik, D. J. Bomans, U. Klein, R. Beck, M. Soida and M. Urbanik, "Magnetic fields and ionized gas in the local group irregular galaxies IC 10 and NGC 6822", A&A, **405**, 513–524 (2003).

Chyży, K. T., M. Weżgowiec, R. Beck and D. J. Bomans, "Magnetic fields in Local Group dwarf irregulars", A&A, **529**, A94 (2011).

Cigan, P., L. Young, D. Cormier, V. Lebouteiller, S. Madden, D. Hunter, E. Brinks, B. Elmegreen, A. Schruba, V. Heesen and the LITTLE THINGS Team, "Herschel Spectroscopic Observations of Little Things Dwarf Galaxies", AJ, **151**, 14 (2016).

Clarke, C. and M. S. Oey, "Galactic porosity and a star formation threshold for the escape of ionizing radiation from galaxies", MNRAS, **337**, 4, 1299–1308 (2002).

Condon, J. J., "Radio emission from normal galaxies", ARA&A, **30**, 575–611 (1992).

Condon, J. J., W. D. Cotton, E. W. Greisen, Q. F. Yin, R. A. Perley, G. B. Taylor and J. J. Broderick, "The NRAO VLA Sky Survey", AJ, **115**, 1693–1716 (1998).

Cook, D. O., D. A. Dale, B. D. Johnson, L. Van Zee, J. C. Lee, R. C. Kennicutt, D. Calzetti, S. M. Staudaher and C. W. Engelbracht, "Spitzer Local Volume Legacy (LVL) SEDs and physical properties", MNRAS, **445**, 899–912 (2014a).

Cook, D. O., D. A. Dale, B. D. Johnson, L. Van Zee, J. C. Lee, R. C. Kennicutt, D. Calzetti, S. M. Staudaher and C. W. Engelbracht, "The Spitzer Local Volume Legacy (LVL) global optical photometry", MNRAS, **445**, 881–889 (2014b).

Cowie, L. L., E. M. Hu, A. Songaila and E. Egami, "The Evolution of the Distribution of Star Formation Rates in Galaxies", ApJL, **481**, L9–L13 (1997).

Cowley, W. I., C. G. Lacey, C. M. Baugh, S. Cole, C. S. Frenk and C. d. P. Lagos, "The evolution of the UV-to-mm extragalactic background light: evidence for a top-heavy initial mass function?", MNRAS, **487**, 3, 3082–3101 (2019).

Cullen, F., R. J. McLure, J. S. Dunlop, S. Khochfar, R. Davé, R. Amorín, M. Bolzonella, A. C. Carnall, M. Castellano, A. Cimatti, M. Cirasuolo, G. Cresci, J. P. U. Fynbo, F. Fontanot, A. Gargiulo, B. Garilli, L. Guaita, N. Hathi, P. Hibon, F. Mannucci, F. Marchi, D. J. McLeod, L. Pentericci, L. Pozzetti, A. E. Shapley, M. Talia and G. Zamorani, "The VANDELS survey: the stellar metallicities of star-forming galaxies at 2.5 < z < 5.0", MNRAS, **487**, 2, 2038–2060 (2019).

Dalcanton, J. J., B. F. Williams, A. C. Seth, A. Dolphin, J. Holtzman, K. Rosema, E. D. Skillman, A. Cole, L. Girardi, S. M. Gogarten, I. D. Karachentsev, K. Olsen, D. Weisz, C. Christensen, K. Freeman, K. Gilbert, C. Gallart, J. Harris, P. Hodge, R. S. de Jong, V. Karachentseva, M. Mateo, P. B. Stetson, M. Tavarez, D. Zaritsky, F. Governato and T. Quinn, "The ACS Nearby Galaxy Survey Treasury", ApJS, **183**, 67–108 (2009).

Dalcanton, J. J., P. Yoachim and R. A. Bernstein, "The Formation of Dust Lanes: Implications for Galaxy Evolution", ApJ, **608**, 189–207 (2004).

Dale, D. A., S. A. Cohen, L. C. Johnson, M. D. Schuster, D. Calzetti, C. W. Engelbracht, A. Gil de Paz, R. C. Kennicutt, J. C. Lee, A. Begum, M. Block, J. J. Dalcanton, J. G. Funes, K. D. Gordon, B. D. Johnson, A. R. Marble, S. Sakai, E. D. Skillman, L. van Zee, F. Walter, D. R. Weisz, B. Williams, S.-Y. Wu and Y. Wu, "The Spitzer Local Volume Legacy: Survey Description and Infrared Photometry", ApJ, **703**, 517–556 (2009).

Dohm-Palmer, R. C., E. D. Skillman, A. Saha, E. Tolstoy, M. Mateo, J. Gallagher, J. Hoessel, C. Chiosi and R. J. Dufour, "The Dwarf Irregular Galaxy Sextans A. II. Recent Star Formation History", AJ, **114**, 2527 (1997).

Dolphin, A. E., A. Saha, E. D. Skillman, R. C. Dohm-Palmer, E. Tolstoy, A. A. Cole, J. S. Gallagher, J. G. Hoessel and M. Mateo, "Deep Hubble Space Telescope Imaging of Sextans A. II. Cepheids and Distance", AJ, **125**, 1261–1290 (2003a).

Dolphin, A. E., A. Saha, E. D. Skillman, R. C. Dohm-Palmer, E. Tolstoy, A. A. Cole, J. S. Gallagher, J. G. Hoessel and M. Mateo, "Deep Hubble Space Telescope Imaging of Sextans A. III. The Star Formation History", AJ, **126**, 187–196 (2003b).

Edmunds, M. G. and B. E. J. Pagel, "On the composition of H II regions in southern galaxies. III - NGC 2997 and 7793", MNRAS, **211**, 507–519 (1984).

Eisenstein, D. J., D. H. Weinberg, E. Agol, H. Aihara, C. Allende Prieto, S. F. Anderson, J. A. Arns, É. Aubourg, S. Bailey, E. Balbinot and et al., "SDSS-III: Massive Spectroscopic Surveys of the Distant Universe, the Milky Way, and Extra-Solar Planetary Systems", AJ, **142**, 72 (2011).

El-Badry, K., D. R. Weisz and E. Quataert, "The statistical challenge of constraining the low-mass IMF in Local Group dwarf galaxies", MNRAS, **468**, 1, 319–332 (2017).

Engelbracht, C. W., K. D. Gordon, G. H. Rieke, M. W. Werner, D. A. Dale and W. B. Latter, "Metallicity Effects on Mid-Infrared Colors and the 8 μm PAH Emission in Galaxies", ApJL, **628**, L29–L32 (2005).

Engelbracht, C. W., G. H. Rieke, K. D. Gordon, J.-D. T. Smith, M. W. Werner, J. Moustakas, C. N. A. Willmer and L. Vanzi, "Metallicity Effects on Dust Properties in Starbursting Galaxies", ApJ, **678**, 804–827 (2008).

Erb, D. K., A. M. Quider, A. L. Henry and C. L. Martin, "Galactic Outflows in Absorption and Emission: Near-ultraviolet Spectroscopy of Galaxies at 1 < z < 2", ApJ, **759**, 1, 26 (2012).

Ferrarese, L., H. C. Ford, J. Huchra, R. C. Kennicutt, Jr., J. R. Mould, S. Sakai, W. L. Freedman, P. B. Stetson, B. F. Madore, B. K. Gibson, J. A. Graham, S. M. Hughes, G. D. Illingworth, D. D. Kelson, L. Macri, K. Sebo and N. A. Silbermann, "A Database of Cepheid Distance Moduli and Tip of the Red Giant Branch, Globular Cluster Luminosity Function, Planetary Nebula Luminosity Function, and Surface Brightness Fluctuation Data Useful for Distance Determinations", ApJS, **128**, 431–459 (2000).

Fitzpatrick, E. L., "Correcting for the Effects of Interstellar Extinction", PASP, **111**, 63–75 (1999).

Garnett, D. R., "Electron temperature variations and the measurement of nebular abundances", AJ, **103**, 1330–1337 (1992).

Geha, M., T. M. Brown, J. Tumlinson, J. S. Kalirai, J. D. Simon, E. N. Kirby, D. A. Vand enBerg, R. R. Muñoz, R. J. Avila, P. Guhathakurta and H. C. Ferguson, "The Stellar Initial Mass Function of Ultra-faint Dwarf Galaxies: Evidence for IMF Variations with Galactic Environment", ApJ, **771**, 1, 29 (2013).

Gil de Paz, A., B. F. Madore and O. Pevunova, "Palomar/Las Campanas Imaging Atlas of Blue Compact Dwarf Galaxies. I. Images and Integrated Photometry", ApJS, **147**, 29–59 (2003a).

Gil de Paz, A., B. F. Madore and O. Pevunova, "Palomar/Las Campanas Imaging Atlas of Blue Compact Dwarf Galaxies. I. Images and Integrated Photometry", The Astrophysical Journal Supplement Series **147**, 29–59 (2003b).

Ginzburg, V. L. and S. I. Syrovatskii, "Cosmic Magnetobremsstrahlung (synchrotron Radiation)", ARA&A, **3**, 297 (1965).

Giovanelli, R., M. P. Haynes, E. A. K. Adams, J. M. Cannon, K. L. Rhode, J. J. Salzer, E. D. Skillman, E. Z. Bernstein-Cooper and K. B. W. McQuinn, "ALFALFA Discovery of the Nearby Gas-rich Dwarf Galaxy Leo P. I. H I Observations", AJ, **146**, 15 (2013).

González-López, J., L. F. Barrientos, M. D. Gladders, E. Wuyts, J. Rigby, K. Sharon, M. Aravena, M. B. Bayliss and E. Ibar, "ALMA Resolves the Molecular Gas in a Young Low-metallicity Starburst Galaxy at z = 1.7", ApJL, **846**, 2, L22 (2017).

Gordon, K. D., G. C. Clayton, A. N. Witt and K. A. Misselt, "The Flux Ratio Method for Determining the Dust Attenuation of Starburst Galaxies", ApJ, **533**, 1, 236–244 (2000).

Grazian, A., E. Giallongo, D. Paris, K. Boutsia, M. Dickinson, P. Santini, R. A. Windhorst, R. A. Jansen, S. H. Cohen, T. A. Ashcraft, C. Scarlata, M. J. Rutkowski, E. Vanzella, F. Cusano, S. Cristiani, M. Giavalisco, H. C. Ferguson, A. Koekemoer, N. A. Grogin, M. Castellano, F. Fiore, A. Fontana, F. Marchi, F. Pedichini, L. Pentericci, R. Amorín, G. Barro, A. Bonchi, A. Bongiorno, S. M. Faber, M. Fumana, A. Galametz, L. Guaita, D. D. Kocevski, E. Merlin, M. Nonino, R. W. O'Connell, S. Pilo, R. E. Ryan, E. Sani, R. Speziali, V. Testa, B. Weiner and H. Yan, "Lyman continuum escape fraction of faint galaxies at z 3.3 in the CANDELS/GOODS-North, EGS, and COSMOS fields with LBC", A&A, **602**, A18 (2017).

Grocholski, A. J., R. P. van der Marel, A. Aloisi, F. Annibali, L. Greggio and M. Tosi, "HST/ACS Photometry of Old Stars in NGC 1569: The Star Formation History of a nearby Starburst", AJ, **143**, 117 (2012).

Gunn, J. E. and B. A. Peterson, "On the Density of Neutral Hydrogen in Intergalactic Space.", ApJ, **142**, 1633–1641 (1965).

Guseva, N. G., Y. I. Izotov, K. J. Fricke and C. Henkel, "New candidates for extremely metal-poor emission-line galaxies in the SDSS/BOSS DR10", A&A, **579**, A11 (2015).

Guseva, N. G., Y. I. Izotov and T. X. Thuan, "A Spectroscopic Study of a Large Sample Of Wolf-Rayet Galaxies", ApJ, **531**, 776–803 (2000).

Guseva, N. G., P. Papaderos, Y. I. Izotov, R. F. Green, K. J. Fricke, T. X. Thuan and K. G. Noeske, "Spectroscopic and photometric studies of low-metallicity star-forming dwarf galaxies . I. SBS 1129+576", A&A, **407**, 75–90 (2003).

Hanish, D. J., P. Capak, H. I. Teplitz, V. Desai, L. Armus, C. Brinkworth, T. Brooke, J. Colbert, L. Edwards, D. Fadda, D. Frayer, M. Huynh, M. Lacy, E. Murphy,

A. Noriega-Crespo, R. Paladini, C. Scarlata and S. Shenoy, "The Spitzer Archival Far-Infrared Extragalactic Survey", ApJS, **217**, 17 (2015).

Hashimoto, T., A. K. Inoue, K. Mawatari, Y. Tamura, H. Matsuo, H. Furusawa, Y. Harikane, T. Shibuya, K. K. Knudsen, K. Kohno, Y. Ono, E. Zackrisson, T. Okamoto, N. Kashikawa, P. A. Oesch, M. Ouchi, K. Ota, I. Shimizu, Y. Taniguchi, H. Umehata and D. Watson, "Big Three Dragons: A z = 7.15 Lyman-break galaxy detected in [O III] 88 μm, [C II] 158 μm, and dust continuum with ALMA", PASJ, p. 70 (2019).

Haynes, M. P., R. Giovanelli, B. R. Kent, E. A. K. Adams, T. J. Balonek, D. W. Craig, D. Fertig, R. Finn, C. Giovanardi, G. Hallenbeck, K. M. Hess, G. L. Hoffman, S. Huang, M. G. Jones, R. A. Koopmann, D. A. Kornreich, L. Leisman, J. Miller, C. Moorman, J. O'Connor, A. O'Donoghue, E. Papastergis, P. Troischt, D. Stark and L. Xiao, "The Arecibo Legacy Fast ALFA Survey: The ALFALFA Extragalactic H I Source Catalog", ApJ, **861**, 49 (2018).

Heckman, T. M., L. Armus and G. K. Miley, "On the Nature and Implications of Starburst-driven Galactic Superwinds", ApJS, **74**, 833 (1990).

Helou, G. and M. D. Bicay, "A physical model of the infrared-to-radio correlation in galaxies", ApJ, **415**, 93–100 (1993).

Helou, G., I. R. Khan, L. Malek and L. Boehmer, "IRAS observations of galaxies in the Virgo cluster area", ApJS, **68**, 151–172 (1988).

Henry, A., C. L. Martin, K. Finlator and A. Dressler, "The Metallicity Evolution of Low-mass Galaxies: New Constraints at Intermediate Redshift", ApJ, **769**, 148 (2013a).

Henry, A., C. L. Martin, K. Finlator and A. Dressler, "The Metallicity Evolution of Low-mass Galaxies: New Constraints at Intermediate Redshift", ApJ, **769**, 2, 148 (2013b).

Hikage, C., J. Schmalzing, T. Buchert, Y. Suto, I. Kayo, A. Taruya, M. S. Vogeley, F. Hoyle, J. R. Gott, III and J. Brinkmann, "Minkowski Functionals of SDSS Galaxies I : Analysis of Excursion Sets", PASJ, **55**, 911–931 (2003).

Hindson, L., G. Kitchener, E. Brinks, V. Heesen, J. Westcott, D. Hunter, H.-X. Zhang, M. Rupen and U. Rau, "A Radio Continuum Study of Dwarf Galaxies: 6 cm Imaging of LITTLE THINGS", ApJS, **234**, 29 (2018).

Hinkel, N. R., *Stellar Abundances in the Solar Neighborhood*, Ph.D. thesis, Arizona State University (2012).

Hirschauer, A. S., J. J. Salzer, E. D. Skillman, D. Berg, K. B. W. McQuinn, J. M. Cannon, A. J. R. Gordon, M. P. Haynes, R. Giovanelli, E. A. K. Adams, S. Janowiecki, K. L. Rhode, R. W. Pogge, K. V. Croxall and E. Aver, "ALFALFA Discovery of the Most Metal-poor Gas-rich Galaxy Known: AGC 198691", ApJ, **822**, 108 (2016).

Hodge, P., R. C. Kennicutt and N. Strobel, "The H II regions of Sextans A", PASP, **106**, 765–769 (1994).

Högbom, J. A., "Aperture Synthesis with a Non-Regular Distribution of Interferometer Baselines", A&AS, **15**, 417 (1974).

Houck, J. R., V. Charmandaris, B. R. Brandl, D. Weedman, T. Herter, L. Armus, B. T. Soifer, J. Bernard-Salas, H. W. W. Spoon and D. Devost, "The Extraordinary Mid-infrared Spectrum of the Blue Compact Dwarf Galaxy SBS 0335-052", ApJS, **154**, 1, 211–214 (2004).

Hsu, L.-Y., V. Desai, E. J. Murphy, L. L. Cowie, I. Heywood, E. Momjian, A. J. Barger and I. Smail, "The Hawaii SCUBA-2 Lensing Cluster Survey: Radio-detected Submillimeter Galaxies in the HST Frontier Fields", ApJ, **840**, 1, 29 (2017).

Huchra, J. P., L. M. Macri, K. L. Masters, T. H. Jarrett, P. Berlind, M. Calkins, A. C. Crook, R. Cutri, P. Erdoğdu, E. Falco, T. George, C. M. Hutcheson, O. Lahav, J. Mader, J. D. Mink, N. Martimbeau, S. Schneider, M. Skrutskie, S. Tokarz and M. Westover, "The 2MASS Redshift Survey–Description and Data Release", ApJS, **199**, 26 (2012).

Hunt, L., S. Bianchi and R. Maiolino, "The optical-to-radio spectral energy distributions of low-metallicity blue compact dwarf galaxies", A&A, **434**, 849–866 (2005a).

Hunt, L. K., K. K. Dyer and T. X. Thuan, "The radio continuum of the extremely metal-poor blue compact dwarf galaxy I Zw 18", A&A, **436**, 3, 837–844 (2005b).

Hunt, L. K., K. K. Dyer, T. X. Thuan and J. S. Ulvestad, "The Radio Continuum of the Metal-deficient Blue Compact Dwarf Galaxy SBS 0335-052", ApJ, **606**, 2, 853–861 (2004).

Hunter, D. A. and B. G. Elmegreen, "Star Formation Properties of a Large Sample of Irregular Galaxies", AJ, **128**, 2170–2205 (2004).

Hunter, D. A., D. Ficut-Vicas, T. Ashley, E. Brinks, P. Cigan, B. G. Elmegreen, V. Heesen, K. A. Herrmann, M. Johnson, S.-H. Oh, M. P. Rupen, A. Schruba, C. E. Simpson, F. Walter, D. J. Westpfahl, L. M. Young and H.-X. Zhang, "Little Things", AJ, **144**, 134 (2012).

Hunter, D. A. and J. S. Gallagher, III, "An Emission-line Study of Supergiant Ionized Filaments in Irregular Galaxies", ApJ, **475**, 65–82 (1997).

Hunter, D. A. and J. D. Plummer, "Sextans A: A Case Study of Star Formation and Gas Densities in Irregular Galaxies", ApJ, **462**, 732 (1996).

Inoue, A. K. and I. Iwata, "A Monte Carlo simulation of the intergalactic absorption and the detectability of the Lyman continuum from distant galaxies", MNRAS, **387**, 1681–1692 (2008).

Inoue, A. K., I. Shimizu, I. Iwata and M. Tanaka, "An updated analytic model for attenuation by the intergalactic medium", MNRAS, **442**, 1805–1820 (2014).

Izotov, Y. I., N. G. Guseva, K. J. Fricke and P. Papaderos, "SBS 0335-052E+W: deep VLT/FORS+UVES spectroscopy of the pair of the lowest-metallicity blue compact dwarf galaxies", A&A, **503**, 61–72 (2009).

Izotov, Y. I., N. G. Guseva and T. X. Thuan, "Green Pea Galaxies and Cohorts: Luminous Compact Emission-line Galaxies in the Sloan Digital Sky Survey", ApJ, **728**, 161 (2011).

Izotov, Y. I., I. Orlitová, D. Schaerer, T. X. Thuan, A. Verhamme, N. G. Guseva and G. Worseck, "Eight per cent leakage of Lyman continuum photons from a compact, star-forming dwarf galaxy", Nature, **529**, 7585, 178–180 (2016a).

Izotov, Y. I., P. Papaderos, N. G. Guseva, K. J. Fricke and T. X. Thuan, "Two extremely metal-poor emission-line galaxies in the Sloan Digital Sky Survey", A&A, **454**, 137–141 (2006a).

Izotov, Y. I., D. Schaerer, T. X. Thuan, G. Worseck, N. G. Guseva, I. Orlitová and A. Verhamme, "Detection of high Lyman continuum leakage from four low-redshift compact star-forming galaxies", MNRAS, **461**, 4, 3683–3701 (2016b).

Izotov, Y. I., G. Stasińska, G. Meynet, N. G. Guseva and T. X. Thuan, "The chemical composition of metal-poor emission-line galaxies in the Data Release 3 of the Sloan Digital Sky Survey", A&A, **448**, 955–970 (2006b).

Izotov, Y. I. and T. X. Thuan, "Heavy-Element Abundances in Blue Compact Galaxies", ApJ, **511**, 639–659 (1999).

Izotov, Y. I. and T. X. Thuan, "MMT Observations of New Extremely Metal-poor Emission-Line Galaxies in the Sloan Digital Sky Survey", ApJ, **665**, 1115–1128 (2007).

Izotov, Y. I., T. X. Thuan and N. G. Guseva, "Hunting for extremely metal-poor emission-line galaxies in the Sloan Digital Sky Survey: MMT and 3.5 m APO observations", A&A, **546**, A122 (2012).

Izotov, Y. I., T. X. Thuan, N. G. Guseva and S. E. Liss, "J0811+4730: the most metal-poor star-forming dwarf galaxy known", MNRAS, **473**, 1956–1966 (2018).

Izotov, Y. I., T. X. Thuan and V. A. Lipovetsky, "The primordial helium abundance from a new sample of metal-deficient blue compact galaxies", ApJ, **435**, 647–667 (1994).

James, B. L., S. Koposov, D. P. Stark, V. Belokurov, M. Pettini and E. W. Olszewski, "Uncovering blue diffuse dwarf galaxies", MNRAS, **448**, 2687–2703 (2015).

Kaasinen, M., N. Scoville, F. Walter, E. Da Cunha, G. Popping, R. Pavesi, B. Darvish, C. M. Casey, D. A. Riechers and S. Glover, "The Molecular Gas Reservoirs of z $\sim$ 2 Galaxies: A Comparison of CO(1−0) and Dust-based Molecular Gas Masses", ApJ, **880**, 1, 15 (2019).

Karachentsev, I. D., "The Local Group and Other Neighboring Galaxy Groups", AJ, **129**, 178–188 (2005).

Karachentsev, I. D., V. E. Karachentseva, W. K. Huchtmeier and D. I. Makarov, "A Catalog of Neighboring Galaxies", AJ, **127**, 2031–2068 (2004).

Kaufer, A., K. A. Venn, E. Tolstoy, C. Pinte and R.-P. Kudritzki, "First Stellar Abundances in the Dwarf Irregular Galaxy Sextans A", AJ, **127**, 5, 2723–2737 (2004).

Kennicutt, J., Robert C., D. Calzetti, F. Walter, G. Helou, D. J. Hollenbach, L. Armus, G. Bendo, D. A. Dale, B. T. Draine, C. W. Engelbracht, K. D. Gordon, M. K. M. Prescott, M. W. Regan, M. D. Thornley, C. Bot, E. Brinks, E. de Blok, D. de Mello, M. Meyer, J. Moustakas, E. J. Murphy, K. Sheth and J. D. T. Smith, "Star Formation in NGC 5194 (M51a). II. The Spatially Resolved Star Formation Law", ApJ, **671**, 1, 333–348 (2007).

Kennicutt, J., Robert C., P. Tamblyn and C. E. Congdon, "Past and Future Star Formation in Disk Galaxies", ApJ, **435**, 22 (1994).

Kennicutt, R. C., Jr., "The rate of star formation in normal disk galaxies", ApJ, **272**, 54–67 (1983).

Kennicutt, R. C., Jr., "The Global Schmidt Law in Star-forming Galaxies", ApJ, **498**, 541–552 (1998).

Kennicutt, R. C., Jr., J. C. Lee, J. G. Funes, S. J., S. Sakai and S. Akiyama, "An Hα Imaging Survey of Galaxies in the Local 11 Mpc Volume", ApJS, **178**, 247–279 (2008).

Kepley, A. A., A. E. Reines, K. E. Johnson and L. M. Walker, "High Resolution Radio and Optical Observations of the Central Starburst in the Low-metallicity Dwarf Galaxy II Zw 40", AJ, **147**, 43 (2014).

Kewley, L. J. and M. A. Dopita, "Using Strong Lines to Estimate Abundances in Extragalactic H II Regions and Starburst Galaxies", ApJS, **142**, 35–52 (2002).

Kirby, E. N., "The Chemical Evolution of Milky Way Satellite Galaxies from Keck Spectroscopy", Highlights of Astronomy **16**, 278–279 (2015).

Klein, U., "Radio continuum observations of low-surface brightness dwarf galaxies", A&A, **168**, 65–68 (1986).

Klein, U., E. Hummel, D. J. Bomans and U. Hopp, "The synchrotron halo and magnetic field of NGC 4449.", A&A, **313**, 396–404 (1996).

Kleinmann, D. E. and F. J. Low, "Infrared Observations of Galaxies and of the Extended Nucleus in M82", ApJL, **161**, L203 (1970a).

Kleinmann, D. E. and F. J. Low, "Observations of Infrared Galaxies", ApJL, **159**, L165 (1970b).

Kniazev, A. Y., E. K. Grebel, L. Hao, M. A. Strauss, J. Brinkmann and M. Fukugita, "Discovery of Eight New Extremely Metal Poor Galaxies in the Sloan Digital Sky Survey", ApJL, **593**, L73–L76 (2003).

Kniazev, A. Y., E. K. Grebel, S. A. Pustilnik, A. G. Pramskij and D. B. Zucker, "Spectrophotometry of Sextans A and B: Chemical Abundances of H II Regions and Planetary Nebulae", AJ, **130**, 1558–1573 (2005).

Kniazev, A. Y., S. A. Pustilnik, E. K. Grebel, H. Lee and A. G. Pramskij, "Strong Emission Line H II Galaxies in the Sloan Digital Sky Survey. I. Catalog of DR1 Objects with Oxygen Abundances from T_e Measurements", ApJS, **153**, 429–445 (2004).

Kniazev, A. Y., S. A. Pustilnik, J. Masegosa, I. Márquez, A. V. Ugryumov, J.-M. Martin, Y. I. Izotov, D. Engels, N. Brosch, U. Hopp, S. Merlino and V. A. Lipovetsky, "HS 0822+3542 - a new nearby extremely metal-poor galaxy", A&A, **357**, 101–110 (2000).

Kniazev, A. Y., S. A. Pustil'nik and A. V. Ugryumov, "New nearby very metal-deficient blue compact galaxies.", Bulletin of the Special Astrophysics Observatory **46**, 23–27 (1998).

Kobulnicky, H. A. and E. D. Skillman, "Elemental Abundance Variations and Chemical Enrichment from Massive Stars in Starbursts. II. NGC 1569", ApJ, **489**, 636–655 (1997).

Lee, H., M. L. McCall, R. L. Kingsburgh, R. Ross and C. C. Stevenson, "Uncovering Additional Clues to Galaxy Evolution. I. Dwarf Irregular Galaxies in the Field", AJ, **125**, 146–165 (2003).

Lee, H., E. D. Skillman, J. M. Cannon, D. C. Jackson, R. D. Gehrz, E. F. Polomski and C. E. Woodward, "On Extending the Mass-Metallicity Relation of Galaxies by 2.5 Decades in Stellar Mass", ApJ, **647**, 970–983 (2006).

Lee, H., E. D. Skillman and K. A. Venn, "Investigating the Possible Anomaly between Nebular and Stellar Oxygen Abundances in the Dwarf Irregular Galaxy WLM", ApJ, **620**, 223–237 (2005).

Lee, J. C., A. Gil de Paz, R. C. Kennicutt, Jr., M. Bothwell, J. Dalcanton, J. José G. Funes S., B. D. Johnson, S. Sakai, E. Skillman, C. Tremonti and L. van Zee, "A GALEX Ultraviolet Imaging Survey of Galaxies in the Local Volume", ApJS, **192**, 6 (2011).

Lee, J. C., A. Gil de Paz, C. Tremonti, R. C. Kennicutt, Jr., S. Salim, M. Bothwell, D. Calzetti, J. Dalcanton, D. Dale, C. Engelbracht, S. J. J. G. Funes, B. Johnson, S. Sakai, E. Skillman, L. van Zee, F. Walter and D. Weisz, "Comparison of Hα and UV Star Formation Rates in the Local Volume: Systematic Discrepancies for Dwarf Galaxies", ApJ, **706**, 599–613 (2009a).

Lee, J. C., R. C. Kennicutt, J. G. Funes, S. Sakai, C. A. Tremonti and L. van Zee, "11HUGS: The 11Mpc Hα and Ultraviolet Galaxy Survey", in "American Astronomical Society Meeting Abstracts", vol. 36 of *Bulletin of the American Astronomical Society*, p. 1442 (2004).

Lee, J. C., R. C. Kennicutt, Jr., S. J. J. G. Funes, S. Sakai and S. Akiyama, "Dwarf Galaxy Starburst Statistics in the Local Volume", ApJ, **692**, 1305–1320 (2009b).

Leitet, E., N. Bergvall, N. Piskunov and B. G. Andersson, "Analyzing low signal-to-noise FUSE spectra. Confirmation of Lyman continuum escape from Haro 11", A&A, **532**, A107 (2011).

Leitherer, C., S. Hernandez, J. C. Lee and M. S. Oey, "Direct Detection of Lyman Continuum Escape from Local Starburst Galaxies with the Cosmic Origins Spectrograph", ApJ, **823**, 1, 64 (2016).

Linden, S., "Star Clusters in a Subset of LEGUS/SFRS Galaxies - An Optical - Radio Comparison", in "Linking Observations and Theory Across the Scales of Star Formation in Galaxies", p. 17 (2017).

Longair, M. S., *High energy astrophysics* (Cambridge University Press, Cambridge ; New York, 1992), 2nd ed.. edn.

Loose, H.-H. and T. X. Thuan, "The morphology and structure of blue compact dwarf galaxies from CCD observations.", in "Star-forming Dwarf Galaxies and Related Objects", edited by D. Kunth, T. X. Thuan, J. Tran Thanh Van, J. Lequeux and J. Audouze, pp. 73–88 (1986).

Luhman, K. L., "The Stellar Membership of the Taurus Star-forming Region", AJ, **156**, 6, 271 (2018).

Mac Low, M.-M. and R. McCray, "Superbubbles in Disk Galaxies", ApJ, **324**, 776 (1988).

Madau, P., "Radiative transfer in a clumpy universe: The colors of high-redshift galaxies", ApJ, **441**, 18–27 (1995).

Madau, P. and M. Dickinson, "Cosmic Star-Formation History", ARA&A, **52**, 415–486 (2014).

Magrini, L., R. L. M. Corradi, R. Greimel, P. Leisy, D. J. Lennon, A. Mampaso, M. Perinotto, D. L. Pollacco, J. R. Walsh, N. A. Walton and A. A. Zijlstra, "The Local Group Census: Planetary nebulae in <ASTROBJ>IC 10</ASTROBJ>, <ASTROBJ>Leo A</ASTROBJ> and <ASTROBJ>Sextans A</ASTROBJ>", A&A, **407**, 51–59 (2003).

Magrini, L. and D. R. Gonçalves, "IC10: the history of the nearest starburst galaxy through its Planetary Nebula and HII region populations", MNRAS, **398**, 280–292 (2009).

Mao, M. Y., M. T. Huynh, R. P. Norris, M. Dickinson, D. Frayer, G. Helou and J. A. Monkiewicz, "No Evidence for Evolution in the Far-infrared-Radio Correlation out to z ˜ 2 in the Extended Chandra Deep Field South", ApJ, **731**, 79 (2011).

Markaryan, B. E., V. A. Lipovetskii and D. A. Stepanyan, "Second Byurakan Spectral Sky Survey - Part One - Quasistellar and Seyfert Objects", Astrophysics **19**, 14–25 (1983).

Martin, C. L., H. A. Kobulnicky and T. M. Heckman, "The Metal Content of Dwarf Starburst Winds: Results from Chandra Observations of NGC 1569", ApJ, **574**, 2, 663–692 (2002).

Martin, C. L., A. E. Shapley, A. L. Coil, K. A. Kornei, K. Bundy, B. J. Weiner, K. G. Noeske and D. Schiminovich, "Demographics and Physical Properties of Gas Outflows/Inflows at 0.4 < z < 1.4", ApJ, **760**, 2, 127 (2012).

Mateo, M. L., "Dwarf Galaxies of the Local Group", ARA&A, **36**, 435–506 (1998).

McGaugh, S. S., "H II region abundances - Model oxygen line ratios", ApJ, **380**, 140–150 (1991).

McKee, C. F. and J. C. Tan, "The Formation of the First Stars. II. Radiative Feedback Processes and Implications for the Initial Mass Function", ApJ, **681**, 2, 771–797 (2008).

McQuinn, K. B. W., E. D. Skillman, D. Berg, J. M. Cannon, J. J. Salzer, E. A. K. Adams, A. Dolphin, R. Giovanelli, M. P. Haynes and K. L. Rhode, "ALFALFA Discovery of the Nearby Gas-rich Dwarf Galaxy Leo P. IV. Distance Measurement from LBT Optical Imaging", AJ, **146**, 145 (2013).

McQuinn, K. B. W., E. D. Skillman, A. E. Dolphin and N. P. Mitchell, "Calibrating UV Star Formation Rates for Dwarf Galaxies from STARBIRDS", ApJ, **808**, 109 (2015).

Mould, J. R., J. P. Huchra, W. L. Freedman, R. C. Kennicutt, Jr., L. Ferrarese, H. C. Ford, B. K. Gibson, J. A. Graham, S. M. G. Hughes, G. D. Illingworth, D. D. Kelson, L. M. Macri, B. F. Madore, S. Sakai, K. M. Sebo, N. A. Silbermann and P. B. Stetson, "The Hubble Space Telescope Key Project on the Extragalactic Distance Scale. XXVIII. Combining the Constraints on the Hubble Constant", ApJ, **529**, 786–794 (2000).

Moustakas, J., R. C. Kennicutt, Jr., C. A. Tremonti, D. A. Dale, J.-D. T. Smith and D. Calzetti, "Optical Spectroscopy and Nebular Oxygen Abundances of the Spitzer/SINGS Galaxies", ApJS, **190**, 233–266 (2010).

Myers, A. T., M. R. Krumholz, R. I. Klein and C. F. McKee, "Metallicity and the Universality of the Initial Mass Function", ApJ, **735**, 1, 49 (2011).

Naidu, R. P., P. A. Oesch, N. Reddy, B. Holden, C. C. Steidel, M. Montes, H. Atek, R. J. Bouwens, C. M. Carollo, A. Cibinel, G. D. Illingworth, I. Labbé, D. Magee, L. Morselli, E. J. Nelson, P. G. van Dokkum and S. Wilkins, "The HDUV Survey: Six Lyman Continuum Emitter Candidates at z ˜ 2 Revealed by HST UV Imaging", ApJ, **847**, 12 (2017).

Nakajima, K., M. Ouchi, K. Shimasaku, Y. Ono, J. C. Lee, S. Foucaud, C. Ly, D. A. Dale, S. Salim, R. Finn, O. Almaini and S. Okamura, "Average Metallicity and Star Formation Rate of Lyα Emitters Probed by a Triple Narrowband Survey", ApJ, **745**, 12 (2012).

Nakamura, F. and M. Umemura, "The Stellar Initial Mass Function in Primordial Galaxies", ApJ, **569**, 2, 549–557 (2002).

Namumba, B., C. Carignan and S. Passmoor, "H I observations of Sextans A and B with the SKA pathfinder KAT-7", MNRAS, **478**, 487–500 (2018).

Narayanan, D. and R. Davé, "Cosmological implications of a stellar initial mass function that varies with the Jeans mass in galaxies", MNRAS, **423**, 4, 3601–3615 (2012).

Osterbrock, D. E., *Astrophysics of gaseous nebulae and active galactic nuclei* (University Science Books, Mill Valley, Calif., 1989).

Osterbrock, D. E. and G. J. Ferland, *Astrophysics of gaseous nebulae and active galactic nuclei.* (University Science Books, Sausalito, Calif., 2006), 2nd edn.

Oswalt, T. D. and G. Gilmore, eds., *The Stellar and Sub-Stellar Initial Mass Function of Simple and Composite Populations*, vol. 5 (2013).

Ott, J., F. Walter and E. Brinks, "A Chandra X-ray survey of nearby dwarf starburst galaxies - I. Data reduction and results", MNRAS, **358**, 1423–1452 (2005).

Pagel, B. E. J., M. G. Edmunds, D. E. Blackwell, M. S. Chun and G. Smith, "On the composition of H II regions in southern galaxies. I - NGC 300 and 1365", MNRAS, **189**, 95–113 (1979).

Pannella, M., D. Elbaz, E. Daddi, M. Dickinson, H. S. Hwang, C. Schreiber, V. Strazzullo, H. Aussel, M. Bethermin, V. Buat, V. Charmandaris, A. Cibinel, S. Juneau, R. J. Ivison, D. Le Borgne, E. Le Floc'h, R. Leiton, L. Lin, G. Magdis, G. E. Morrison, J. Mullaney, M. Onodera, A. Renzini, S. Salim, M. T. Sargent, D. Scott, X. Shu and T. Wang, "GOODS-Herschel: Star Formation, Dust Attenuation, and the FIR-radio Correlation on the Main Sequence of Star-forming Galaxies up to z = 4", ApJ, **807**, 2, 141 (2015).

Papaderos, P., N. G. Guseva, Y. I. Izotov and K. J. Fricke, "Extremely metal-poor star-forming galaxies. New detections and general morphological and photometric properties", A&A, **491**, 113–129 (2008).

Peel, M. W., C. Dickinson, R. D. Davies, D. L. Clements and R. J. Beswick, "Radio to infrared spectra of late-type galaxies with Planck and Wilkinson Microwave Anisotropy Probe data", MNRAS, **416**, 1, L99–L103 (2011).

Peterson, B. M. B. M., *An introduction to active galactic nuclei* (Cambridge University Press, Cambridge ; New York, 1997).

Prochaska, J. X., G. Worseck and J. M. O'Meara, "A Direct Measurement of the Intergalactic Medium Opacity to H I Ionizing Photons", ApJL, **705**, L113–L117 (2009).

Pustilnik, S. A., A. Y. Kniazev and A. G. Pramskij, "Study of DDO 68: nearest candidate for a young galaxy?", A&A, **443**, 91–102 (2005).

Pustilnik, S. A., A. G. Pramskij and A. Y. Kniazev, "SBS 0335-052 E and W: Implications of new broad-band and Hα photometry", A&A, **425**, 51–65 (2004).

Rawle, T. D., B. Altieri, E. Egami, P. G. Pérez-González, F. Boone, B. Clement, R. J. Ivison, J. Richard, W. Rujopakarn, I. Valtchanov, G. Walth, B. J. Weiner, A. W. Blain, M. Dessauges-Zavadsky, J. P. Kneib, D. Lutz, G. Rodighiero, D. Schaerer and I. Smail, "A complete census of Herschel-detected infrared sources within the HST Frontier Fields", MNRAS, **459**, 2, 1626–1645 (2016).

Rhode, K. L., J. J. Salzer, N. C. Haurberg, A. Van Sistine, M. D. Young, M. P. Haynes, R. Giovanelli, J. M. Cannon, E. D. Skillman, K. B. W. McQuinn and E. A. K. Adams, "ALFALFA Discovery of the Nearby Gas-rich Dwarf Galaxy Leo P. II. Optical Imaging Observations", AJ, **145**, 149 (2013).

Rubio, M., B. G. Elmegreen, D. A. Hunter, E. Brinks, J. R. Cortés and P. Cigan, "Dense cloud cores revealed by CO in the low metallicity dwarf galaxy WLM", Nature, **525**, 7568, 218–221 (2015).

Rybicki, G. B. and A. P. Lightman, *Radiative processes in astrophysics* (Wiley, New York, 1985).

Sakai, S., L. Ferrarese, R. C. Kennicutt, Jr. and A. Saha, "The Effect of Metallicity on Cepheid-based Distances", ApJ, **608**, 42–61 (2004).

Sakai, S., B. F. Madore and W. L. Freedman, "Tip of the Red Giant Branch Distances to Galaxies. IV. Sextans B", ApJ, **480**, 589–595 (1997).

Salpeter, E. E., "The Luminosity Function and Stellar Evolution.", ApJ, **121**, 161 (1955).

Sargent, M. T., E. Schinnerer, E. Murphy, C. L. Carilli, G. Helou, H. Aussel, E. Le Floc'h, D. T. Frayer, O. Ilbert, P. Oesch, M. Salvato, V. Smolčić, J. Kartaltepe and D. B. Sanders, "No Evolution in the IR-Radio Relation for IR-luminous Galaxies at $z < 2$ in the COSMOS Field", ApJL, **714**, L190–L195 (2010).

Scannapieco, E. and M. Brüggen, "Simulating supersonic turbulence in galaxy outflows", MNRAS, **405**, 3, 1634–1653 (2010).

Schlafly, E. F. and D. P. Finkbeiner, "Measuring Reddening with Sloan Digital Sky Survey Stellar Spectra and Recalibrating SFD", ApJ, **737**, 103 (2011).

Schlegel, D. J., D. P. Finkbeiner and M. Davis, "Maps of Dust Infrared Emission for Use in Estimation of Reddening and Cosmic Microwave Background Radiation Foregrounds", ApJ, **500**, 525–553 (1998).

Schleicher, D. R. G. and R. Beck, "A new interpretation of the far-infrared - radio correlation and the expected breakdown at high redshift", A&A, **556**, A142 (2013).

Scott, P., M. Asplund, N. Grevesse and A. J. Sauval, "On the Solar Nickel and Oxygen Abundances", ApJL, **691**, L119–L122 (2009).

Senarath, M. R., M. J. I. Brown, M. E. Cluver, J. Moustakas, L. Armus and T. H. Jarrett, "Calibrating the James Webb Space Telescope Filters as Star Formation Rate Indicators", ApJ, **869**, L26 (2018).

Senchyna, P. and D. P. Stark, "Photometric identification and MMT spectroscopy of new extremely metal-poor galaxies: towards a better understanding of young stellar populations at low metallicity", ArXiv e-prints (2018).

Shao, Y., R. Wang, C. L. Carilli, J. Wagg, F. Walter, J. Li, X. Fan, L. Jiang, D. A. Riechers, F. Bertoldi, M. A. Strauss, P. Cox, A. Omont and K. M. Menten, "Star Formation and ISM Properties in the Host Galaxies of Three Far-infrared Luminous Quasars at z $\sim$ 6", ApJ, **876**, 2, 99 (2019).

Skillman, E. D., D. J. Bomans and H. A. Kobulnicky, "Interstellar Medium Abundances in the Pegasus Dwarf Irregular Galaxy", ApJ, **474**, 205–216 (1997).

Skillman, E. D., R. C. Kennicutt and P. W. Hodge, "Oxygen abundances in nearby dwarf irregular galaxies", ApJ, **347**, 875–882 (1989).

Skillman, E. D. and R. C. Kennicutt, Jr., "Spatially resolved optical and near-infrared spectroscopy of I ZW 18", ApJ, **411**, 655–666 (1993).

Skillman, E. D., J. J. Salzer, D. A. Berg, R. W. Pogge, N. C. Haurberg, J. M. Cannon, E. Aver, K. A. Olive, R. Giovanelli, M. P. Haynes, E. A. K. Adams, K. B. W. McQuinn and K. L. Rhode, "ALFALFA Discovery of the nearby Gas-rich Dwarf Galaxy Leo P. III. An Extremely Metal Deficient Galaxy", AJ, **146**, 3 (2013).

Skillman, E. D., R. Terlevich, P. J. Teuben and H. van Woerden, "H I synthesis observations of the dwarf irregular galaxy Sextans A", A&A, **198**, 33–42 (1988).

Spitzer, L., *Physical processes in the interstellar medium* (Wiley, New York, 1977).

Stasińska, G. and Y. Izotov, "Modeling the emission line sequence of H II galaxies", A&A, **397**, 71–85 (2003).

Stepanian, J. A., "The Second Byurakan Survey. General Catalogue", RMxAA, **41**, 155–368 (2005).

Tabatabaei, F. S., R. Beck, E. Krügel, M. Krause, E. M. Berkhuijsen, K. D. Gordon and K. M. Menten, "High-resolution radio continuum survey of M 33. II. Thermal and nonthermal emission", A&A, **475**, 133–143 (2007).

Tabatabaei, F. S., E. M. Berkhuijsen, P. Frick, R. Beck and E. Schinnerer, "Multi-scale radio-infrared correlations in M 31 and M 33: The role of magnetic fields and star formation", A&A, **557**, A129 (2013a).

Tabatabaei, F. S., E. Schinnerer, M. Krause, G. Dumas, S. Meidt, A. Damas-Segovia, R. Beck, E. J. Murphy, D. D. Mulcahy, B. Groves, A. Bolatto, D. Dale, M. Galametz, K. Sandstrom, M. Boquien, D. Calzetti, R. C. Kennicutt, L. K. Hunt, I. De Looze and E. W. Pellegrini, "The Radio Spectral Energy Distribution and Star-formation Rate Calibration in Galaxies", ApJ, **836**, 185 (2017).

Tabatabaei, F. S., E. Schinnerer, E. J. Murphy, R. Beck, B. Groves, S. Meidt, M. Krause, H.-W. Rix, K. Sandstrom, A. F. Crocker, M. Galametz, G. Helou, C. D. Wilson, R. Kennicutt, D. Calzetti, B. Draine, G. Aniano, D. Dale, G. Dumas, C. W. Engelbracht, K. D. Gordon, J. Hinz, K. Kreckel, E. Montiel and H. Roussel, "A detailed study of the radio-FIR correlation in NGC 6946 with Herschel-PACS/SPIRE from KINGFISH", A&A, **552**, A19 (2013b).

Tammann, G. A., B. Reindl and A. Sandage, "New period-luminosity and period-color relations of classical Cepheids. IV. The low-metallicity galaxies IC 1613, WLM, Pegasus, Sextans A and B, and Leo A in comparison to SMC", A&A, **531**, A134 (2011).

Tehrani, K., P. A. Crowther and I. Archer, "Revealing the nebular properties and Wolf-Rayet population of IC10 with Gemini/GMOS", MNRAS, **472**, 4618–4633 (2017).

Thuan, T. X. and Y. I. Izotov, "High-Ionization Emission in Metal-deficient Blue Compact Dwarf Galaxies", ApJS, **161**, 240–270 (2005).

Tielens, A. G. G. M., *The physics and chemistry of the interstellar medium* (Cambridge University Press, Cambridge, 2005).

Tinsley, B. M., "Interpretation of the Stellar Metallicity Distribution", ApJ, **197**, 159–162 (1975).

Tremonti, C. A., T. M. Heckman, G. Kauffmann, J. Brinchmann, S. Charlot, S. D. M. White, M. Seibert, E. W. Peng, D. J. Schlegel, A. Uomoto, M. Fukugita and J. Brinkmann, "The Origin of the Mass-Metallicity Relation: Insights from 53,000 Star-forming Galaxies in the Sloan Digital Sky Survey", ApJ, **613**, 898–913 (2004).

van der Kruit, P. C., "Observations of core sources in Seyfert and normal galaxies with the Westerbork synthesis radio telescope at 1415 MHz.", A&A, **15**, 110–122 (1971).

van der Kruit, P. C., "High-resolution Radio Continuum Observations of Bright Spiral Galaxies at 1415 MHz: A General Discussion", A&A, **29**, 263 (1973).

van Dokkum, P. G., "Evidence of Cosmic Evolution of the Stellar Initial Mass Function", ApJ, **674**, 1, 29–50 (2008).

van Zee, L., "Discovery of an Extremely Metal-Poor Galaxy: Optical Spectroscopy of UGCA 292", ApJL, **543**, L31–L34 (2000).

van Zee, L. and M. P. Haynes, "Oxygen and Nitrogen in Isolated Dwarf Irregular Galaxies", ApJ, **636**, 214–239 (2006).

van Zee, L., M. P. Haynes and J. J. Salzer, "Element Enrichment and Stellar Populations O Gas-Rich Low Surface Brightness Dwarf Galaxies", AJ, **114**, 2497 (1997).

van Zee, L., E. D. Skillman and M. P. Haynes, "Oxygen and Nitrogen in Leo A and GR 8", ApJ, **637**, 269–282 (2006).

Völk, H. J., "The correlation between radio and far-infrared emission for disk galaxies - A calorimeter theory", A&A, **218**, 67–70 (1989).

Wu, Y., V. Charmandaris, L. Hao, B. R. Brandl, J. Bernard-Salas, H. W. W. Spoon and J. R. Houck, "Mid-Infrared Properties of Low-Metallicity Blue Compact Dwarf Galaxies from the Spitzer Infrared Spectrograph", ApJ, **639**, 157–172 (2006).

Wu, Y., V. Charmandaris, J. R. Houck, J. Bernard-Salas, V. Lebouteiller, B. R. Brandl and D. Farrah, "Blue Compact Dwarf Galaxies with Spitzer: The Infrared/Radio Properties", ApJ, **676**, 970–977 (2008).

York, D. G., J. Adelman, J. E. Anderson, Jr., S. F. Anderson, J. Annis, N. A. Bahcall, J. A. Bakken, R. Barkhouser, S. Bastian, E. Berman, W. N. Boroski, S. Bracker, C. Briegel, J. W. Briggs, J. Brinkmann, R. Brunner, S. Burles, L. Carey, M. A. Carr, F. J. Castander, B. Chen, P. L. Colestock, A. J. Connolly, J. H. Crocker, I. Csabai, P. C. Czarapata, J. E. Davis, M. Doi, T. Dombeck, D. Eisenstein, N. Ellman, B. R. Elms, M. L. Evans, X. Fan, G. R. Federwitz, L. Fiscelli, S. Friedman, J. A. Frieman, M. Fukugita, B. Gillespie, J. E. Gunn, V. K. Gurbani, E. de Haas, M. Haldeman, F. H. Harris, J. Hayes, T. M. Heckman, G. S. Hennessy, R. B. Hindsley, S. Holm, D. J. Holmgren, C.-h. Huang, C. Hull, D. Husby, S.-I. Ichikawa, T. Ichikawa, Ž. Ivezić, S. Kent, R. S. J. Kim, E. Kinney, M. Klaene, A. N. Kleinman, S. Kleinman, G. R. Knapp, J. Korienek, R. G. Kron, P. Z. Kunszt, D. Q. Lamb, B. Lee, R. F. Leger, S. Limmongkol, C. Lindenmeyer, D. C. Long, C. Loomis, J. Loveday, R. Lucinio, R. H. Lupton, B. MacKinnon, E. J. Mannery, P. M. Mantsch, B. Margon, P. McGehee, T. A. McKay, A. Meiksin, A. Merelli, D. G. Monet, J. A. Munn, V. K. Narayanan, T. Nash, E. Neilsen, R. Neswold, H. J. Newberg, R. C. Nichol, T. Nicinski, M. Nonino, N. Okada, S. Okamura, J. P. Ostriker, R. Owen, A. G. Pauls, J. Peoples, R. L. Peterson, D. Petravick, J. R. Pier, A. Pope, R. Pordes, A. Prosapio, R. Rechenmacher, T. R. Quinn, G. T.

Richards, M. W. Richmond, C. H. Rivetta, C. M. Rockosi, K. Ruthmansdorfer, D. Sandford, D. J. Schlegel, D. P. Schneider, M. Sekiguchi, G. Sergey, K. Shimasaku, W. A. Siegmund, S. Smee, J. A. Smith, S. Snedden, R. Stone, C. Stoughton, M. A. Strauss, C. Stubbs, M. SubbaRao, A. S. Szalay, I. Szapudi, G. P. Szokoly, A. R. Thakar, C. Tremonti, D. L. Tucker, A. Uomoto, D. Vanden Berk, M. S. Vogeley, P. Waddell, S.-i. Wang, M. Watanabe, D. H. Weinberg, B. Yanny, N. Yasuda and SDSS Collaboration, "The Sloan Digital Sky Survey: Technical Summary", AJ, **120**, 1579–1587 (2000).

Yun, M. S., N. A. Reddy and J. J. Condon, "Radio Properties of Infrared-selected Galaxies in the IRAS 2 Jy Sample", ApJ, **554**, 803–822 (2001).

Zackrisson, E., C. Binggeli, K. Finlator, N. Y. Gnedin, J.-P. Paardekooper, I. Shimizu, A. K. Inoue, H. Jensen, G. Micheva, S. Khochfar and C. Dalla Vecchia, "The Spectral Evolution of the First Galaxies. III. Simulated James Webb Space Telescope Spectra of Reionization-epoch Galaxies with Lyman-continuum Leakage", ApJ, **836**, 78 (2017).

Zaritsky, D., R. C. Kennicutt, Jr. and J. P. Huchra, "H II regions and the abundance properties of spiral galaxies", ApJ, **420**, 87–109 (1994).

APPENDIX A

DIRECT, EMPIRICAL, AND SEMI-EMPIRICAL DETERMINATIONS OF OXYGEN ABUNDANCE

In this appendix I describe the different methods of determining oxygen abundance referred to in Section 2.2.2. While all of these methods rely on measurements of optical nebular emission lines, the full suite of emission line diagnostics are not always be available due to source faintness, smaller aperture telescopes, or limited spectroscopic coverage. Spectroscopy from the Sloan Digitized Sky Survey (SDSS) does not reach far enough into the UV to measure the [OII]λ3726Å/λ3729Å doublet for low-redshift, local sources. Low S/N spectra do not always provide adequate measurements of the faint [OIII]λ4363Å lineor the the [SII]λ6731Å/λ6716Å doublet. A fully physical, "direct" determination of the oxygen abundance requires knowledge of both the electron temperature T_e and density N_e, which cannot be calculated without these lines.

In the absence of these diagnostically-critical lines, several "empirical" and "semi-empirical" methods have been developed over the past few decades, which produce oxygen abundance estimates based on only the brightest optical emission lines. I describe the dependencies, underlying physics, and uncertainties associated with all three techniques, and discuss their limitations in low metallicity environments. While the "direct" method is generally always preferable, the metallicities of the galaxy sample presented in Chapter 2 are determined by a mixture of all three of these methods, and consequently carry additional uncertainty, as discussed in Section 2.2.2.

A.1 Direct Abundance Measurement

In this section I summarize the basic emission line diagnostics used to directly determine the nebular oxygen abundance (O/H), the electron temperature T_e, the electron density N_e, and the geometric assumptions of the two-zone photoionization model. The underlying physics of radiative transfer, photoionization, and collisional excitation/deexcitation are described in further detail in (Spitzer, 1977; Osterbrock, 1989; Peterson, 1997).

For a permitted transition in an optically thin gaseous medium, the observed intensity I_l of the emission line is the integral of the energy emitted per unit solid angle per unit time per unit volume j_l along the line of sight ds. For a recombination line such as Hβ, j_l is the product of the electron density N_e, the ionized species n_i, and the effective recombination coefficient $\alpha^{eff}_{nn'}(T)$ between energy levels n and n':

$$\begin{aligned} I_l = \int j_l \; ds &= \frac{1}{4\pi} \int N_i \; N_e \; h\nu_{nn'} \; \alpha^{eff}_{nn'}(T) \; ds \\ &= \int N_i \; N_e \; \epsilon_l(T) \; ds \end{aligned} \tag{A.1}$$

The temperature dependence of the emission coefficient $\epsilon_l(T)$ is typically fit with a

power law, i.e. $\epsilon_l(T) \propto T^{-m}$. If we known the relevant recombination coefficients and can measure the electron density N_e, we can "directly" determine the density of the ionized species (in the case of hydrogen, the density of protons: $N_i = N_p$). For most recombination lines in the observable in optical spectra, the recombination emission coefficients are only weakly dependent on the temperature, i.e. $m \sim 1$. Temperature dependence is often ignored when T_e cannot be determined precisely.

Temperature dependence cannot be ignored for the strong forbidden transitions such as the bright [OII], [NII] and [OIII] optical lines. These are collisionally-excited transitions, so the total energy emitted along the line of sight is determined by the rate at which collisions excite electrons from the ground state n to the higher energy level n' which is capable of producing the forbidden line transition. The fraction b is the balance of electrons in level n' which will eventually deexcite to the level that produce the observed transition. The emission coefficient for collisionally-excited transitions goes as $\epsilon_l(T) \propto T^{-1/2}\ e^{-\chi/kT}$, where χ is the energy difference between level n and level n'.

In full physical detail, the integral of the emitted energy along the line of sight becomes:

$$\begin{aligned} I_l &= \int j_l\ ds = \int N_i\ N_e\ \epsilon_l(T)\ ds \\ &= \frac{1}{4\pi} \int N_i\ N_e\ h\nu\ q_{n,n'}(T)\ b\ ds \\ &= \frac{1}{4\pi} \int N_i\ N_e\ h\nu\ \frac{8.629 \times 10^{-6}}{T^{1/2}}\ \frac{\Upsilon(n,n')}{g_n}\ e^{-\chi/kT}\ b\ ds \end{aligned} \tag{A.2}$$

where $q_{n,n'}(T)$ is the total collisional excitation rate per unit time per unit volume per ion per colliding electron, $\Upsilon(n,n')$ is the collisional strength, g_n is the degeneracy of level n, and b is the fraction of excitations to level n' that result in emission in the relevant line. While most of these values can be looked up, it is necessary to observationally determine T_e and N_e before the abundance can be calculated.

A.1.1 Electron temperature diagnostics

Electron temperature T_e can by obtained by comparing the strengths of collisionally-excited lines from the same ionized species which originate from energy levels with very different excitation energies. O^{+2} and N^+ are two such species: the bright [OIII]λ5009Å + λ4959Å and [NII]λ6583Å + λ6548Å doublets are the product of collisional excitations into the $^1D_2$ level, while the [OIII]λ4363Å and [NII]λ5755Å lines come from the $^1S_0$ level (Figure 28a). In the low-density limit ($N_e < 10^5$ cm^{-3}),

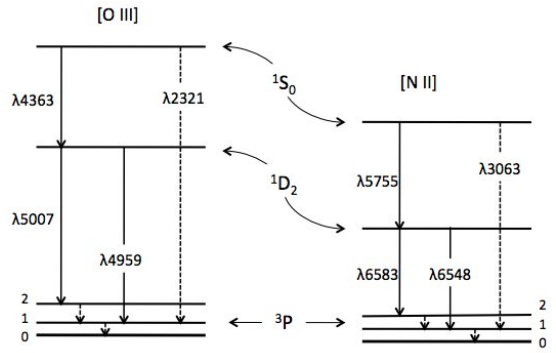

(a) Energy levels of the ground $2p^2$ configuration of O^{+2} and N^+, with diagnostic forbidden transitions marked.

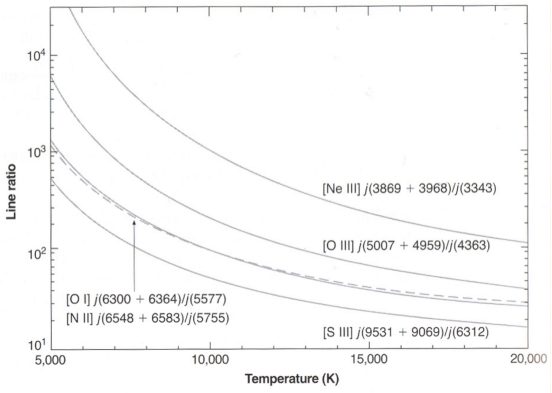

(b) Calculated dependence of the [OIII] and [NII] line ratios on electron temperature T_e, for $N_e \leq 1$ cm$^-3$. From Osterbrock (1989); Osterbrock and Ferland (2006), used with permission from G. Ferland.

Figure 28

where collisional deexcitation can be neglected, the relative strengths of these emission lines will be determined solely by the electron temperature T_e, the collision strengths $\Upsilon(n, n')$, the transition probabilities for radiative de-excitation $A(n', n' - 1)$, and the energy difference in between the excited levels ΔE:

$$\frac{j_{\lambda 4959} + j_{\lambda 5007}}{j_{\lambda 4363}} = \frac{\Upsilon(^3P,^1D)}{\Upsilon(^3P,^1S)} \left[\frac{A(^1S,^1D) \ + \ A(^1S,^3P)}{A(^1S,^1D)} \right] \frac{\bar{\nu}(^3P,^1D)}{\bar{\nu}(^1D,^1S)} \ e^{(\Delta E/kT)} \quad \text{(A.3)}$$

where

$$\bar{\nu}(^3P,^1D) = \frac{A(^1D_2,^3P_2)\nu(\lambda 5007) \ + \ A(^1D_2,^3P_1)\nu(\lambda 4595)}{A(^1D_2,^3P_2) + A(^1D_2,^3P_1)} \quad \text{(A.4)}$$

The contribution of the $\lambda 4959$ de-excited electrons to the $^1D_2$ level can also be ignored. Plugging in the relevant collision strengths and transition probabilities for the [OIII] lines, and including a factor of $N_e/T^{1/2}$ for higher density conditions (Osterbrock and Ferland, 2006), equation A.5 becomes:

$$\frac{j_{\lambda 4959} + j_{\lambda 5007}}{j_{\lambda 4363}} = \frac{7.9 \ e^{(3.29 \times 10^4/T)}}{1 \ + \ (4.5 \times 10^{-4} N_e/T^{1/2})} \quad \text{(A.5)}$$

Calculated line ratios as a function of electron temperature are show for species with useable optical lines in Figure 28b. The ratios are typically quite large: even in the

relevant temperature range of $T > 10,000$K for low-metallicity environments, the [OIII]λ5007 $+ \lambda$4959 emission may be tens or even hundreds of times brighter than the fainter [OIII]λ4363 transition. For low S/N spectra, this large emission ratio means that it is may not be possible to measure [OIII]λ4363 or directly determine the temperature.

A.1.2 Electron density diagnostics

Electron density N_e is typically determined from the ratio of two lines of the same ion with nearly identical excitation energies but differing Einstein A emission coefficients. The [OII]λ3726 + λ3729 and [SII]λ6716 + λ6731 doublets are good examples: The $^2D^0_{5/2}$ and $^2D^0_{3/2}$ levels have identical collision strengths q, nearly-identical excitation energies ΔE, but different Einstein A emission coefficients (see Figure 29a). This combination makes the emission ratios of these doublets sensitive diagnostics of electron density.

Following Tielens (2005), we can define the critical density for a given collisional transition, $N_{cr} = A(n', n'-1)/q(n, n')$, where once again $A(n', n'-1)$ is the Einstein emission coefficient of the $n' \rightarrow n'-1$ transition, and $q(n, n')$ is the collisional strength coefficient for excitation to level n' from the ground state n. Recall that "forbidden" transitions are so-called because their oscillator strengths and Einstein coefficients are small, and consequently the timescales for emission of photons are long compared with permitted transitions; in a high density environment, an ion collisionally excited into the "forbidden" energy state may not have time emit a photon before another collision deexcites the atom.

The ratio of ions in the ground state to ions in the excited state is given by:

$$\frac{N(^2D_{5/2})}{N(^4S)} = \frac{g(^2D_{5/2})}{g(^4S)} \frac{e^{-\Delta E/kt}}{1 \ + \ (N_{cr(5/2)}/N_e)} \tag{A.6}$$

$$\frac{N(^2D_{3/2})}{N(^4S)} = \frac{g(^2D_{3/2})}{g(^4S)} \frac{e^{-\Delta E/kt}}{1 \ + \ (N_{cr(3/2)}/N_e)} \tag{A.7}$$

where $N_{cr(5/2)} = A(^2D_{5/2})/q(2D_{5/2})$ and $N_{cr(3/2)} = A(^2D_{3/2})/q(^2D_{3/2})$. Dividing Equation A.6 by Equation A.7, we can find the ratio of the ions between the levels of the ^2D doublet:

$$\frac{N(^2D_{5/2})}{N(^2D_{3/2})} = \frac{g(^2D_{5/2})}{g(^2D_{3/2})} \frac{N_e \ + \ N_{cr(3/2)}}{N_e \ + \ N_{cr(5/2)}} \tag{A.8}$$

In the low density limit $N_e < N_{cr}$, collisions are rare, and any ion excited by a collision is unlikely to be deexcited by a second one; all of the electrons in the excited level

can be assumed to eventually return to their ground states by emitting a photon of the "forbidden" transition, regardless of however tiny the corresponding Einstein A coefficient may be. Consequently, for levels with identical collisional strengths $q(^4S_{3/2},^2 D_{3/2}) = q(^4S_{3/2},^2 D_{5/2})$, as the electron density approaches zero $N_e \to 0$, the emission line ratio is simply the ratio of the energy level degeneracies.

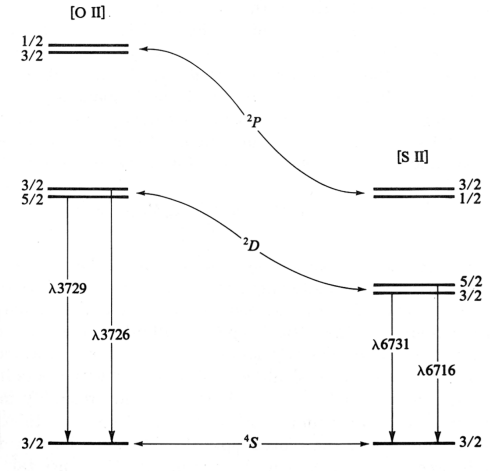

(a) Energy levels of the $2p^3$ ground configuration of O^+ and the $3p^3$ ground configuration of S^+, with diagnostic forbidden transitions marked.

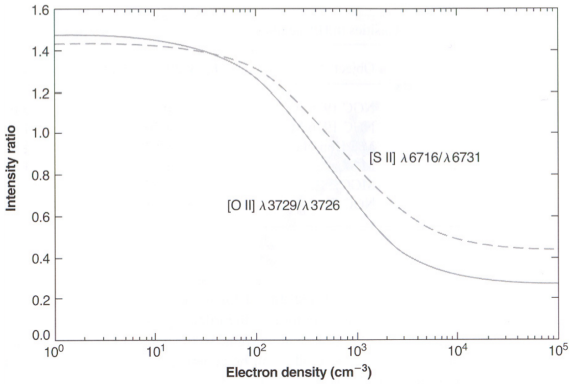

(b) Calculated dependence of the [OII] λ3729Å/λ3726Å and the [SII] λ6716Å/λ6731Å line ratios on electron density N_e, for $T_e = 10,000$K. From Osterbrock (1989); Osterbrock and Ferland (2006), used with permission from G. Ferland.

Figure 29

We can confirm this logic solving Equation A.8 in the limit of $N_e \to 0$. Recall that the collisional strengths of the doublet are the same, $q(^2D_{5/2}) = q(^2D'_{3/2})$, and that the emitted energy is $j_l = N_l\ A_l$. So for the [OII] doublet, the emission line ratio becomes:

$$\frac{j_{\lambda 3729}}{j_{\lambda 3726}} = \frac{N_{\lambda 3729}}{N_{\lambda 3726}} = \frac{g_{\lambda 3729}}{g_{\lambda 3726}} = \frac{3}{2} \tag{A.9}$$

In the high density limit, $N_e > N_{cr}$, the energy level distribution approaches local thermodynamic equilipbrium, with the energy level distribution determined by the Boltzmann equation. Again, because the doublet transitions have levels that are nearly identical, their LTE populations are identical except for their statistical degeneracies g_i. But not every excited electron will emit a photon: the ion may be collisionally deexcited before it radiates, and so the ratio of the Einstein A coefficients figures into the ratio of the emitted lines:

$$\frac{j_{\lambda 3729}}{j_{\lambda 3726}} = \frac{N_{\lambda 3729}}{N_{\lambda 3726}} \frac{A(^4S_{3/2},^2 D_{5/2})}{A(^4S_{3/2},^2 D_{3/2})} = \frac{g_{\lambda 3729}}{g_{\lambda 3726}} \frac{A(^4S_{3/2},^2 D_{5/2})}{A(^4S_{3/2},^2 D_{3/2})} = \frac{3}{2} \frac{3.6 \times 10^{-5}}{1.6 \times 10^{-4}} = 0.34 \tag{A.10}$$

We can see from Figure 29b that the calculated emission line ratio does indeed go to $j_{\lambda 3729}/j_{\lambda 3726} = 1.5$ at low electron densities, and $j_{\lambda 3729}/j_{\lambda 3726} \sim 0.3$ in the high density limit. These diagnostics are most powerful around the critical density N_{cr}.

A.1.3 Two-zone ionization model

Once the the electron density and temperature are known, we could simply plug our numbers use Equations A.1 and A.2 to directly calculate the O/H ratio. However, observations and photoionization theory agree that the [OII] and [OIII] originate in spatially distinct zones, whereas HII will be found throughout the ionized nebula. In order to correctly estimate the (O/H) ratio, we much calculate the abundances of all ionized species of oxygen present with the ionized HII. The most simple mathematical description of this situation is the two-zone ionization model.

The first four ionized states of oxygen have ionization energy thresholds $\Delta E = [13.62, 35.12, 54.94, 77.41]$ eV. (Compare to hydrogen, with $\Delta E = 13.60$ eV). In an HII region or planetary nebula, the ionizing photons are typically only hot enough to knock one or two electrons off of the oxygen atom. The vast majority of the oxygen will be in O^+ and O^{+^2}, with the doubly-ionized O^{+^2} more closely concentrated around the ionizing source. A small amount of oxygen is found to be in more ionized species, but measurements of O^{+^3} and O^{+^4} ultraviolet lines suggest this is typically only a few percent of the total oxygen in the nebula, and these species are usually ignored in optical studies. Disregarding these higher ionization states, the total oxygen abundance becomes:

$$\frac{O}{H} = \frac{O^+ + O^{+^2}}{H} \tag{A.11}$$

We will need to derive electron temperatures for both zones. The distribution of ionized species are typically confirmed via ionization grids, Garnett (1992) confirms that:

$$T_e(O^{+^2}) = T_e(Ne^{+^2}) = T_e(Ar^{+^3}) \tag{A.12}$$

and

$$T_e(O^+) = T_e(N^+) = T_e(S^+) \tag{A.13}$$

We can therefore obtain $T_e(O^{+^2})$ from the [OIII](λ4959+λ5007)/λ4363 ratio, while obtaining $T_e(O^+)$ from the [NII](λ6548+λ6563)/λ5755 ratio. The electron density N_e for the lower ionization zone can be determined from either the [SII]; this value is typically applied to the higher ionization zone as well.

The final abundance calculation from the direct method is typically complicated enough to require an iterative process of comparing computationally-calculated photoionization grids, and adjusting the geometry to match the full suite of measured line ratios.

A.2 Empirical Abundance Measurements

Sometimes the fainter lines necessary for the direct abundance estimate are not accessible. In particular, the large intensity ratios in Figure 28b mean that for fainter objects it may be possible to measure [OIII]λ5007+λ4959, white [OIII]λ4363 line may be lost in the noise. Similarly, while the [NII] lines are quite bright, the [SII] lines can be difficult to observe.

This situation has caused authors to develop several strong-line "empirical" diagnostics that do not require the full suite of optical emission lines to estimate astrophysical conditions. Originally pioneered by Alloin *et al.* (1979) and Pagel *et al.* (1979), these techniques use only the brightest lines in the emission line to derive abundances, ionizing flux, and

For abundance measures, R_{23} is the most popular method, because it uses the very brightest lines in an HII or PNe spectrum, which are easily observed via low-resolution spectroscopy on small aperture telescopes (1-2 meters).

Using SDSS spectra for 53,000 galaxies, Tremonti *et al.* (2004, (T04)) demonstrate the uncertainties associated with the R_{23} method for oxygen abundances between $9.5 < 12 + [O/H] < 8.0$ (see Figure 30). T04 determine the "true" metallicity using a more sophisticated simultaenous

$$12 + [O/H] = 9.185 - 0.313x - 0.264x^2 - 0.321x^3 \tag{A.14}$$

where $x \equiv \log(R_{23})$.

Unfortunately, the T04 galaxy sample is not well sampled at low metallicity. While the low-metallicity double-valued feature of the Edmunds and Pagel (1984) and McGaugh (1991) R_{23} formulations are apparent, neither fits the T04 distribution well below $12 + [O/H] < 8.3$, and galaxies with $12 + [O/H] < 8.0$ are almost entirely absent.

While the SDSS sample demonstrates the intrinsic spread of the R_{23} measure, it does not do a good job of constraining the value of this diagnostic at low metallicity.

Calculated theoretical models give a better sense of the efficacy of strong line measures at low metallicity. Kewley and Dopita (2002) examined a variety of common strong-line diagnostics, for a range of metallicities and ionization q-parameters. The q-parameter is the number of ionizing photons per cm^2 per second, and is defined as:

$$q_{eff} = fracQ_{H^0} 4\pi R_s^2 n \tag{A.15}$$

where Q_{H^0} is the flux of photons emitted above the Lyman limit, R_s is the Strömgren radius, and n is the local number density of hydrogen atoms. From their Figure 5 we see that R_{23} is not a particularly sensitive diagnostic at low metallicity– even more so if we don't know the ionization parameter q for the local environment. We can get a sense of q from the [OII]/[OIII] ratio, but only if we already know the metallicity. Other diagnostics break the degeneracy, but there are built-in assumptions about the (N/O) and (S/O) ratio remaining essentially consistent with Solar. In general, R_{23} is not optimal for low metallicity samples.

A.3 Semi-Empirical Abundance Measurements

Strong line empirical abundance measures are not well-suited to low-metallicity environments, but the direct method relies on the measurement of the [OIII] $lambda4363$ line, which is not always possible for faint galaxies. In response to this situation, Izotov et al. have developed their own "semi-empirical" method, for galaxies in which uses the traditional bright lines are readily observed, but the temperature-dependent [OIII] $lambda4363$ line is not necessarily available. Using the photoionization models of Stasińska and Izotov (2003), they develop an empirical temperature relation based on the available bright lines

$$t_e(OIII_= - 1.36854 log fracI(\lambda 3727) + I(\lambda 4959) + I(\lambda 5007) I(H\beta) + 2.62577 \tag{A.16}$$

where $t_e(OIII) = 10^{-4} T_e(OIII)$. It should be noted that this calibrator requires the use of the [OII]λ3727 line, which is unavailable in SDSS spectra.

For the galaxies with direct measurements of [OIII]$lambda4363$, there does appear to be variations between the T_e estimated from the bright line vs. the direct method, and consequently in the metallicities estimated via the two technique. The semiempirical method does fare better than the various bright line methods, which exhibit large systematic offsets from the "direct" metallicities (see Izotov and Thuan (2007) Table 5). Based on these variations, even with "semiempirical" or "direct" measurements, nebular oxygen abundances should always be assumed to be uncertain by 0.2 dex, regardless of the advertised uncertainties.

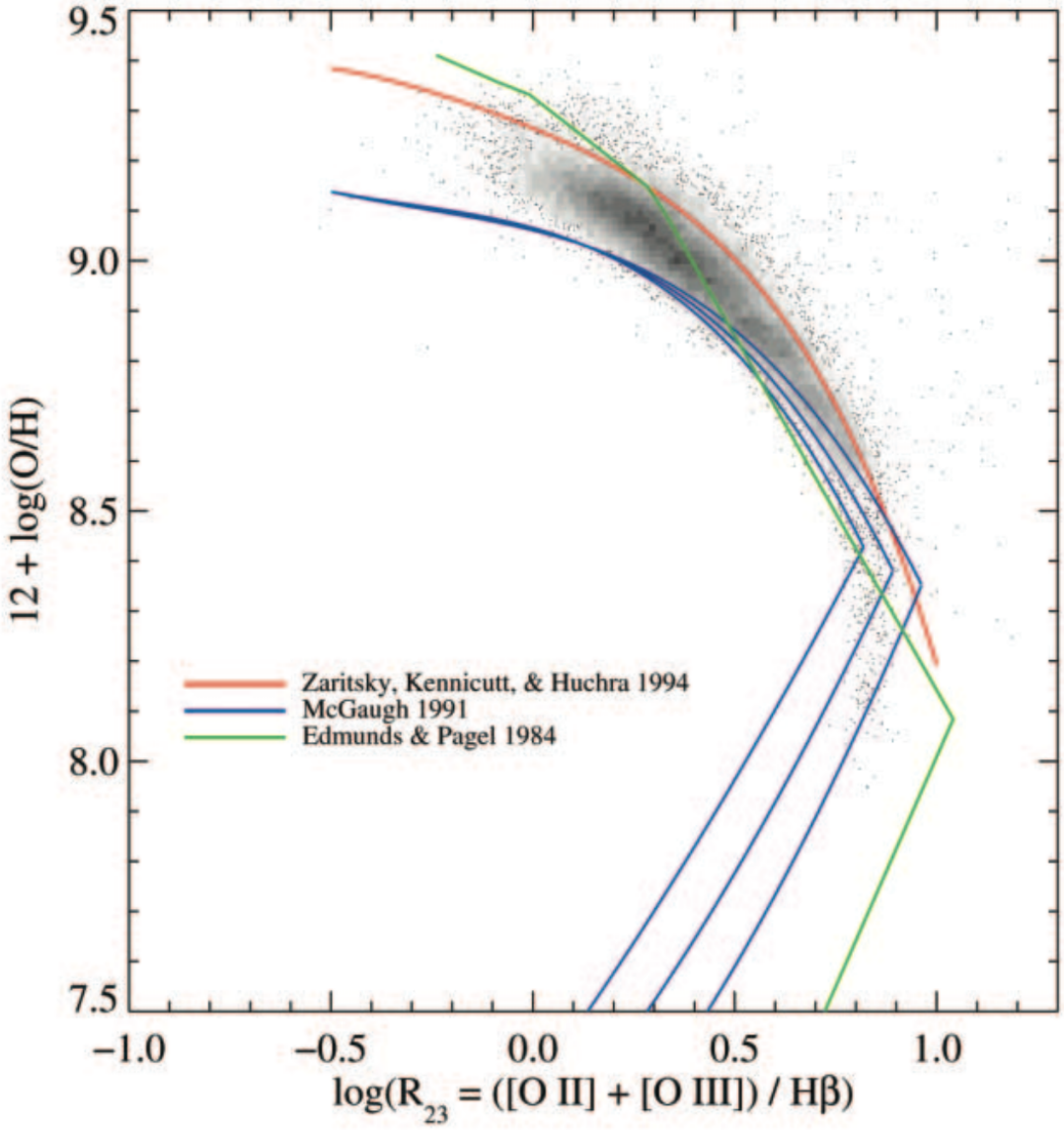

Figure 30: Using SDSS spectra of 53,000 galaxies... Tremonti *et al.* (2004). The empirical calibrations of Edmunds and Pagel (1984); McGaugh (1991) and Zaritsky *et al.* (1994) are plotted for comparison. The T04 sample shows both the intrinsic spread in R_{23} as a function of "true" metallicity, and the systematic offsets of the commonly-cited R_{23} calibrations at Solar and super-Solar metallicities. Unfortunately, the SDSS sample does not extend to metallicities below $\sim 1/5$th Solar, where the R_{23} diagnostic become degenerate.